UNIVERSITÄT DES
SAARLANDES

UNIVERSIDAD NACIONAL DE
MAR DEL PLATA

Final project submitted in fulfilment of the requirements for the degree of
Materials Engineering

Enhancement of the electrical and tribological properties of electrical connectors using Direct Laser Interference Patterning

Author:	Poliseno, Jazmín Carla
Director:	Dr. Valdez, Matías
Co-Director:	Dr. Reinert, Leander

Dedicado a mi mamá y a mi hermano.

Y a un ser muy especial llamado Hera.

Preface

The present work is a Final Project submitted to complete the requirements of the Materials Engineering degree, to be granted by the Faculty of Engineering of the National University of Mar de Plata (UNMdP, Argentina). This work was carried out in the frame of a project under a cooperation agreement between the Functional Materials Chair of the Materials Science & Engineering Department at Saarland University (UdS, Germany) and TE Connectivity (Bensheim, Germany).

I declare that I have authored this work independently, that I have not used other than the declared sources/resources, and that I have explicitly marked all material that has been quoted either literally or by content from the used sources.

This work contains a lock flag and is to be treated confidentially.

Poliseno, Jazmín Carla
Mar del Plata, July 2019

Resumen

Dada la pronunciada electrificación de la industria automotriz, el número de conectores eléctricos presentes en los vehículos, así como las demandas en los mismos han ido aumentando en el tiempo. A raíz de la necesidad de disminuir el peso total del automóvil, se han desarrollado sistemas multipolos, los cuales deben cumplir dos exigencias principales: una resistencia eléctrica baja y una fuerza de conexión y desconexión reducida. Además, los conectores deben contar con una resistencia contra el *fretting* elevada. El *fretting* es considerado el mecanismo de degradación principal de los conectores eléctricos con recubrimiento de estaño. Este término hace referencia a la presencia de micro-movimientos entre las superficies del conector debido a alteraciones mecánicas o tensiones generadas por desajustes de expansión térmica. Estos movimientos se encuentran acompañados por una continua corrosión de la superficie y por lo tanto un continuo aumento de la resistencia eléctrica.

En general, estos requerimientos pueden alcanzarse modificando el material del recubrimiento utilizado o el tratamiento superficial del mismo. En su trabajo, Leidner y colaboradores han demostrado que a través de la estructuración por interferencia láser directa de la superficie del pin del conector la resistencia de contacto puede reducirse hasta en un 50%. Una topografía con forma sinusoidal presenta menor resistencia de contacto que la típica superficie plana ya que en los máximos de la topografía surge un aumento en la presión de contacto y por lo tanto una mayor superficie de contacto. Sin embargo, este tipo de superficie muestra un mayor coeficiente de fricción lo cual resulta en una mayor fuerza de conexión y en una menor resistencia al *fretting*.

Durante la estructuración por interferencia láser directa, se generan gradientes de temperatura de más de 1000°C entre los máximos y mínimos de interferencia. Debido a las tensiones superficiales que surgen bajo el efecto Marangoni, el material fundido migra de los máximos de interferencia hacia los mínimos, donde los frentes de material se unen y solidifican formando los máximos de la estructura. Dependiendo de la fluencia del láser utilizado y el período de la estructura, se puede obtener porosidad en los máximos de la misma. En el presente trabajo se plantea como objetivo disminuir la fuerza de conexión de conectores eléctricos al encerrar PAO 40 en la porosidad generada mediante la estructuración por interferencia láser de la superficie del pin.

Como muestras se utilizaron conectores eléctricos de la familia MCON 1.2 comercializada por TE Connectivity. Tanto el pin (macho) como la terminal (hembra) están compuestos por una base de cobre recubierta de estaño mediante inmersión en caliente. La estructuración de las muestras se llevó a cabo mediante un láser pulsado de nanosegundos Nd: YAG con una duración de pulso de 10 ns, una frecuencia de 10 Hz y una longitud de onda

de 532 nm. Previamente se ha demostrado que el periodo óptimo que debe poseer la estructura para obtener porosidad en los máximos de la misma es aproximadamente de 15 µm. Asimismo, en la primera parte de este trabajo se seleccionó la fluencia del láser óptima para lograr este objetivo. Las muestras fueron caracterizadas mediante interferometría de luz blanca, y microscopía electrónica (SEM/FIB). Una vez confirmada la existencia de poros en la estructura, se estructuraron muestras aplicando a la superficie PAO 40 y se evaluó la presencia del lubricante dentro de los poros mediante espectroscopía Raman. A continuación, se midió la fuerza de conexión y desconexión de los conectores eléctricos durante 10 ciclos, utilizando la misma terminal tanto para los pines estructurados como sin estructurar. Los resultados de estos ensayos fueron respaldados con mediciones del coeficiente de fricción. Además, se estudiaron las propiedades eléctricas de los conectores para corroborar que no hubiera una pérdida en la performance eléctrica de los mismos por el lubricante encerrado en los poros de la estructura. En primer lugar, se registró la variación de la resistencia de contacto en función del camino de rozamiento y en función de la fuerza normal aplicada a la superficie. Luego, se evaluó la resistencia al *fretting* de los contactos y se calculó la curva de *derating* de los mismos. Por *derating* se entiende la operación de un componente eléctrico por debajo de su capacidad máxima con el fin de extender su vida útil. La curva define la corriente máxima que se puede aplicar a una cierta temperatura. Por último, se caracterizó el envejecimiento de los conectores.

A continuación, se destacan los principales resultados del presente trabajo:

- Una potencia de láser entre 5,0 y 5,5 W permite obtener porosidad en los máximos de la estructura. Se forman compuestos intermetálicos, los cuales ocupan alrededor del 60% del recubrimiento de estaño. No se observó diferencia en las capas de compuestos intermetálicos entre los pines estructurados y aquellos sin estructurar utilizados como referencia.
- Tanto máximos como mínimos de la estructura presentaron picos característicos del PAO 40 en la espectroscopía Raman.
- Los pines sin estructurar presentaron una fuerza promedio de 4,5 N. Solo después del quinto ciclo, cuando el lubricante se libera de los máximos de la estructura, la fuerza de conexión adquiere un valor menor a la fuerza obtenida para los pines sin estructurar. Para reducir el número de ciclos en los que sucede esto, se propuso cepillar la superficie de los pines antes del ensayo. Al desgastar la superficie, se obtiene una reducción en la fuerza de conexión de aproximadamente 50% a partir del segundo ciclo.
- Al igual que para la fuerza de conexión, los pines estructurados presentaron un menor coeficiente de fricción que las muestras sin estructurar recién a partir del quinto ciclo. Al cepillar los pines, el coeficiente de fricción disminuye. Puede destacarse que el cepillado

de la superficie reduce la rugosidad de la superficie, además de promover la liberación del lubricante en un menor número de ciclos.

- La resistencia de contacto obtenida para los pines estructurados es menor a los pines sin estructurar tanto en función del camino de rozamiento como en función de la fuerza normal aplicada. El cepillado de la superficie perjudica la resistencia de contacto, aumentándose a valores similares a los que presentan las muestras sin estructurar.
- La resistencia total de los conectores eléctricos con pines estructurados resulta similar a los conectores utilizados como referencia. Esto se debe principalmente a la interacción entre los múltiples puntos de contactos presentes en el sistema MCON 1.2 y a la presencia de lubricante en los máximos de la estructura.
- Los pines estructurados poseen una mayor resistencia frente a la corrosión por *fretting.* Estos resistieron aproximadamente el doble de ciclos de micro-movimientos que los pines sin estructurar principalmente debido a la presencia de lubricante y una disminución del coeficiente de fricción.
- No se observó diferencia entre las curvas de *derating* de los pines estructurados y sin estructurar. Ambas muestras admiten un máximo de corriente de 20.5 A y una temperatura máxima de 130°C.
- Se ensayó el envejecimiento de los conectores eléctricos en un horno a 100°C durante 1200 hs. Luego de este calentamiento, la resistencia total aumentó para ambos tipos de conectores, mientras la fuerza de conexión disminuyó en ambos casos. Los pines estructurados presentaron una mayor reducción en la fuerza. La causa principal de estos cambios es la relajación de las lengüetas de fijación de la terminal hembra del conector.

Para lograr una reducción significativa de la fuerza desde la primera conexión, sin comprometer la performance eléctrica y tribológica, se propone utilizar en un trabajo futuro un láser monolítico con un haz de mayor diámetro. Esto permitiría obtener una estructura más homogénea a lo largo de toda la superficie del pin. Por lo tanto, se lograría ajustar aún más el valor de potencia elegida y así optimizar la posición y el tamaño de los poros en los máximos de la estructura.

Contents

Acknowledgments

I would like to sincerely acknowledge the help, advice and encouragement of many people and institutions during the work on this final project:

- Prof. Dr. Matias Valdez (UNMdP) for his supervision and patient during the correction phase of this work,

- Prof. Dr. Leander Reinert (UdS) and Dr. Michael Leidner (TE Connectivity) for giving me the opportunity to research and work in a very interesting field,

- Dr. Helge Schmidt and Eng. Stefan Thoss for their support during my internship at TE Connectivity,

- Dr. Sebastian Suarez and Eng. Katherine Aristizabal for FIB and SEM observations, and specially for the interesting suggestions,

- Dr. Silvia Simison and Dr. María Andrea Camerucci, for their contribution in the I.DEAR Program and for letting me be part of it,

- Rosette Tsapi Sonking and Jai Koshta for their kindness and friendship during my time in TE Connectivity,

- All the technical staff of TE Connectivity for the comfortable and friendly work environment,

- To the National University of Mar del Plata and all the professors who helped me to acquire important tools for my future professional career.

- Last but not least, to my mother Claudia and my brother Federico for their unconditional love and help in all the stages of my life. I dedicate this work to Hera, my study partner during all this time. This important achievement is also theirs. Additionally, I would like to express my gratitude to all my friends for their continuous motivation, specially to Johnnatan Posadas for his support during the last months in Germany.

List of Abbreviations

CAGR	Compound Annual Growth Rate
COF	Coefficient of Friction
CVD	Chemical Vapor Deposition
DLIP	Direct Laser Interference Patterning
EDX	Energy Dispersive X-ray Spectroscopy
IMC	Intermetallic Compound (also IMP)
LASER	Light Amplification by Stimulated Emission of Radiation
FIB	Focused Ion Beam
LA	Laser Annealing
LC	Laser Cleaning
LCVD	Laser-induced Chemical Vapor Deposition
LEC	Laser-induced Electrochemical Plating/Etching
LIS	Laser-induced Isotope Separation/IR-laser Photochemistry
LL	Locking Lance
LSCW	Laser-supported Combustion Waves
LSDW	Laser-supported Detonation Waves
MPA	Multiphoton Absorption
MPI	Multiphoton Ionization
PAO	Poly Alpha Olefines
PCB	Printed Circuit Board
PLA	Pulsed-laser Ablation
PLD	Pulsed-laser Deposition
SEM	Scanning Electron Microscopy
WLI	White-Light Interferometer

List of Symbols

α	Absorption coefficient
a	Radius of a-spot
A	Laser beam area
A_b	Load-bearing area
c	Speed of light
δ	Absorption depth
ϵ_0	Vacuum permittivity
E	Modulus of Young
E_j	Components of the light wave field
f	Frequency
F	Laser fluence
F_N	Normal force
h	Planck constant
H	Hardness
I	Light intensity
J	Current density
κ	Thermal diffusivity
λ	Wavelength
l_T	Thermal diffusion length
M	Lens magnification
p	Laser power
P	Period of interference pattern
R_C	Contact resistance
R_E	Constriction resistance
R_F	Film resistance
R_M	Conductor/Material resistance
ρ	Resistivity
σ_y	Yield Stress
τ	Frequency of the ns-pulsed laser irradiation
θ	Angle between beams
ξ	Pressure factor

1. Introduction

Nowadays the social interest in the quality of vehicle has been changed from running performance to luxury, comfort, safety and more environmental sustainability. This leads to a boom in the electrification of the automotive industry. The automotive connectors market was estimated to be USD 4.38 Billion in 2016 and is projected to grow to USD 6.28 Billion by 2021, at a compound annual growth rate (CAGR) of 7.46% [1]. The numbers, types, and complexity of electrical network systems in a commercial vehicle are continuously increasing as the number of electrical contact points increases as well. In a modern luxury-class vehicle, there are up to 400 connectors with more than 3000 individual contacts [2]. The automotive connectors market has major applications in the powertrain system; which is followed by safety and infotainment systems.

Not only is the sheer number increasing, but also the demands on electrical connectors. These devices are used in motor vehicles for energy transmission and networking of electrical and electronic systems, and often represent a weak point of the systems. Different types of electrical contacts and materials are used depending on the application. Tin coated copper contacts are the most common in heavy vehicle electrical connectors. Although tin has an easy availability and is the least expensive non-noble contact material, it is relatively soft and thus, is not very resistant to abrasion. A protective oxide film forms on the tin surface, which limits further corrosion but increases the electrical resistance. However, because of its brittleness, it can be damaged during connection allowing the creation of electrical contacts with high local conductivity. In spite this advantage, tin is susceptible to fretting corrosion and tends to form detrimental intermetallic compounds in contact with copper [3,4].

Electrical connectors are exposed to different conditions during its operation such as strong temperature fluctuations, vibrations, and corrosive environment. The most common degradation mechanisms of the connectors are corrosion, wear, and loss of contact normal force, which may become more severe at high operating temperature. Driven by the design trend towards miniaturization, the operating temperatures for connectors have slowly increased from 125 °C to more than 150 °C. Besides, elevated temperatures are caused by a poor heat dissipation of the individual contacts due to a reduced cross-section. The electrification of the powertrain in electric and hybrid vehicles also results in the use of higher currents and voltages, which also leads to an increase in temperature [5, 6].

For tin plated contacts, the dominant mechanism is the fretting corrosion. This phenomenon, as its name indicates, results of the combination between fretting wear and environmental corrosion. Fretting corrosion occurs at the interface of contacting materials subjected to small oscillatory movement due to mechanical and thermal stresses. This causes an increase in the electrical contact resistance.

Wear as a degradation mechanism is important because increases corrosion susceptibility by removing the protection provided by the passive layer. High temperatures during operation produce metal softening, which represents a higher wear. This environment condition in the engine could also influence the rate of oxidation, the intermetallic formation and trigger other chemical reactions [7-9]

In addition to a low contact resistance for establishing a good electrical connection, a high wear resistance is required based on these failure mechanisms. A decrease in the connection force is also desirable mainly for facilitation of the automobile assembly work and the maintenance of connectors. The principal reason for this lies in the miniaturization that has led to an increment in the number of individual pins. The force increases proportionally to the number of pins involved. Therefore, multi-pole connectors require greater force to be connected, which in turn reduces the workability [11,12]. According to the current North American ergonomic regulation, the insertion force in automotive wire harness terminal connections cannot be more than 75 N [13]. A reduction in the normal contact force may be a solution for improving mating and unmating process, however, it is detrimental to the functionality of connectors. This reduction hinders the suppression of vibrations promoting fretting corrosion and, on the other hand, increases the electrical contact resistance. The contact resistance is inversely dependent on the contact normal force, which in turn is closely related to the insertion force [2,5,14].

Over the years, different techniques were developed in order to reduce the insertion force without compromising the electrical contact resistance. Various efforts have concentrated almost entirely on improving contact surface coatings and materials. Moreover, other design concepts have been proposed in order to minimize the insertion force by modifying the pin or the spring shape [14,15].

Recently, a promising new approach for achieving this goal has been pursued, based on the topographic texturing of the coating or substrate. The purpose of the texturing is to improve the electrical properties of the connectors by promoting the formation of a metallic, well-conducting contact surface. It has been showed that sinusoidal-like surface topography can reduce the electrical contact resistance of a tin-coated contact by a factor of 2 for a given contact normal force [16-18]. However, these surfaces show disadvantages in terms of tribology. Pores can be obtained within the topographic maxima, which can be used to enclose a lubricant in order to reduce the coefficient of friction of this surface [19].

The present work contributes to a project established by *TE Connectivity* in cooperation with the Chair of Functional Materials at the Saarland University. *TE Connectivity*, previously known as *Tyco Electronics*, is a global technology and manufacturing leader in highly engineered connectors and sensors. With customers in nearly 150 countries, the company offers an extensive product portfolio for a variety of industries, such as automotive, industrial equipment, data communication systems, aerospace, medical, etc.

The main goal of this project is to reduce the insertion force of electrical connectors by enclosing poly alpha olefins (PAO) as lubricant in the topographic maxima of the surface of pins modified by means of direct laser interference patterning (DLIP). For this, in first place, the parameters for the laser texturing were optimized in order to obtain porosity within the structure. Then, pins of commercial connectors (MCON family) were textured using DLIP. A complete study of the electrical and tribological properties of textured pins including electrical contact resistance, coefficient of friction, fretting corrosion resistance, long-term behavior and, primarily, insertion force, was carried out.

It should be noted that there is no strict distinction between surface structure and texture, but generally, surface texture is used for smaller scales. In this work, the structure obtained by means of DLIP will be considered as texture because the surface presents a sinusoidal-like shape with a period of a few micrometers after being irradiated with laser beams. The term should not be mistaken for crystallographic texture.

This work is organized into four main sections: principal theoretical concepts, description of experimental techniques and methods, results and discussion, and finally the conclusion. The first section introduces the reader to the main concepts associated with electrical connectors in the automotive industry and the DLIP technique. Previous research papers related to this work are also reviewed in this section. The experimental methodology and the different instruments used in this work are introduced in the second section. The analysis and interpretation of the results are shown in the third section. Lastly, a comprehensive conclusion and recommendations for further research will be presented.

2. Objectives

2.1 General Objective

The main objective of this study was to decrease the connection force of electrical connectors by enclosing PAO 40 as lubricant in the porosity generated during the texturing of the pin surface by means of direct laser interference.

2.2 Specific Objective

1. To optimize the texturing process in order to obtain porosity at the maxima of the topography: fine-tune the experimental setup of optical elements, laser power, etc., by comparing the topography of textured samples with different powers using a White Light Interferometer.
2. To evaluate the presence of porosity in the topographic maxima by observing cross-sections of the surface by FIB / SEM. To use Raman spectroscopy to corroborate the presence of PAO 40 in the porosity. To test possible methods to place the lubricant on the surface to be structured.
3. To texture pins on both sides using PAO 40 as lubricant with the parameters previously determined. (Maximum quantity: 50)
4. To measure the connection force of the textured pins with PAO 40.
5. To analyze the electrical properties of the pins by measuring the resistance as function of an applied normal force and as function of a frictional path. To measure the coefficient of friction as function of a cyclical displacement.
6. To evaluate the fretting corrosion resistance in textured pins.
7. To determine the derating curve of the electrical connectors.
8. To study the long-term aging behavior of the electrical connectors. To compare the electrical resistance and the connection force before and after the aging test.
9. Final discussion of the results.

3. Literature Review

This chapter reviews the most important theoretical concepts in order to get a better understanding of the present work. Previous work on electrical contact resistance and insertion force enhancement will be also commented.

3.1 Electrical Contact Theory

An electrical contact is defined as the junction between two current-carrying members of an electrical device aimed to ensure the continuity of the electric circuit. These current-carrying members called as contact parts or simply contacts, can be divided into anode and cathode. They are connected to the positive and negative clamp respectively, which means that through the anode enters the current that leaves from the cathode contact.

For the electrical contact to be generated, a mechanical force must be applied to press the contact parts together. Real surfaces are not perfectly flat, but rough on the microscale and comprise many asperities. Furthermore, in practice, all the materials can be deformed. Thus, when two parts come in touch with enough force, the micropeaks of the surface will deform and penetrate the natural oxide or other electrically insulating layers, such as contaminants or dust, creating localized conducting paths to transfer the electrical current commonly referred as *a-spots*. The quality of the electrical contact will depend on the amount of the contact force and the number and physical nature of the contact spots. As the normal force increases, the number and the area of these metal-to-metal contacts also increase by disrupting more oxide film. However, the real contact area is still only a small portion of the nominal contact area [20].

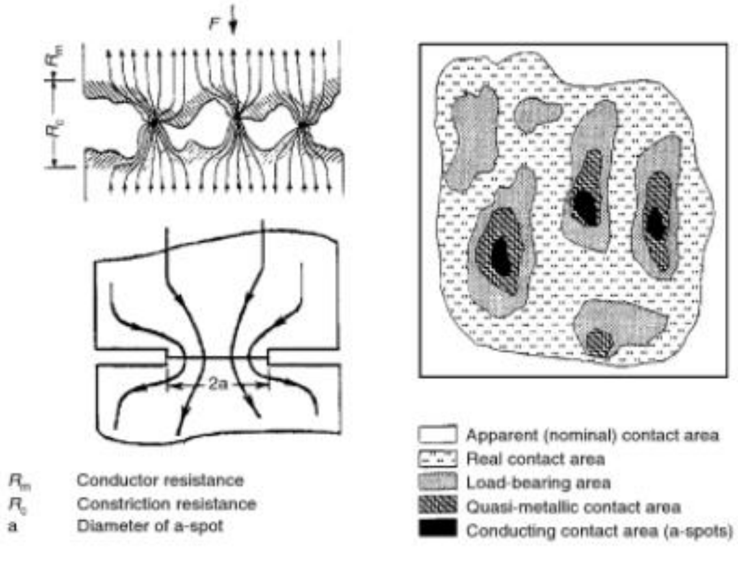

Figure 1. Schematic of real contact area and current constriction.

Figure 1 illustrates different regions that can be distinguished within the contact area. The load bearing area (A_b) represents the sum of all the small areas where the asperities of the surfaces are in contact. This area can be divided into three regions: (1) metal-to-metal contact or a-spots; (2) quasi-metallic contact, a conducting contact area with a higher resistance because of a thin oxide film; and (3) non-conducting areas covered with thick films of oxide, sulfides, and tungstenates [21].

The mechanical contact area is related to the normal force F_N applied to the electrical interface and to the material hardness H as

$$F_N = \xi H A_b \tag{Eq. 3.1}$$

where ξ is the pressure factor. This value between 0.2 and 1 depends on the amount of deformation of the surface asperities. In practical contact systems, the pressure factor is often considered equal to 1. According to Holm [22], the hardness can be expressed in relation to the material yield stress (σ_y) as

$$H = 3\,\sigma_y \tag{Eq. 3.2}$$

Therefore, the real area of mechanical contact is independent of the dimensions of the contacting surfaces depending only on the contact force and the hardness of the softer material involved in the contacting bodies.

As shown in figure 1, the electric current is constricted to flow through the individual a-spots at the contact interface. This generates an important contribution to the total contact resistance (R_C) by the so-called constriction resistance (R_E). Often, the current passage is also affected by a thin oxide and other inorganic films or adsorbed molecules that can be present on the metal surfaces due to insufficient cleaning, causing other contribution to the R_C called film resistance (R_F). The contact resistance is given, then, by

$$R_C = R_E + R_F \tag{Eq. 3.4}$$

For a monometallic electrical contact with a large number of well-distributed a-spots, the constriction resistance can be approximated by the following expression even for non-circular spots

$$R_E = \frac{\rho}{2\,a} \tag{Eq. 3.5}$$

where ρ is the specific electrical resistivity and a the radius of the metal-to-metal contact area. This resistance is related to the normal contact force as

$$R_E = K\,{F_N}^{-n} \tag{Eq. 3.6}$$

where K and n are constants dependent on basic properties of materials such as hardness and Young's Modulus. The exponent can take values from 0.3 to 1 depending on the deformation behavior of the surface material. For instance, n is equal to ${}^{1}/_{3}$ for ideal elastic materials and ${}^{1}/_{2}$ in case of plastic deformation without the presence of impurity layers.

Equation 3.7 shows an expression for the film resistance. In most practical applications, this resistance represents a minor contribution to the contact resistance because, as previously said, to form the a-spots the oxide film is usually ruptured.

$$R_F = \frac{\sigma}{\pi\, a} \qquad \text{Eq. 3.7}$$

In this equation, σ is the resistance per unit area of the film and a is also the radius of the a-spots [4,20,22].

High contact resistances can cause localized Joule heating and thereby, an important rise in temperature, which can also result in oxidation at the a-spots. Although these areas represent a small fraction of the contact area, about one or two orders of magnitude less than the real contact area, they strongly affect the reliability of the electrical contact, determining its quality and stability [21].

3.2 Electrical Connectors

An electrical connector provides a separable interface between two subunits of an electrical system in order to carry a signal or to distribute power [9,14]. There are three types of electrical connectors: wire-to-wire, wire-to-device/board, and board-to-board connections. The first one is generated when two terminal wires are connected to form a circuit. In a wire-to-board connection, wire terminals are inserted into printed circuit boards (PCB). Finally, board-to-board connectors are used for connection of PCBs and other electric components. Automotive connectors are also divided into two types: sealed and unsealed. Sealed connectors are commonly used in engine compartments due to the severe environmental conditions and un-sealed connectors are for other applications inside the vehicle [3,23].

3.2.1 Connector Structure

Wire-to-wire connectors consist of a pin or tab terminal (male part) and a receptacle terminal (female part). The male part is inserted into the female part, where the spring elements applied a normal force to the pin surface in order to establish an electrical contact.

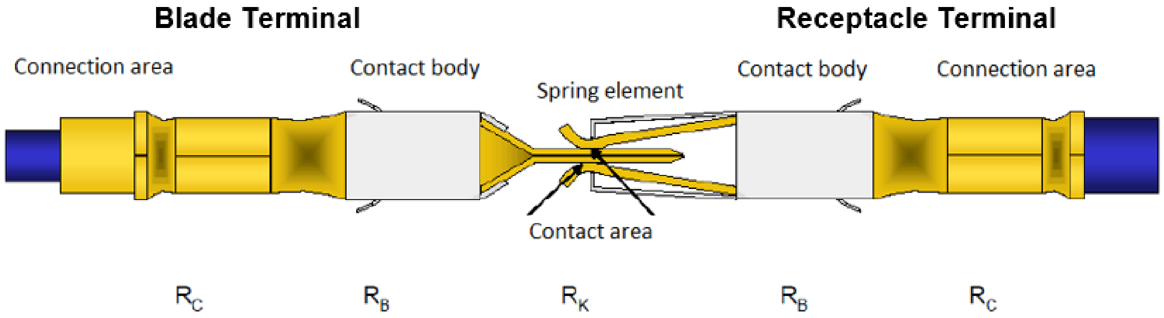

Figure 2. Schematic illustration of a typical blade connector indicating the major structural parts [24].

As shown in Figure 2, two or more spring elements are placed on opposite sides and are fixed on one end being able to move on the end where the pin is inserted. Contact pins of wire-to-wire connection are commonly blade-shaped with a chamfered edge or tip. Isolated wires are connected to both terminals by soldering or crimping. Each of these zones has an electrical resistance that contributes to the total resistance against the passage of current. In the figure, R_C represents the resistance of the connection between the wire and the terminal; R_B is the bulk resistance of the contact materials and R_K is the resistance introduced by the separable interface (or contact) [25,26].

In general, both terminals are protected by a plastic housing, which also performs electrical and mechanical functions. The housing insulates the contact from one another while providing mechanical guides for mating and protection against mechanical damage and detrimental fluids or solids of the environment [9,27].

3.2.2 Spring and coating materials

The material selection for the spring element involves a compromise between cost, mechanical performance, electrical properties and physical size constraint. Some desired properties for the contact material are low electrical resistance; high thermal conductivity, wear resistance, fatigue resistance and corrosion resistance [28]. Copper alloys are often used as basis material due to a high electrical conductivity and a large range of mechanical performance and cost depending on the alloying elements (Zn, P, Ni, Al, Zr, Ti, Cr, Mg, Co).

The contact is typically plated in order to increase the wear resistance, to protect it from corrosion and to enhance the conductivity. Two main types of contact finishes can be distinguished: noble metals (Ag, Au, Pd and alloys of these metals) and non-noble metals (primarily Sn or Sn/Ni) [9,23,29]. Silver is used in high-power contacts because of its high electrical conductivity, while both gold and palladium are used in electronic for low-power applications. Gold has the highest resistance to corrosion, because is the most noble metal, but has a poor hardness and therefore, is alloyed with cobalt, nickel or iron to enhance its mechanical properties. Since gold does not form oxides, very low contact forces are needed to establish contact between the surfaces. The main disadvantage of gold is its high cost and its price-dependence on the stock market. Tin and tin-lead alloys are very common in automotive applications, or where solderability is important, due to its low cost. Nickel is most often used as an underplate for acting as corrosion barrier [30-32].

Tin metal is silver-white, soft, ductile, nontoxic, with excellent corrosion resistance in air, lubricity, and ability to form many useful alloys. It has a low melting point of 231,9°C, which is high enough for most application conditions and enables an easy manufacturing [33]. Tin shows good performance during soldering since molten tin has a good wetting and adherence to steels as well as copper and copper alloys [34-36]. Moreover, tin is highly abundant and its main advantage is its low price.

There are two allotropic forms of tin depending on temperature and pressure conditions: white (β) and gray (α) tin. White β-tin is the allotrope stable at room temperature, it is ductile and has a body-centered tetragonal crystal structure. Upon cooling below 13.2 °C, β-tin transforms into grey α-tin, which has a face-centered cubic structure with a density considerably lower than β-tin. The allotrope α is a semiconductor. Furthermore, this transition involves a volume increase of about 27% and is known as tin pest due to the deterioration that represents. The α-tin product is brittle and readily crumbles into powder. Although tin pest can form at a temperature below 13 °C, the phase transformation rarely occurs unless, for instance, the tin oxide surface layer is removed or the material undergoes a prior deformation. Once small nuclei of α-tin appear, the maximum rate of tin pest formation occurs at temperatures between −30 °C and −40 °C. The tin pest can arise on plated electrical connectors exposed to low temperatures during storage causing the degradation of the connectors [35,37,38].

Tin is prone to exhibit spontaneous whiskers growth, which also represents a serious reliability problem in electrical and electronic devices. A tin whisker is a single microscopic crystal filament that grows spontaneously from the surface. Whiskers are highly conductive and readily results in an electrical short out by bridging gaps between electrical conductors nearby. The average growth rate of tin whiskers is close to 0.1 $Å.s^{-1}$ under ambient conditions and they can achieve lengths from few microns to over 20 mm. In addition, the shape of whiskers can vary considerably. The main factors that cause whisker growth are those that increase stress or promote diffusion within the tin plating layer such as grain size, surface oxide, residual and external compressive stresses, elevated temperature and humidity, thermal expansion coefficient mismatch and especially, intermetallic compound formation. Under certain conditions the internal stress can reach a critical level, leading to the formation of whiskers as a way of reducing the system’s internal energy [39-44]. The whisker growth can be mitigated either by using a nickel layer between the copper substrate and the tin coating, by reflowing, or by using hot-dip tin plating instead of electroplating [36].

Besides promoting the formation of whiskers, intermetallic compounds (abbreviated as IMC) can cause degradation of electrical and mechanical properties of the contact jeopardizing the reliability of the electrical connector [45]. The interfacial diffusion between the basis material and the tin plating layer results in the formation of a Cu-Sn intermetallic layer, which is comprised of two phases Cu_3Sn (ε) and Cu_6Sn_5 (η). In particular, the Cu-rich ε-phase grows adjacent to the copper substrate and the η-phase adjacent to the tin layer [46]. The binary phase diagram of the Cu-Sn system is shown below in figure 3.

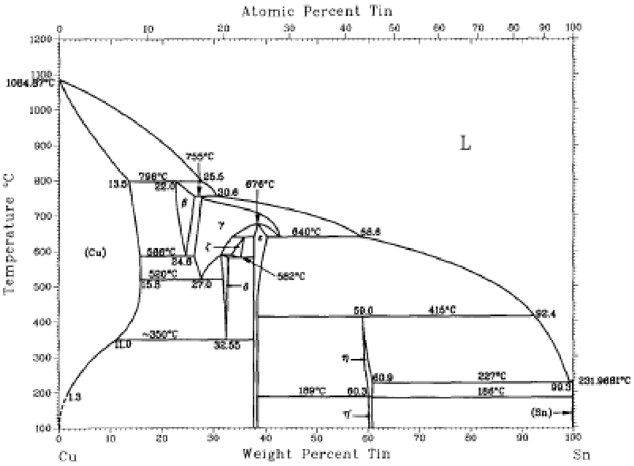

Figure 3. Cu-Sn Binary Phase Diagram. The system is characterized by a series of peritectic reactions and the formation of intermetallic phases. The structure of the ε phase is orthorhombic. η' is hexagonal with a superlattice based on the NiAs-type structure. Upon heating, at a temperature between 186 and 189°C, η' transforms into η, which has the conventional NiAs structure [47,48].

The formation of the intermetallic phases becomes an important issue in view of the fact that the operational conditions of the electrical connectors are highly critical, mostly because of the elevated application temperatures (over 100°C) and the high electrical currents, which in turn increases the temperature due to the joule effect.

Table 1. Properties of Cu, Sn and their intermetallic compounds at room temperature [50]

	Cu	Sn	Cu_6Sn_5	Cu_3Sn
Hardness VHN (MPa)	369	51	378	343
Elastic Modulus (GPa)	115	47	85.6	108.3
Thermal Expansion (PPM/°K)	16.5	23	16.3	19
Heat Capacity (J/g°K)	0.385	0.226	0.286	0.326
Resistivity (µΩ.cm)	1.7	11.6	17.5	8.9
Density (g/cm^3)	7.96	6.97	8.28	8.90
Thermal Conductivity (W/m °K)	401	66.8	34.1	70.4

The IMC are harder than pure tin and inherently brittle, thus tends to failure easily [49, 50]. Furthermore, the IMC may degrade the current-carrying capacity of the contact as their thickness increase [51]. Although there is no strong difference in the electrical resistivity between tin and the intermetallic compounds (see table 1), the presence of the intermetallic layer contributes to the contact resistance by increasing the constriction resistance and through its influence on the surface oxides that are formed [52].

The growth of IMC is a diffusion-controlled process. The phase η', Cu_6Sn_5, forms spontaneously at room temperature after a long storage time, while the Cu-rich phase, Cu_3Sn, starts to grow at temperatures above 60°C at both Cu/Cu_6Sn_5 and Cu_6Sn_5/Cu_3Sn interfaces. At the Cu/Cu_6Sn_5 interface, Cu can react with Cu_6Sn_5 to form Cu_3Sn and hence Cu_3Sn increases in thickness at expense of the Cu_6Sn_5 phase. At the same time, Sn may diffuse to the Cu/Cu_3Sn interface and react with Cu to form Cu_3Sn [53, 54]. The rate of copper mass transport in tin coatings at lower temperatures is controlled predominantly by grain boundary and defect diffusion. At elevated temperatures, the bulk diffusion becomes the predominant growth mechanism. Moreover, the growth rate of the intermetallic layer in most cases does not follow the typical $x^2 = k.t$ relationship, where x is the IMC thickness after a time t and k is a rate constant. It has been proposed that the growth rate is linear and the reduction rate of Cu_6Sn_5 due to Cu_3Sn is parabolic [45, 55].

The growth of Cu3Sn is accompanied by the formation of micropores mainly within the intermetallic phases. These micropores, also called Kirkendall voids, arises due to the volume difference between Cu_3Sn and Cu_6Sn_5. Furthermore, the diffusion of Cu to the Cu/Cu_3Sn is much slower than the diffusion of Cu from Cu_3Sn into Cu_6Sn_5, which cannot be compensated by the inverse diffusion of Sn through Cu_3Sn/Cu_6Sn_5 interface. This unbalanced diffusion results in vacancies that condense to form Kirkendall voids. This effect may induce premature mechanical failures of electrical connectors [56-58].

In many cases, where the electrical devices are exposed to harsh operating environments, especially to extreme temperatures, the use of a diffusion barrier such as a nickel undercoating is often warranted. This nickel layer prevents the migration of copper to the surface. Moreover, the growth rate of SnNi intermetallics is far slower than for SnCu intermetallics [59]. It has been shown that the nickel suppresses the formation of both intermetallic phases, but is more pronounced for the ε-phase [60-63].

The tin plated surface is usually covered with oxide films such as SnO and SnO_2, which prevent further corrosion or other direct chemical surface reactions. These oxides present high electrical resistance and, therefore, should be broken down by a high normal force in order to establish a proper and stable electrical contact [64].

Tin-plated copper contacts are susceptible to fretting corrosion when the contact force is low, which represents the principal cause of electrical connectors failure. Due to oscillatory movements of small amplitude oxide debris tends to accumulate in the contact zone causing an increase in the contact resistance. These relative movements of the contacting components may be produced by either external mechanical vibrations, differential thermal expansion of the contact materials or load relaxation. Hence, it is important to attain mechanical stability for prevention of the motion at the contact. For instance, this can be achieved by high contact forces and large interface areas. In addition, the use of lubricants can retard the wear rate and thus, stabilize the contact resistance [65-69].

3.2.3 Manufacturing Process

The manufacturing process has an important influence on the surface roughness and, therefore, on properties such as contact resistance, insertion and withdrawal forces, etc. Three stages can be distinguished in the manufacturing process of electrical connectors: hot-rolling process of copper strip, stamping/bending and surface finishing [3].

There are several coating techniques such as electroplating, cladding or hot dipping. By electroplating, the corresponding plating material is applied to the base metal by using an electric current to promote an electrochemical reaction. During cladding, the coating material is mechanically bonded to the base metal. Finally, in hot-dip plating, the base metal passes through a molten bath of the plating material. After leaving the bath, the coating is still liquid and adheres to the copper strip. The desired thickness is achieved by hot air leveling before the coating solidifies [32].

The coatings obtained by hot-dip tinning are dense and homogeneous since they solidify from a molten bath. Typical for these coatings is the formation of the intermetallic compounds, which arise immediately at the Sn-Cu interface upon contact of the liquid tin with the copper strip [70]. As a result, a good bonding between the basis material and the tin layer is generated. Moreover, excellent resistance to whisker formation is achieved because of a low internal stress. In general, hot-dip tinned coatings tend to have higher surface hardness and higher abrasion strength compared to electroplated coatings, in addition to good formability and solderability [71, 72].

In contrast, the coating obtained by electroplating presents a specific column crystal-structure, which tends to have pores and impurity inclusions. Another important difference between both techniques lies in the formation of the IMCs. No intermetallic forms during tin electroplating. There is a certain time until the intermetallic compounds appear since their growth depends on time and temperature. One of the advantages of electroplating is that no limitation is imposed on the thickness of tin that can be applied and the base material can be covered with several intermediate layers to improve the properties. The required thickness can be attained by adjusting the bath parameters, applied current and time. The main disadvantage is the elevated residual stresses that trigger the growth of whiskers. After electroplating, the coating can be subjected to a thermal treatment during which the tin is remelted (EPR = electroplated reflow). This results in the formation of intermetallic phases and also reduces internal stresses, which makes the coating less susceptible to whisker formation [72-74].

3.3 Laser Texturing

3.3.1 Fundamentals of laser light

The word LASER is an acronym for Light Amplification by Stimulated Emission of Radiation. The laser light is characterized by some properties that set it apart from the white light:

- monochromaticity: the laser light consists of a single wavelength, or frequency, i.e. the laser emits all photons with the same energy;
- high coherence: the laser light is both spatial and temporal coherent, which means that the wavefronts are in phase;
- high directionality: the laser beam presents a low divergence due to the fact that the laser cavity is constructed by two parallel mirrors which constrain the beam to a path perpendicular to them;
- high intensity: the high level of collimation results in high energy density (energy per unit area, fluence).

Basically, the laser is formed from three parts: an active/gain medium, placed in an optical cavity, which consists in two parallel and highly reflecting mirrors with one of them partially transmitting, and an energy source for laser pumping. The active medium allows the amplification of the light wave passing through it. This can be gaseous, liquid or solid. Neodymium is a common dopant in various solid-state laser crystals, including neodymium-doped yttrium aluminium garnet (Nd:YAG), which is the most widely used. The optical cavity, or resonator, functions as a feedback mechanism for light amplification and, moreover, constrains the range of frequencies that can be amplified. Finally, the pump source transfers energy to the active medium to excite electrons to higher energy levels and thereby, achieve a population inversion. The pumping mechanism can be optical, electrical discharge, passing current, or electron bombardment [75-80].

Particles can interact with light by absorbing or emitting photons. Normally, electrons of the atoms of the active medium reside in the ground state (with an energy E_1) with the lowest energy. The majority of these atoms can be excited to an upper state (E_2) by pumping energy. After a short time, the electrons decay back to the ground state emitting photons with an energy $hf = E_2 - E_1$, where h is the Plank constant and f the frequency. According to Einstein, the emission may be spontaneous or stimulated by radiation incident on the excited atom. The latter occurs when a photon from spontaneous decaying induce an electron in the excited state to decay to the ground state by emitting another photon. Since this photon has the same frequency, phase, and state of polarization as the stimulating photon, they add constructively resulting in an increase in amplitude [77, 81]. To generate the laser, the stimulated emission has to dominate over both self-absorption and spontaneous emission. Therefore, the lasing system has to be in population inversion by going beyond the thermal equilibrium, with more atoms of the active medium in the excited state than in the ground state [82].

Further amplification is obtained through the optical cavity by reflecting the photons into the active medium. The photons travel the long path back and forth through the active medium resulting in a subsequent high-intensity laser output. To initiate and sustain the laser oscillations, the gain within the resonant cavity must be high enough to overcome various losses, such as diffraction from the edges of the mirrors, absorption and scattering by the mirrors, absorption and scattering in the laser medium, etc. [83].

Today lasers can generate light either continuously or in form of pulses. Pulse durations of nanosecond or even shorter can be obtained by means of techniques such as Q-switching or mode-locking respectively. In the Q-switching mode, there is an important growth of population inversion by increasing the losses in the cavity. When the losses are switched to a lower value, there is a release of energy in form of an intense and short pulse.

3.3.2 Laser-matter interaction

When light strikes a surface, a portion will be reflected at the interface and the rest will be transmitted into the material. The reflectivity of the material will depend on the frequency of the incident light through the dispersion relation of its refraction index. Part of the transmitted light will be absorbed. In general, the light intensity (I) will decay with depth (z) following the Beer-Lambert law $I = I_o \, e^{-\alpha z}$, where I_o is the intensity just inside the material after corresponding reflection and α is the absorption coefficient. The latter is a function of the light wavelength and temperature. The absorption depth δ, or optical penetration, is defined as the depth at which the intensity drops to ${}^{1}/_{e}$, and can be calculated as $\delta = {}^{1}/_{\alpha}$. Hence, local surface modification without altering the material bulk can be achieved by choosing wavelength with short absorption depths. The absorption of nanosecond pulsed lasers is most typically due to single photon interactions. Femtosecond or shorter pulsed lasers can induce optical breakdown or multiphoton absorption which reduces significantly the absorption depth [84].

The specific mechanism by which the laser light interacts with the matter will depend on the parameters of the laser beam and the properties of the material. Laser parameters are wavelength, intensity, spatial and temporal coherence, polarization, angle of incidence, and dwell time. Energy density, or rather, fluence, should be considered instead of intensity for pulsed-laser irradiation [85].

In general, photons will couple into available electronic or vibrational states in the material depending on their energy. Ideal semiconductors and insulators are commonly transparent, but if the frequency of the electric field matched to the resonance frequency, photons can then be absorbed through resonant excitations such as electronic transitions within one band (intraband) or between bands (interband). These excited electronic states can transfer energy to lattice phonons. In metals, the laser light is absorbed by acceleration of free electrons. The energy is subsequently either re-emitted or transferred to the lattice by collisions. In both cases, the phonon generation leads to lattice heating and melting. The necessary time to thermalize will then depend on the specific material. For most metals, it is on the order of 10^{-12} to 10^{-10} s. Three different laser-induced processes can be observed depending on the laser excitation rate. When the laser-induced excitation rate is lower than the thermalization rate, the process is referred as photothermal. The absorbed laser energy is directly transformed into heat and hence, the material response can be treated in a purely thermal way. When the laser-induced excitation rate is high compared to the thermalization time, non-thermal process takes place. This type of material modification is typically referred as photochemical since the elevated excitation energies can break bonds resulting in photo-decomposition. During a purely photochemical process, the temperature remains practically constant. If both thermal and non-thermal mechanisms are significant, the laser-induced process is denoted as photophysical. For instance, laser processing of metals and semiconductors with nanosecond laser pulses results in photothermal effect. Femtosecond laser pulses can enable photochemical processing [84,86].

Different material responses can occur depending on the laser fluence. Fluences below the melting threshold can activate chemical reactions, phase transformation, and other diffusional processes. In addition, material self-quenching and thermal stresses can arise during localized laser heating due to the large temperature gradients generated. When the stress exceeds a certain value, the material may fracture and/or deform plastically. Higher fluences cause the material to melt and vaporize when the surface temperature exceeds the melting and boiling point respectively. When the laser fluence reaches a certain threshold, the material immediately vaporizes and ionizes forming plasma. Material removal, or ablation, can occur by direct absorption of sufficient high laser energy. Thermal (evaporation and sublimation) and non-thermal (photochemical) ablation mechanisms are observed depending on the material system and laser processing parameters such as wavelength, fluence and pulse length [84,87].

Figure 4 shows an overview of different application areas of the laser processing depending on the laser intensity and the interaction time.

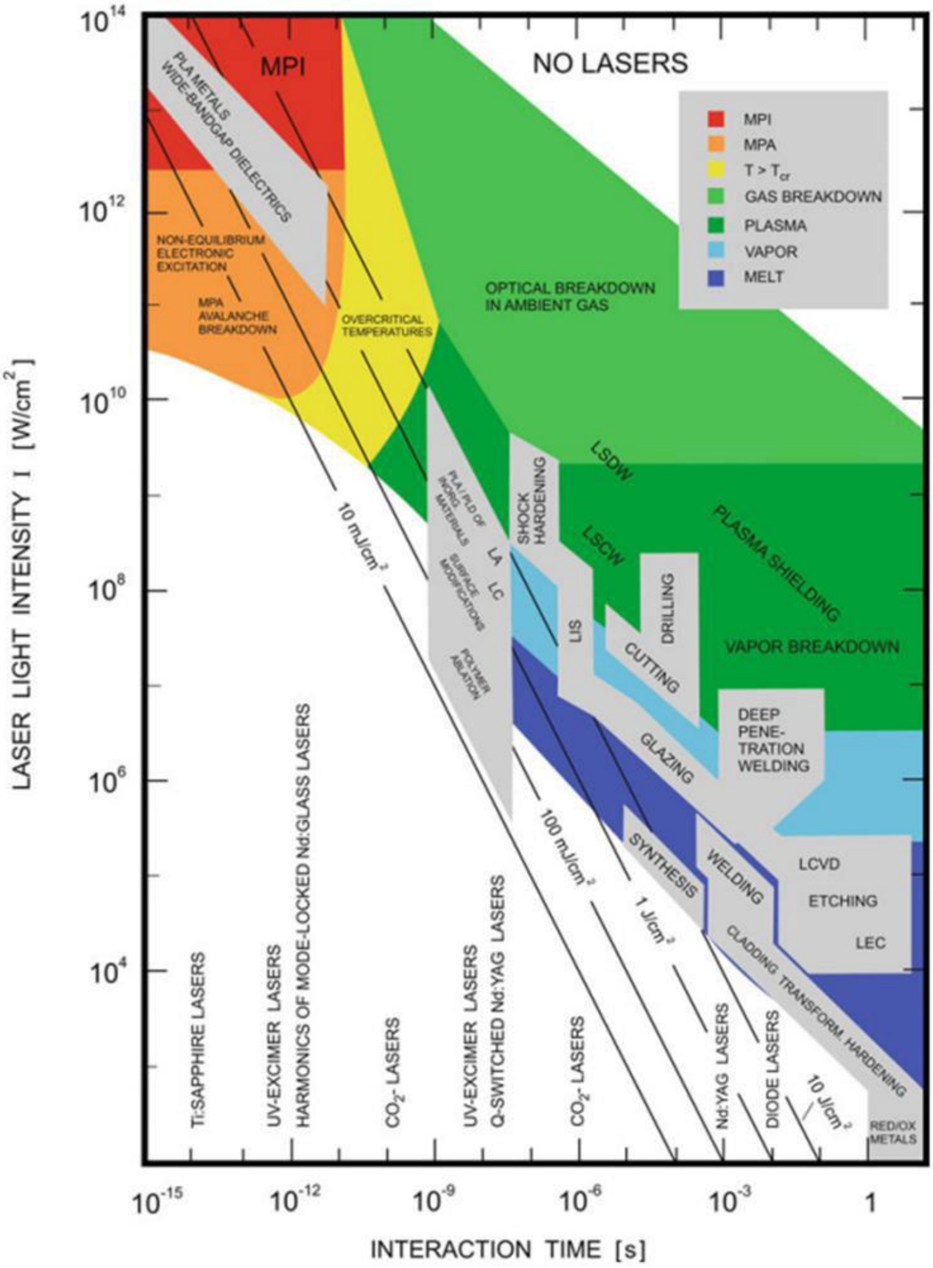

Figure 4. Applications of lasers in materials processing depending on the parameter regime employed. MPA/MPI: multiphoton absorption/ionization. PLA/PLD: pulsed-laser ablation/deposition. Surface modifications include laser-induced oxidation/nitridation of metals, surface doping, etc. LA: laser annealing. LC: laser cleaning. LIS: laser-induced isotope separation/ IR-laser photochemistry. LSDW/LSCW: laser-supported detonation/combustion waves. LCVD: laser-induced chemical vapor deposition (CVD). LEC: laser-induced electrochemical plating/etching [85].

In particular, material melting is typically achieved with laser intensities between 10^3 and 10^8 W/cm^2 and irradiation times from 1 to 10^{-8} s. These relatively lower intensities enable the processing of large areas by using unfocused laser beams. Nd:YAG lasers are most commonly used for this purpose [85]. A novel laser processing technique that has been gaining importance in the last 20 years as a promising industrial tool is the direct laser interference patterning [88], which will be covered in the following section.

3.3.3 Direct Laser Interfering Patterning

Direct Laser Interfering Patterning (abbreviated as DLIP) is an emerging technology that allows the creation of periodic surface arrays with a well-defined long-range order in a micro/nanoscale. This method is based on the beam interference of a high-power pulsed laser. A sample is irradiated with laser beams and the interference pattern generated on the surface induces a periodical local melting due to local photo-thermal interaction between laser and material. The material replicates the interference pattern as a result of the Marangoni effect and hence, a periodical surface texture is obtained. Figure 5 shows an outline of the DLIP process. Only a small layer of material below the surface participates on the process, which corresponds to the penetration depth of the laser radiation. Typically, for metals, this layer has a thickness of about 10 nm [89, 90].

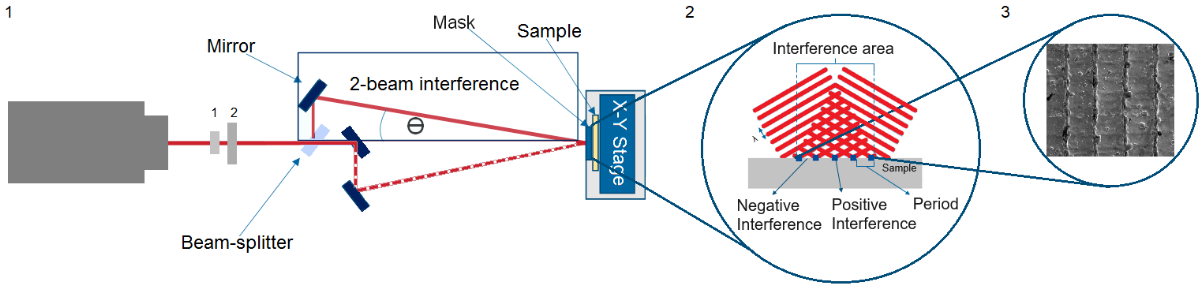

Figure 5. 1. Schema of conventional DLIP setup for ns-pulsed laser systems. The setup includes beam attenuator (1), shutter (2), beam splitter and mirrors. In this case, a primary beam is split into two sub-beams. These sub-beams are overlapped through a quadratic mask transferring the interference pattern to the sample surface. 2. DLIP principle. 3. SEM-image of a typical lineal-like surface pattern obtained by two-beam interference.

For a multiple-beam interference pattern, the intensity distribution (I) of the interfering laser beams is given by

$$I = \frac{c\,\epsilon_0}{2}\left|\sum_{j=1}^{n} E_j\right|^2 \qquad \text{Eq. 3.8}$$

where c is the speed of light, ϵ_0 the vacuum permittivity and E_j are the components of the light wave field [91].

As shown in figure 5, a line-like pattern is obtained in the case of two-beams interference ($n = 2$). The intensity distribution can be expressed as

$$I = 2c\epsilon_0 {E_0}^2 \cos(kx\, sin\, \theta)^2 \qquad \text{Eq. 3.9}$$

where 2θ is the angle between the beams and E_0 is the amplitude of the electric field of the beams assuming $E_{01} = E_{02}$. Equation 3.9 shows that the interference of two laser beams results in a sinusoidal intensity distribution (see figure 6 a).

By interfering three laser beams, different 2D arrays can be produced depending on the electric field of each beam and the geometric configuration. As can be seen in figure 6 (b), a hexagonal dot-like interference pattern can be obtained for a symmetric configuration.

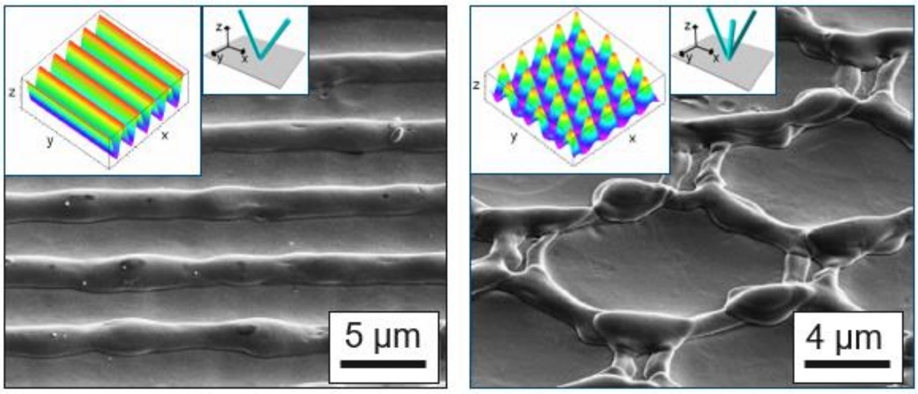

(a) (b)

Figure 6. SEM-images of textured stainless steel substrates: (a) Two laser beam interference and (b) Three laser beam interference [90]. The embedded figures in (a) and (b) represent the corresponding calculated intensity distribution [93].

The spatial period (P) of the interference pattern produced by two laser beams is given by

$$P = \frac{\lambda}{2\sin\theta} \qquad \text{Eq. 3.10}$$

The period can then be described in terms of the angle θ between the interfering beams and the wavelength λ of the light source. The higher the angle θ, the smaller the period of the surface structure. In a similar way, small periods derive from small radiation wavelengths. Theoretically, the smallest period that can be reached corresponds to the half of the wavelength. However, in order to obtain a regular pattern, the period should be larger than the thermal diffusion length (l_T) determined as

$$l_T = \sqrt{\kappa\tau} \qquad \text{Eq. 3.11}$$

where κ is the thermal diffusivity and τ the frequency of the ns-pulsed laser irradiation. The thermal diffusion length provides an idea of the distance in which the heat generated by the laser irradiation at the interference maxima spread out [90].

The absorption behaviour of the samples may also contribute to the energy input and the resulting structure. In absence of microstructural and chemical changes, the absorbance in metals is basically controlled by the number of free electrons, the interband transitions, and the surface roughness. The latter has a strong influence on absorption due to multiple reflections at the surface undulation [94].

Furthermore, the texture is determined by the laser fluence. According to Lasagni [94], three different topographic regimes take place depending on the laser fluence in the case of a sample consisting of two layers. The texture obtained for each regime is presented in figure 7.

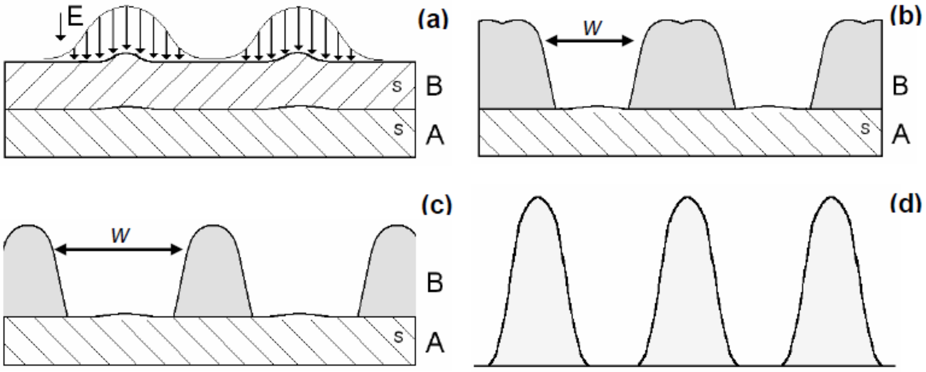

Figure 7. Schematic drawing of the sinusoidal-like topography obtained by laser texturing in case of a substrate consisting of two layers. The layer A has a higher melting point than the surface layer B. (a) Low values of laser fluence induce thermal dilatation of layer B. (b) Higher fluences cause the melting of layer B at the interference maxima and (c) if the fluence increases, the width of the removed area also increases. (d) Both metallic layers are molten and removed from the interference maxima.

In figure 7, material A has a higher melting point that material B. In the first regime, at low laser fluences, the texturing process is carried out without removal of material at the interference maxima positions. The structure arises only because of a deformation in the maxima caused by the high thermal gradient (figure 7 a). This regime is characterized by a very homogeneous texture. In the second regime, the surface is partially molten at the interference maxima. Due to the large temperature gradient generated between minima and maxima, the molten material flows towards the interference minima leading to the formation of the structure. This is caused by the so-called Marangoni convection whereby the surface tension gradient between interference minima and maxima drives a mass transfer to the minima. The molten material solidifies while moving due to extreme cooling rates [95]. This regime displays a non-homogeneous texture and a rise in the structure depth compared to the first regime (figure 7 b). The term non-homogeneous indicates that the resulting topography height is not constant along the symmetrical axis of the periodical pattern. If the laser fluence is further increased, more material is removed from the interference maxima and therefore, the texture minima increase in width (figure 7 c) until both layers are molten (figure 7 d). For elevated fluences arises a fall of the structure depth because the energy density is high enough to locally vaporize the metal at the interference maxima positions. Consequently, begins the third regime of ablation.

For pulsed laser, the laser fluence (F) can be calculated as

$$F = \frac{p}{f\ M\ A}\quad \left[\frac{J}{m^2}\right] \qquad \text{Eq. 3.11}$$

where p is the laser power measured by a power meter after the attenuation of the primary laser beam (W), f is the frequency (Hz), M is the lens magnification and A is the laser beam area (m^2).

Moreover, secondary metallurgical processes such as recrystallization, recovery, IMC formation and other phase transformation can be induced by this processing technique due to the high laser intensity distribution of the interfering laser beams and significant heating/cooling rates [95].

3.4 Previous Work

As previously mentioned in the introduction, the demands on connector materials have been recently increased driven by the trends in miniaturization and electrification of vehicles parts, requiring lower and constant electrical contact resistance and lower contact normal loads. Particularly, electrical connector installation and maintenance are manual operations and thus, also require low and stable insertion and withdrawal forces.

Leidner et al. [16] have developed different contact designs in order to obtain a pronounced reduction in the contact resistance. It has been shown that there is a difference between the current density (J) distribution and the surface pressure distribution for a Hertzian electrical contact interface. Numerical simulations have demonstrated that the a-spots located near the outer rim of the contact area are most vulnerable to exhibit excessive current densities. On the other hand, the a-spots bearing the greatest surface load are located in the central region of the contact area. In addition, degradation initiates at the outer rim, even though it has the lowest mechanical load [16, 96].

By matching both current density and surface pressure distribution it is possible to reduce the electrical contact resistance by a factor of up to 2. This can be explained by the increased mechanical pressure that leads to the rupture of the oxide layer covering a-spots.

According to Leidner, a contact surface with a sinusoidal shape has a huge potential to be designed into real contact systems for reduction of contact resistance. Figure 8 shows the results obtained by simulating the change of the constriction resistance as function of the contact surface design. Figure 8 (a) shows the influence of topography wavelength (λ) on constriction resistance. This curve was obtained by simulation of the contact between a Sn coated half-spherical sample with a diameter of 1.5 mm and a flat surface with a sinusoidal groove texture with wavelengths/periodicities between 0.014 and 4 mm. Four different regions can be identified depending on λ. Surfaces with λ larger than 1.5 mm are considered as hertzian contacts because their mechanical response follows Hertz contact theory. This type of surfaces shows a range of contact resistance of about 0.9 mΩ (grey zone). Wavelengths ranging from 0.75 to 1.5 mm show the highest contact resistance (red zone). In this case, the spherical sample cannot totally touch the bottom of the topography valley (figure b). The contact area is reduced, which causes an increase of contact resistance. Additionally, the ratio of electrical conductive and mechanical bearing a-spots reaches its minimum in this zone. This range of λ is easily produced by typical conforming methods like stamping. A further decrease in λ results in a rapid decrease in resistance. By reducing λ, the contact area split leaving no load bearing spots present at the mid-periphery. Hence, current density starts to match with contact pressure. When λ is further decreased, more topography maxima participate in the contact interface. The contact can then be considered as a parallel circuit, where each maximum shows a high surface pressure and therefore several electrical conducting a-spots. The production of surfaces with a wavelength of 0.2 mm or less (yellow zone) becomes impractical with the conventional conforming methods, being the subsequent coating the critical stage. Furthermore, such high surface pressures derive in a high rate of surface wear, which is undesired for connectors. In this way, the optimum range for practical use on real contacts can be postulated as 0.2 mm < λ < 0.5 mm [16, 25].

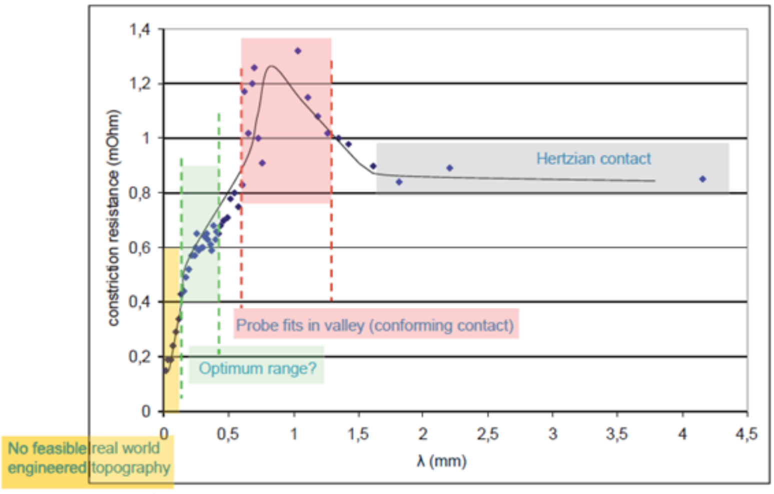

(a)

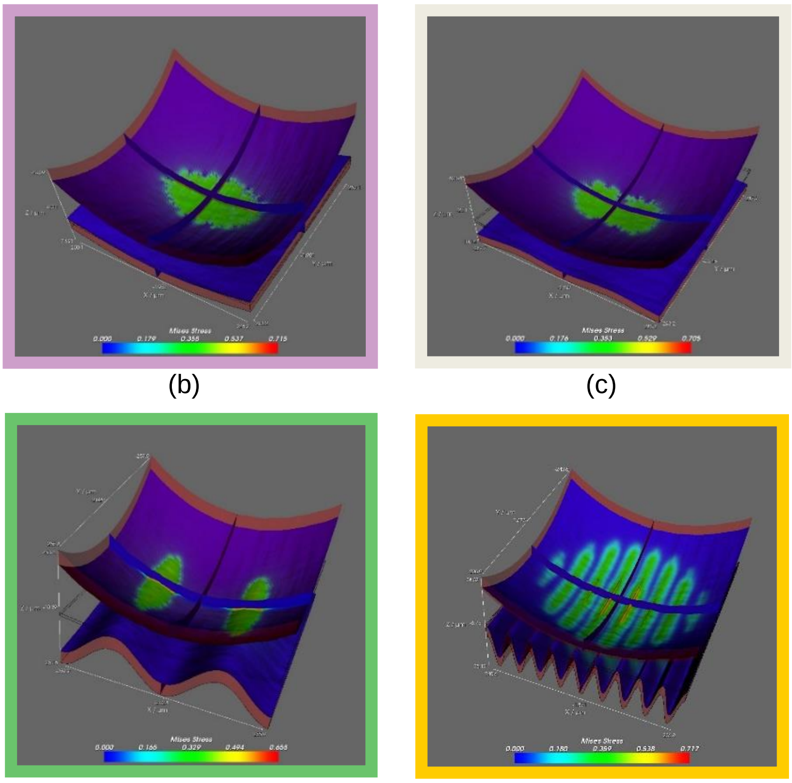

(b) (c)

(d) (e)

Figure 8. Mechanical and electrical simulation results of different electrical contact interface design. (a) Constriction resistance as function of sinus wavelength. Von Mises stress distribution F_N= 1 N: (b) Hertzian contact interface λ > 2 mm; (c) Typical forming processes 0.75 mm < λ < 1.5 mm; (d) Optimal wavelength 0.15 mm < λ < 0.5 mm; (e) Difficult to achieve λ < 0.1 mm.

Direct laser interference patterning provides an excellent way to fabricate sinusoidal surfaces with a small wavelength of the order of some µm. This method offers several advantages due to the remote and contactless operation and thus, flexibility during material processing. DLIP allows a rapid large-area fabrication of 2D or 3D structures with speeds up to several cm^2/s in a single step process, involving a rapid route to large-scale production [91]. Furthermore, DLIP can be also used for different materials including metals, ceramics, and polymers [97].

Leidner et. al have shown that sinusoidal surface texturing offers the possibility of simultaneous embedding of lubricants for reduction of friction coefficient and hence, for improving wear resistance [19]. At this point, it should be mentioned that this surface modification can be applied on both spring and pin side of the connector, regardless of the connector brand or design. Connectors can be textured on a single side or on both. However, in case of pairing a spring and a pin contact with the same sinusoidal surface topography, there would be a conformal contact, which is characterized by very low surface pressures. This, in turn, would lead to a large increase in contact resistance. Therefore, within *TE*

Connectivity exists a conceptual distinction between wave structure (period ~ 0.15 mm), which applies only on the spring side and wave texture (period ~ 0.015 mm), with sole application on the pin side [98].

In order to obtain porosity within the structure, the optimal period is approximately 15 µm. Structures with relatively small period (4-14 µm) do not present porosity, since the fronts of molten metal moving from the hot regions (interference maxima) toward the cold region (interference minima) encounter and completely overlap producing the maxima of the structure as shown in figure 9 (b). On the other hand, interference patterns with larger periods (> 16 µm) produce double-peak structure (figure 9 a). In this case, the fronts do no longer meet and solidify forming a double maximum. Only for a certain period value, the formation of pores can be observed. This occurs because the liquid metal moving towards the interference minimum still encounter fluid coming from the subsequent interference maximum but the fronts do not overlap. When the molten fronts meet, the material solidifies so quickly that the air in between cannot escape. Ideally, they should meet in one point and thus the largest pores would be produced, being possible to enclose a large amount of lubricant. In practice, because of the non-automatized optical setup, the closer period to 15 µm that could be produced was 14,83 µm.

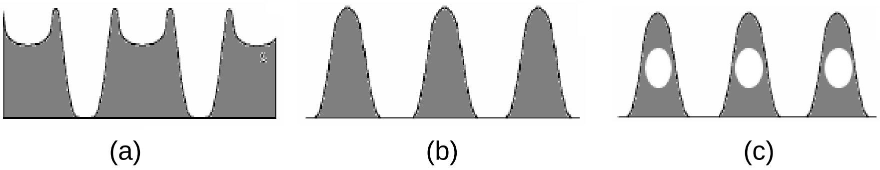
(a) (b) (c)

Figure 9. Schema of sinusoidal-like structures. Interference pattern obtained for (a) large periods; (b) large values of laser fluence and relatively small periods. (c) Optimal structure, which is intended to achieve in this work.

The present bachelor's final project is a follow-up of the work commented hereinabove. The main objective is to evaluate if it is feasible to reduce the insertion force of real electrical connectors by embedding lubricant in the texture, without compromising the electrical performance. The key aspect of this work is that all the study was conducted using directly a final product provided by *TE Connectivity*. It was the previous stage to the acquisition of a laser facility for the mill. The commercial connector system considered for the experimental part will be outlined in the following chapter.

4. Materials

The contact system for the Automotive Industry, MCON 1.2mm LL, provided by *TE Connectivity*, was used in order to study the influence of the surface texturing and the lubricant embedding on the tribological and electrical properties of real contacts.

MCON is a generation of contact systems commonly used for passenger cars and commercial vehicles, either for sealed or unsealed applications. This contact family has been designed for withstanding vibrations and mechanical stresses in various harsh environment applications, which can impact on the long-term performance and quality of the contact system. Some advantages of MCON are a redundant contact point technology for higher reliability; overstress protection of the contact springs; a contact box with polarization and secondary locking feature with three directional access, and the possibility of a protected locking lance [99].

Figure 10 shows a schema of the parts of the connectors used in this work. It also shows a picture of a real pin in order to visualize the dimensions of it.

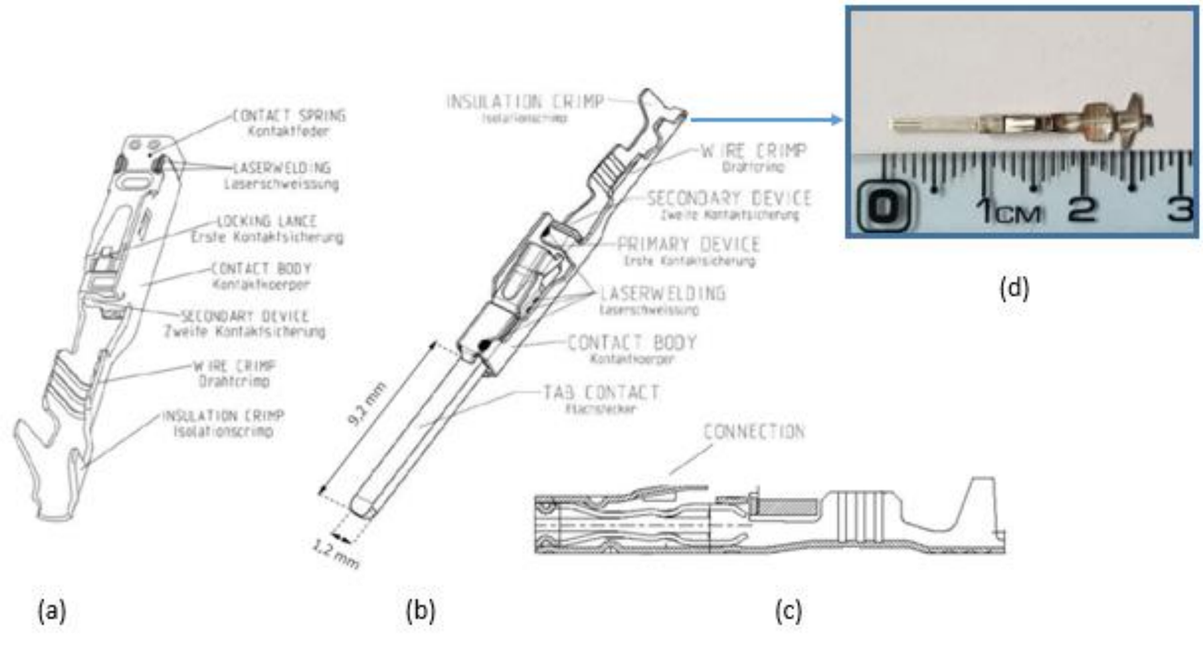

Figure 10. MCON 1.2 Contact System. Schema of (a) female contact (receptacle), (b) male contact (pin / tab), and (c) connection between the parts. (d) Photograph of a textured pin. Pin length can be 24.5 mm minimum and 26 mm maximum. The tab contact has a length of 9.2 mm.

The contact system follows a two-piece contact design strategy, which intends to separate the electrical from the mechanical performance for meeting the integrity requirements of the automotive industry. The receptacle contact (figure 10 a) consists of an outer closedbox contact spring and an inner contact body. In this way, the lamellar contact springs inside the contact system are protected against plastic deformation. The pin contact (figure 10 b) is also stabilized against rotary movements by the lamellar contact springs. Each of the four independent lamellar springs in the polarized contact generates two contact points positioned one behind the other to stabilize the position of the tab relative to the MCON 1.2. Thus, a total of eight electrical contact points are created in one MCON 1.2 contact.

The selection of materials has a main role in the proper function of this two-part contact. A combination of materials is further required to obtain optimum electrical and mechanical characteristics. The bodies of the receptacle contact and the tab contact consist of CuNiSi alloys, while the pin and the spring basis material is CuSn0.15/0.2. The surfaces of the pin and the springs are tin-plated.

The crimp-type connection is designed for contacting cables with cross-sections between 0.13 mm^2 and 1.5 mm^2. The MCON 1.2 with Sn plating can be used for a temperature range between -40°C and 130° C.

In addition, the MCON connector system offers receptacle and pin plastic housings to protect the connection. These housings are waterproof and represent a further resistance to conditions of extreme vibration [101, 102].

5. Methods

5.1 Laser Texturing

In this study, only the pin side of the electrical connectors was texturized. First, the samples were cleaned with 2-Isopropanol in an ultrasonic bath for 10 minutes. Then, they were texturized under normal atmospheric conditions (room temperature and atmospheric pressure) by using a high-power pulsed Nd:YAG Laser (Quanta-Ray PRO 290, Newport Spectra-Physics). The fundamental wavelength of the Nd:YAG Laser used is 1064 nm, but shorter wavelengths can be generated by means of frequency doubling, which reduces at the same time the laser energy. In this case, the samples were irradiated with a wavelength of 532 nm. The pulse duration was 10 ns and the repetition rate was 10 Hz.

The primary laser beam was split into two sub-beams, which were guided through an optical arrangement to the surface sample, whereon both interfered resulting in a line-like interference pattern. The energy level of the primary laser beam was adjusted with a beam attenuator and the number of pulses by means of a mechanical shutter. The intensity of the sub-beams can be regulated by changing the angle between the beam-splitter and the incident primary laser beam.

The pattern wavelength or period, defined as the distance between two adjacent topographical peaks, is a characteristic quantity of the periodical line-like pattern and can be easily varied by changing the laser wavelength or the angle between the interfering beams. As previously stated, Leidner et al. have pointed out that a period of 15 µm is suitable to achieve porosity within the peaks of the structure. Accordingly, the required distance between the different elements of the optical arrangement and, thereby, the angle was determined. Figure 11 pictures the laser interference setup used in this work.

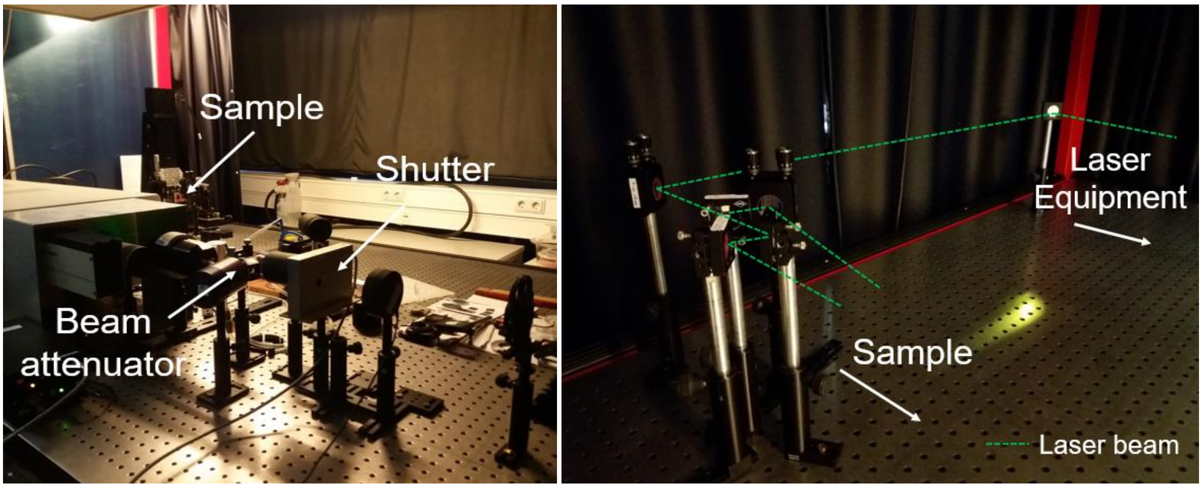

(a) (b)

Figure 11. DLIP setup. (a) Laser equipment and x-y stage for sample. (b) Arrangement of mirrors plus splitter. The laser beam path is delimited by the dashed line in green.

As figure 12 shows, the 8mm diameter laser beam is not homogeneous and therefore, the entire beam cannot be used. For this reason, the laser interference patterning was carried out selecting a certain area of the beam by means of a squared mask of 1.5 x 1.5 mm^2 (figure 12 a). As it can be seen below, the intensity fluctuations can be minimized by selecting a corresponding area (figure 12 b), but no absolutely homogeneous spot can be obtained

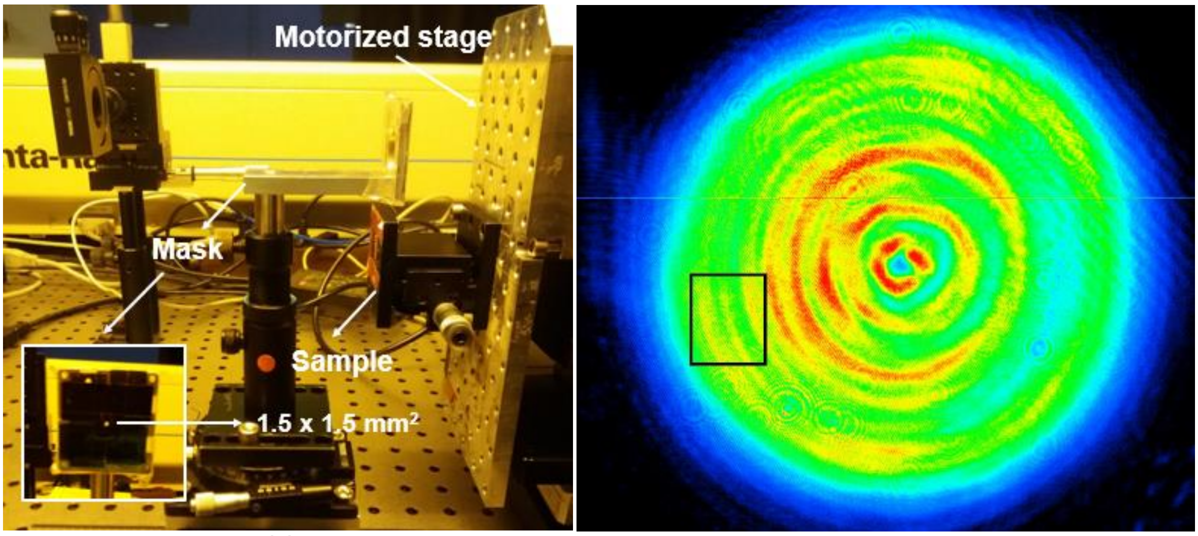

(a) (b)

Figure 12. (a) DLIP setup: mask and x-y motorized stage for sample. (b) Intensity profile of the laser beam used, which has a diameter of 8 mm. The rectangle encloses an example of an area selected for texturing [103].

It should take into account the need to place the sample as close as possible to the mask in order to minimize the diffraction effect of the edges of the mask. The sample was placed immediately after the mask on an x-y motorized stage. Due to the size of the mask, the maximum possible area, which could be textured with only one laser pulse, was 1.5x1.5 mm^2 and hence, the overlap of various laser spots was necessary to cover the total surface of the contact pins.

Different laser powers have been examined in order to find the most favorable power for the formation of pores. The laser power was measured by means of a power-meter EnergyMax Sensor J-50MB-YAG by Coherent. Once the structuring parameters were determined, three different ways of applying the lubricant before texturing were tested: simply dipping the samples into the lubricant; dipping and removing the excess of lubricant with a plastic sheet, and third, applying the lubricant by using a brush. A poly-alpha-olefin of short chain-length (PAO 40) was used as lubricant.

5.2 Surface characterization

5.2.1 White-Light Interferometry

The surface of the samples was observed and measured by means of a White-Light Interferometer Zygo New View 7300, which provides an accurate analysis of the topography without contacting the surface. The operation principle consists of the evaluation of an interference pattern between two light wavefronts. The light from a white LED splits in two within the interferometric objective: one portion reflects from the test surface and the other reflects from a reference surface in the objective. As result of the interference of both portions into a solid-state camera, arises a pattern of light and dark bands, which is analyzed by frequency domain analysis (FDA) [104]. A three-dimensional surface profile can also be calculated by moving vertically the test surface during the analysis and by correlating the recorded path with the FDA.

5.2.2 Electronic Microscopy

A dual-beam system FEI Helios Nanolab 600, where a Scanning Electron Microscope (SEM) and a Focused Ion Beam (FIB) are installed, was used to image with a high resolution the laser-structure. While the electron beam is used for imaging, the ion beam can be used both for imaging or for site-specific material removal from the sample surface. This provides the possibility for exact target preparation to analyze the microstructure below the sample surface.

Furthermore, additional instruments in the dual-beam system offer the possibility of Energy Dispersive X-ray Spectroscopy (EDX), Energy Back-Scatter Diffraction (EBSD) and Scanning Tunneling Electronic Microscopy (STEM) analysis. In this work, only EDX measurements were carried out for the chemical analysis of the samples and mainly, for the evaluation of the presence of intermetallic compounds. The EDAX system was operated with an acceleration voltage of 15 kV. The software EDAX Genesis allowed the recording of the results in form of spectra, line scans, and mappings.

5.2.3 Raman Spectroscopy

Raman spectroscopy is an important and widely used characterization tool for chemical identification. This method is based on a light scattering technique, where a photon of light interacts with the molecules of a sample to produce scattered radiation of different wavelengths. Only the fraction of the scattered photons, which has a change in the wavelength provides the chemical and structural information [105].

Raman spectroscopy was perfomed in order to assess the presence of PAO enclosed within the maxima of the obtained surface structure. Raman spectra were acquired with an inVia^{TM} Raman microscope (Renishaw). For material excitation, a Nd:YAG-Laser was used with a wavelength of 532 nm and a power of approximately 0.2 mW. The laser spot size was 5 µm. The spectral resolution was 2400 lines mm^{-1}. A 50X magnifying microscope objective was used.

First, a silicon sample was measured as standard reference in order to calibrate the Raman system knowing that the first-order Raman spectrum of monocrystalline Si presents an intense peak at 520.5 cm^{-1}. Then, a non-textured sample was measured as reference for comparison with the textured pins. Textured samples were analyzed at both topography maxima and minima. The position over the textured pin was selected using the Raman microscope, while the sample was moving with a motorized x-y table. Prior to the measurements, the samples were cleaned in an ultrasonic bath with acetone for 5 minutes and then with 2-Isopropanol other 5 minutes in order to ensure that the measured PAO 40 signal was not a signal of the remaining lubricant from the texturing process.

Finally, the spectra were plotted and analyzed using OriginPro 8.5.

5.3 Engagement Force Measurement

The engagement force of the electrical connectors was measured using a universal testing machine CADIS Prüftechnik GmbH, which has a special software to simulate the mating/unmating cycles. A force transducer of 1000N was used. Table 2 summarizes the test parameters.

***Table 2*.** Parameters of engagement force measurement.

Number of Cycles	10
Crosshead speed (mm)	50
Turning point (mm)	5
Holding time (s)	0

The terminal side of the connectors was included in a plastic housing in order to contemplate the relaxation on the measured values of the engagement force. During the experiment, it was ensured that the pins were aligned with the terminal parts in order to reduce unwanted force contributions to the total engagement force.

The surface was imaged by means of a confocal microscope Nanofocus µsurf for further characterization. In addition, the connector resistance was measured before and after each connection cycle.

5.4 Tribological and electrical characterization

5.4.1 Electrical resistance and coefficient of friction

In this work, all the electrical resistances were measured using the four-point probe method, wherein a known and controlled test current is introduced into the sample through two points while the voltage drop is measured across other two points. The resistance is calculated as the division between the voltage drop and the test current. The measurements required a dry-circuit method and the voltage-measuring points were chosen so that the voltage drop was due only to the contact resistance.

The contact resistance was measured as a function of the normal force by means of a device developed by *TE Connectivity* (see figure 13). A CuNiSi spherical contact, coated with a tin-layer of 4 µm, and with a radius of 5 mm was used as the spring contact side and pressed through a needle towards the pin surface to enable the contact. The pressing force was increased from 0.05 to 5N and the contact resistance between the spherical contact and the sample was measured by a dry-circuit four-terminal configuration, which minimized the contribution of the inherent resistance of the cables. At a normal force of 1N, the sample was moved 0.1 mm back and forth with a velocity of 0.5 mm/s, in order to break the oxide layer on the surface.

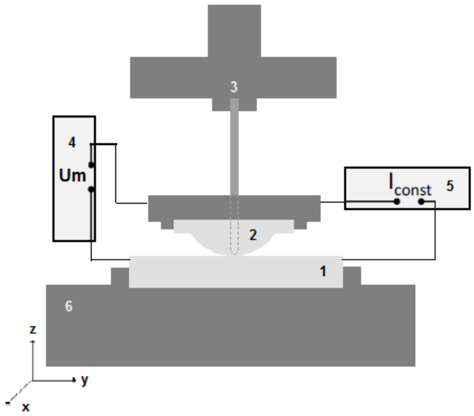

Figure 13. Schema of the device developed by *TE Connectivity* for simulation of contact between spring elements and tab. 1. Sample (pin); 2. Spherical contact; 3. Rod and force sensor for applying the contact normal force; 4. Voltmeter; 5. Current source and, 6. Motorized X-Y stage and sample holder.

The same instrument allowed the evaluation of the contact resistance and the friction coefficient as a function of the accumulative displacement at a normal force of 1 N. In this case, the displacement length was 1 mm and the sample was moved over 10 times with a velocity of 100 µm/s. Hereby, the friction coefficient is calculated as normal force divided by friction force, which are measured by the force sensor.

5.4.2 Fretting corrosion

To characterize the behavior of the samples against fretting corrosion, another equipment developed by *TE Connectivity* (see figure 14) was used, in which the electrical resistance was measured while a relative movement between the sample (pin) and a spherical contact (simulating the spring element) was carried out. As electrical resistance is considered the inherent material resistance plus the contact resistance. The first one is generally constant and as a consequence, a change in the measured electrical resistance means a change in the contact resistance. The pin was placed on the side of the device shown as “a”, which was movable in X-Y directions, and the spherical contact on the “b” side, which was movable only in Z through an adjusting wheel. A normal force of 1N was applied using a needle, which could be loaded with different weights. To ensure that there was no other contribution to the force, the sample was aligned as much as possible. The sample was moved back and forth a total of 100 µm in Y direction over 10^3 cycles.

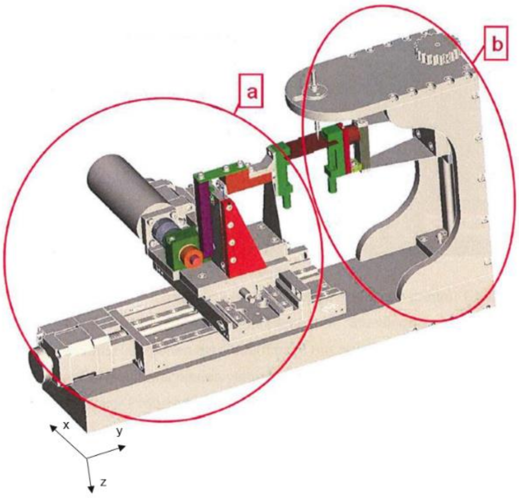

Figure 14. Diagram of the equipment developed by *TE Connectivity* for Fretting Corrosion testing [25].

The relative movement is transferred to the contact pair via an eccentric disc. Due to the high inherent stiffness required, all force-transmitting parts are designed as solid body joints [98].

In all the measurements described in 5.4.1 and 5.4.2, only pins were previously cleaned with 2-Isopropanol.

5.4.3 Derating curve

In electronic and electrical applications, derating can be defined as the reduction of electrical, thermal and mechanical stresses applied to a connector in order to decrease the degradation rate and prolong the life of the product. In other words, to ensure a reliable performance of the connector, a conservative design and operating at a lower stress condition than the part´s rating is required.

A derating-curve indicates the maximum recommended current value at a specific application temperature without failure risk [106, 107]. It can be calculated by measuring the temperature rise as a function of the current applied. Three references and three structured samples were simultaneously tested in free air conditions (see figure 15) following the standard DIN-EN 60512-5-2. The i_{max} was set as 17 A, being the limit current of the 0.7 mm^2 cable used, and the T_{max} was considered as 130°C, being the limit temperature of the connector according to the product specification.

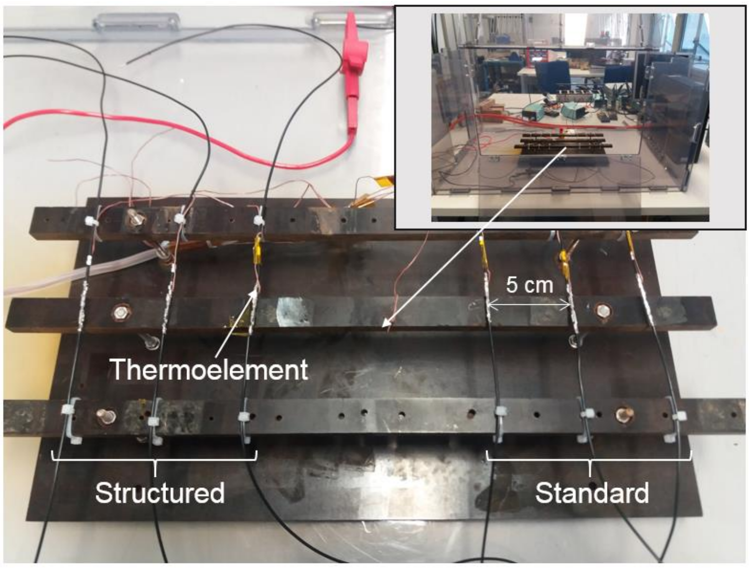

Figure 15. Measurement setup for Derating test.

In addition to these mesurements, thermographic pictures were taken using a JENOPTIK VarioCAM HD to locate the heat point in the connection.

5.4.4 Long-term behavior

Finally, the long-term behavior of standard and structured connectors were compared. The connected samples were placed in a heating chamber at 120°C for 1000 hours and then, after leaving the samples at room temperature for 42 hours, the insertion force was measured. In addition, the connection resistance of the samples was measured before and after the aging test (high-temperature storage).

6. Results and discussion

In this chapter, the results of all the characterizations of textured pins as well as a discussion of them and a comparison with the standard electrical connectors are presented. The first two sections (6.1 and 6.2) include the texturing process design of the pins, where the aim was to find the necessary parameters to obtain porosity within the topographic maxima. The presence of intermetallic compounds in the coating layer and its influence on the texturing is also discussed. Section 6.3 presents the results of the mating and unmating measurements of standard and textured pins. Additionally, due to the high values of insertion force obtained, the possibility of brushing the surface of the textured pins before the force measurement is evaluated. Finally, in section 6.4, the tribological and electrical properties are commented and compared to the properties of standard electrical connectors.

6.1 Selection of texturing parameters

As explained above in the introduction, the presence of porosity is determined by the period of the texture. The optimal period for obtaining porosity within the topography maxima is around 15 µm. Furthermore, the presence of porosity is influenced by the laser fluence. Accordingly, a strip of the same basis material and coating of the pins was irradiated with interfering laser-beams using different laser powers and then the resulting textures were compared. Table 3 summarizes the values of laser power that were used in order to find the optimal laser intensity to ensure remaining porosity. A large range of laser power was, in principle, tested but only a few values, the most representatives, were chosen for discussion. The sample was textured in different spots with intensities between 4.5 W and 6 W with increments of 0.1 W (20 mJ/cm^2). This table also gives values of laser fluence (F) calculated according to equation 3. In this work, no lens was used and therefore, the magnification factor was considered as 1. The diameter of the laser beam was approximately 8 mm, resulting in an area of 0.5 cm^2.

Table 3. Laser powers and corresponding fluences used to select the definitive parameters of the structuring.

Laser Power (W)	Fluence (mJ/cm^2)
4.50	895.25
5.10	1014.61
5.54	1102,15
6.04	1201.62

These relatively high values of laser fluence were used due to the high reflectivity of the tin layer at the used laser wavelength.

It is important to remark the strong influence of the inhomogeneous laser beam profile on the energy input. As shown in figure 16, the variation of the intensity within the laser spot results in inhomogeneity of the texture, whereon different regions have different levels of texturing.

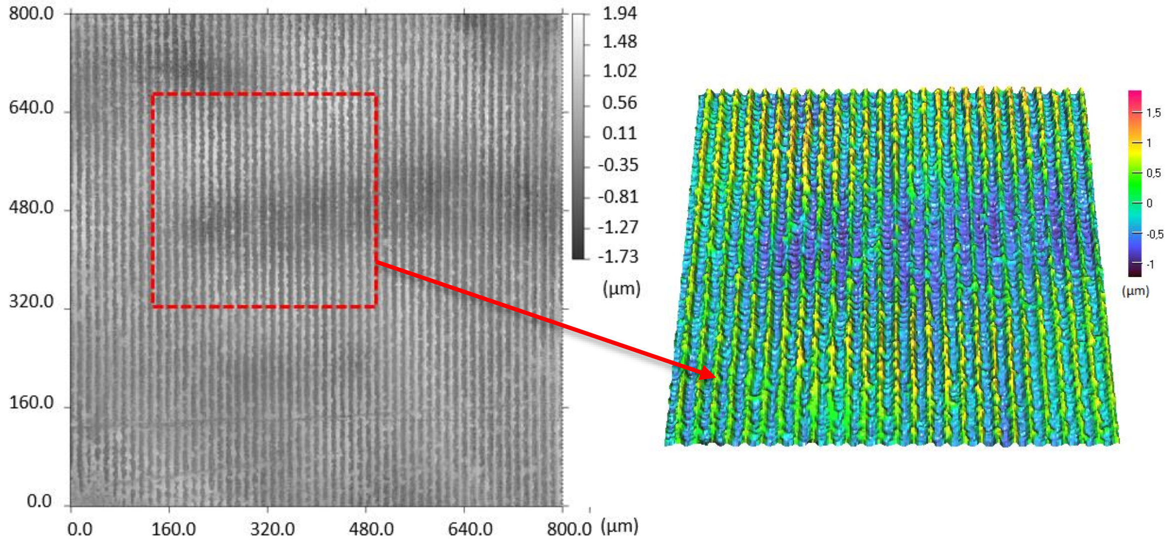

Figure 16. Nanofocus images of a spot textured with a laser power of 5.30 W: 2D topography view (left) and 3D reconstruction (right).

Therefore, only the central area of the textured spots has been imaged for comparison of the laser power aiming to reduce the influence of the laser beam inhomogeneity on the analysis. The surface colour maps and surface depth profiles recorded for each laser power value are presented in figure 17. Herein surface depth, or height, is understood as the vertical distance between peaks and valleys of the structure.

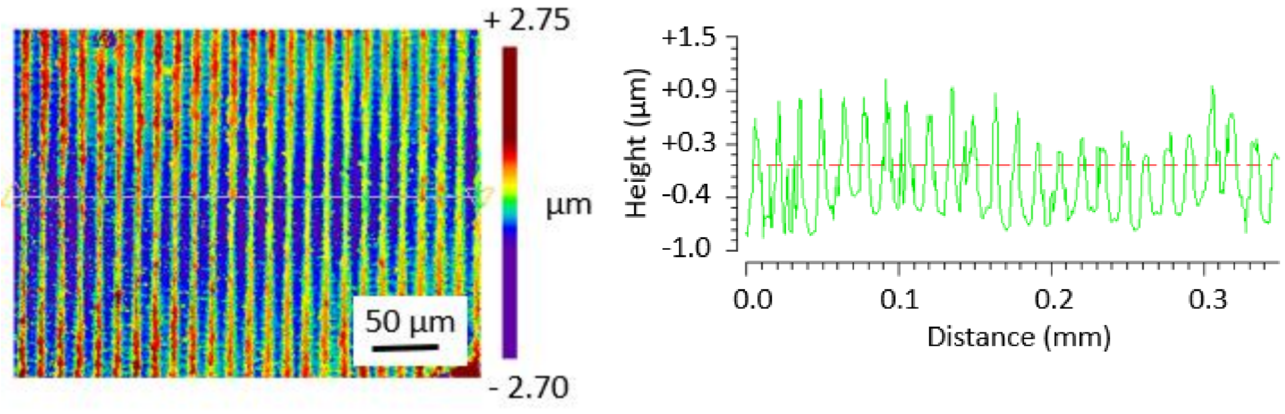

(a)

(e)

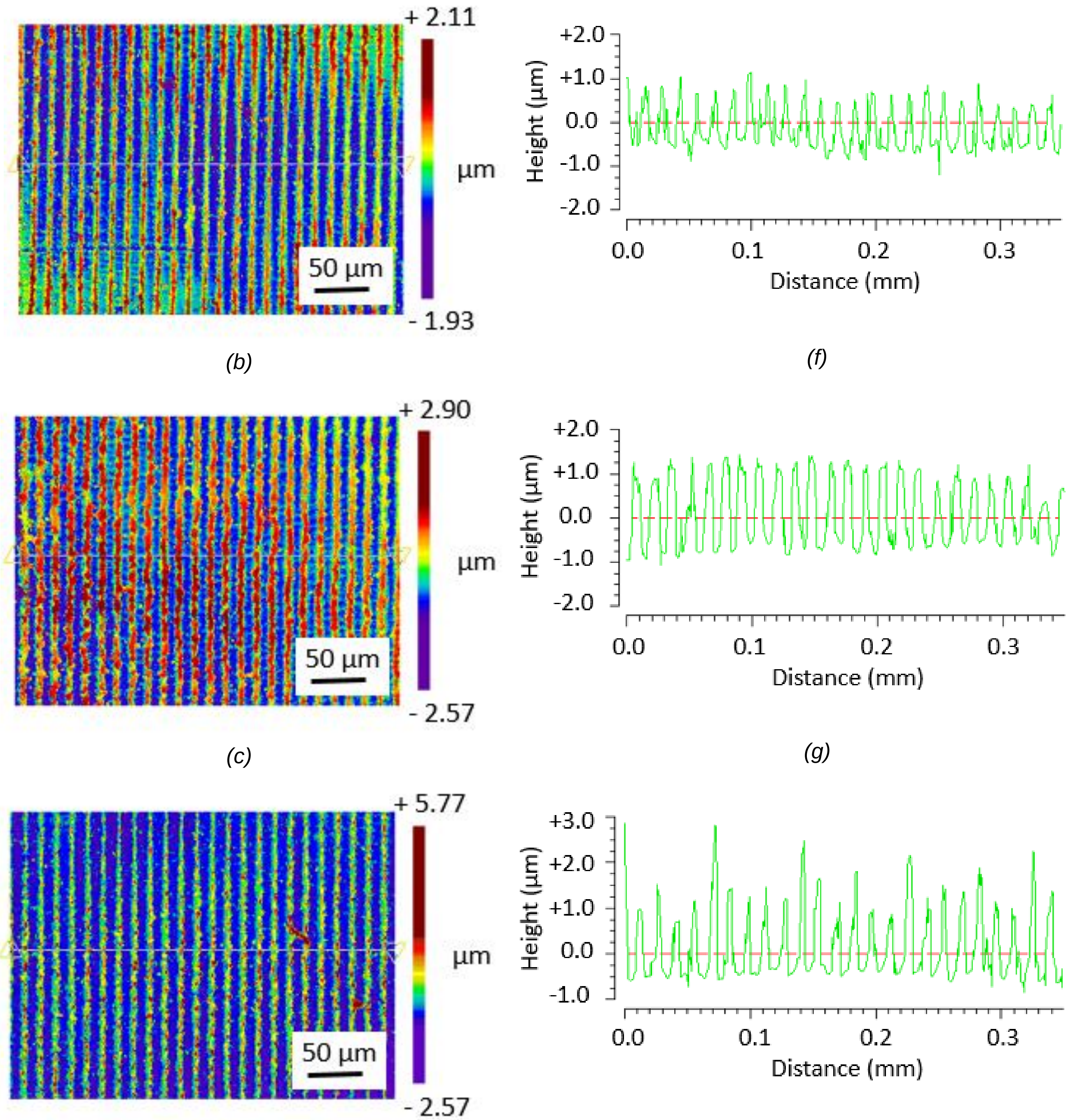

(b) (f)

(c) (g)

(d) (h)

Figure 17. Sample surface characterization by means of a white-light interferometer. Topography color map and lateral profile of a sample textured with a laser power of: (a, e) 4,50 W; (b, f) 5,10 W; (c, g) 5,54 W and (d, h) 6,04 W.

In general, three regimes of the surface depth can be distinguished depending on the laser fluence. After reaching a threshold value in the laser fluence the texture depth strongly increases leaving the first regime, which is characterized by a rough/flat topography. In the second regime, a double-peak texture is observed at medium laser fluences. At relatively high laser fluences, a peak-valley texture is obtained. By further increasing to higher laser fluences begins the third regime of ablation.

The textured samples display surface topographies with a pronounced sinusoidal shape proper of the second regime. Fluences lower than 1000 mJ/cm^2 show a strong variation of the surface depth along the symmetrical axis as can be seen in figure 17 (e) for an energy density of 895 mJ/cm^2. Areas irradiated with low laser intensities present topographies poorly defined and a large area of the pattern has double-peaks. The maximum height of the texture is 0.9 µm and it has an aspect ratio of 6.3%. The aspect ratio is defined as the quotient between height and width of the peaks of the texture. The texture improves for fluences higher than 1000 mJ/cm^2. Despite the inhomogeneity in the surface depth profile, the peaks increase in height and fewer double-peaks are found. As figure 17 (f) indicates the maximum height for a laser fluence of 1015 mJ/cm^2 is 1 µm and the structure has an aspect ratio of 7%. Spots structured with laser fluences between 1050 and 1150 mJ/cm^2 display the most homogeneous topography. For a fluence of 1100 mJ/cm^2, the structure shows a surface depth of 1.25 µm on average, with an aspect ratio of 8.7%. If the intensity is even higher, the texture becomes less homogeneous. The volume of molten material at the interference maxima increases and when it encounters with the fluid moving in the opposite direction, coming from the subsequent interference maximum, the collision produces liquid drops that solidify at the structure minima forming metallic particles over the surface. These droplets can be already observed at lower fluences, but for values higher than 1150 mJ/cm^2 the molten fluid splashes more strongly. As shown in figure 17 (g), the maximum height for an energy density of 1200 mJ/cm^2 is 3 µm and the texture has an aspect ratio of 21%.

Finally, after observing the evolution of the texture in the selected range of laser fluences and taking into account the discussion above, a laser power of 5.5 W was chosen as an optimal value to move forward with the experiments. As previously said, a laser fluence of 1100 mJ/cm^2 shows a high homogeneity. The texture still presents small areas with double-peak shape and hence areas around double-peaks may contain porosity within the maxima.

6.2 Assessment of the presence of porosity within the topography maxima

In the previous section, the laser power has been defined using as sample a strip with the same basis material and tin coating than the connector pins produced by *TE Connectivity*. From now on only connector pins will be considered as definitive sample. Figure 18 (a) shows the surface of a copper pin coated with tin by a hot-dip plating process. Scratches, microcracks and deformation zones can be visualized on the surface. These defects might arise during transport or sample cleaning due to the low hardness of the tin layer.

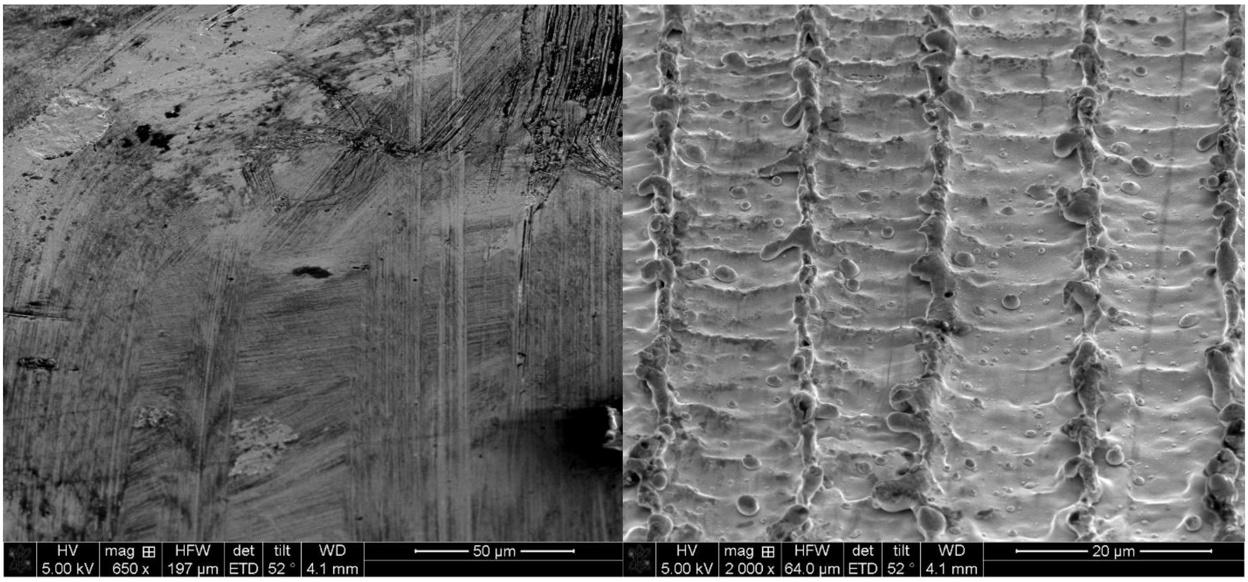

(a) *(b)*

Figure 18. SEM images of hot tin-dipped copper pins (a) Non-textured sample. (b) Textured sample with a laser power of 5.5 W. Viewing angle of 52°.

The roughness of the surface before texturing has a strong influence on the final texture. An input surface with a high roughness of the order of the wavelength of the laser used results in a non-homogeneous texture. It is caused by the multiple reflections on the unevenness of the surface, which produces a visibly inhomogeneous appearance in comparison to a sample with low roughness. The roughness contributes then with the inherent inhomogeneity profile of the laser beam to obtain textures with a lower level of homogeneity. Therefore, a high surface quality is important for achieving well-defined textures.

After being irradiated with two interfering laser beams, the surface presents a line-type pattern as shown in figure 18 (b). Metal particles can be identified in the figure. These particles are product of the collision between the molten fronts coming from the interference maxima. Metal particles are generally observed in metals with a lower surface tension. At high laser fluences, a large volume of metal is melted at interference maxima. Because of low surface tension, the surface is unable to retain the molten material, which is shifted to interference minima, ejecting metal particles that are deposited over topography minima. As a result, the texture shows an inhomogeneous aspect, which is also caused by the input surface roughness and laser beam energy profile as it was previous showed and explained in figure 12.

FIB cross-sections were performed in a textured sample as well as in a non-textured sample in order to identify possible changes in the microstructure during the laser interference patterning.

As it can be seen in figure 19 for a non-textured sample, an intermetallic phase arises in the interface between basis material (Cu) and coating layer (Sn).

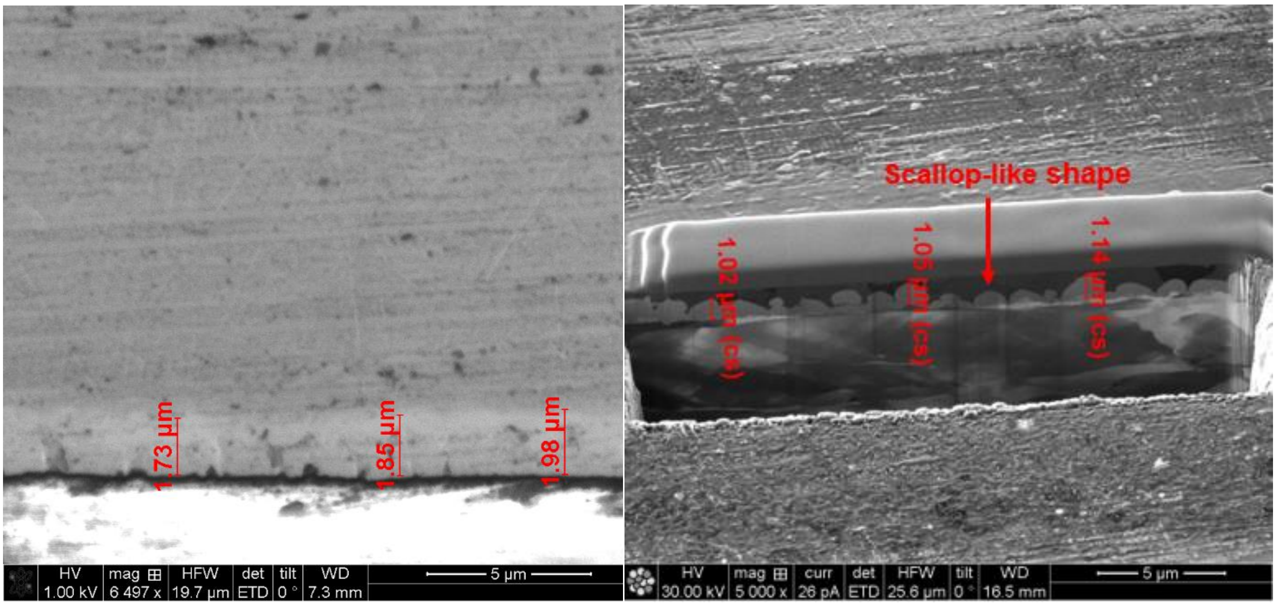

(a) (b)

Figure 19. SEM images of non-textured samples. The pin consists of a base material (copper strip), an intermediate layer of intermetallic phase and an upper layer of tin. (a) Transversal section of a pin. The upper zone is the copper strip and the zone below, which has a lighter grey, is the tin layer. (b) FIB cross-section.

In figure 19 (a), the dark grey zone is the basis material and the lighter grey is the intermetallic compound. The brighter zone does not form part of the sample. It is a polymer used for embedding the sample for easier handling. Since the embedding material is non-conductive, there was an accumulation of negative charges in this zone despite the low voltage of the SEM column used and therefore, it seems brighter than the sample in figure 19 (a). As a result, the quality of the image is rather poor. A way to avoid or reduce this effect could be to coat the polymer with a layer of a conductive material, such as Au or carbon, or not expose the embedding material for long time to the electron beam.

The intermetallic layer can be identified as Cu_6Sn_5 or η. This is because the scallop-like shape that it displays, which is characteristic of η-phase. The phase ε, or Cu_3Sn, cannot be noticed at the interface between basis material and η-phase. The microstructure of the basis material can also be clearly visualized at the bottom of the cross section in figure 19 (b). Due to the manufacturing process, it is reasonable to observe elongated Cu-grains, which tends to be oriented in the direction of rolling.

In average, the tin layer has a thickness of 1.8 µm (figure 19 a), while the intermetallic phase is above 1 µm (figure 19 b). The IMC occupies then around 60% of the coating layer. As commented in the introduction, the IMC growth is a diffusion-controlled process. The thickness of the IMC will depend on both temperature or storage time. For large temperature or large times, the IMC can extend through the entire Sn-layer thickness reaching the pin surface. These phases have a detrimental effect on texturing process, causing further texture inhomogeneity. In addition, the difference on the thickness of the Sn coating layer can produce the texture inhomogeneity. The main reason for this is the difference between the thermal diffusivity and absorption coefficient between copper, tin and the intermetallic compounds.

Figure 20 shows a cross-section of a topography maximum of a sample textured with a laser power of 5.59 W. The texture period was measured by WLI resulting in 14.75 µm. As indicated in figure 20 (a), the height of the peak obtained was 1.84 µm, which is similar to the thickness of the Sn coating layer. An EDX-mapping was also performed for this cross-section in order to identify the elements of the specimen. In figure 20 (b), Cu is shown as purple and Sn as green. As it was expected, the signal of Cu is not only confined to the Cu-strip. This element diffuses through the tin layer and forms the intermetallic compounds. If the purple signal is carefully observed, the scallop-like shape proper of the η-phase can be distinguished.

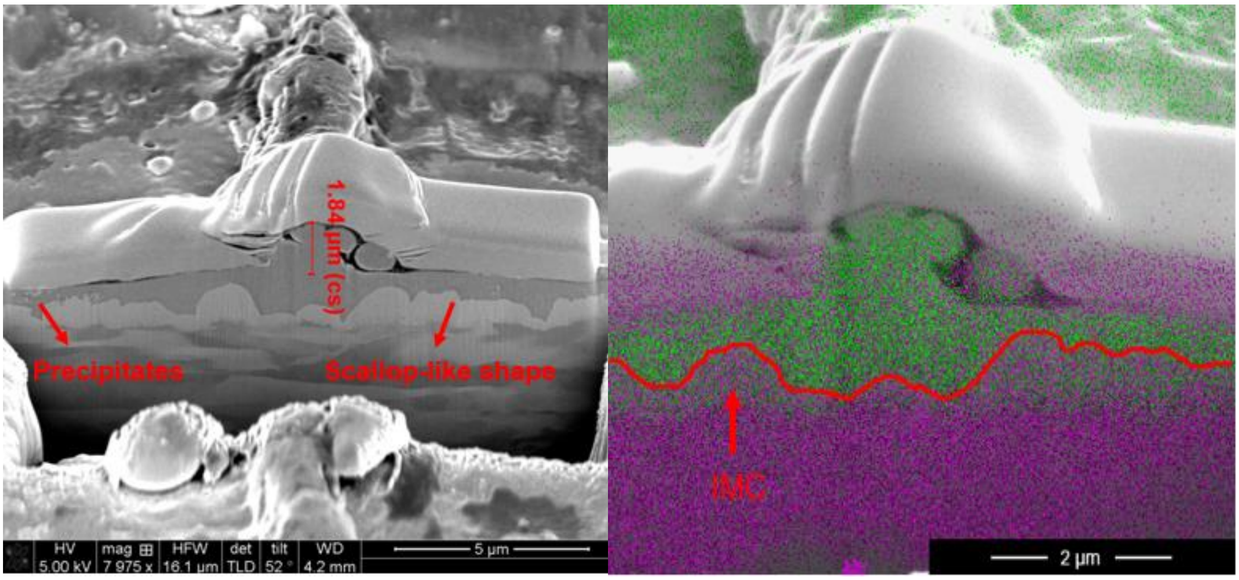

(a) (b)

Figure 20 SEM images of a FIB cross-section of a topography maximum. (a) The same sequence of layers as for the non-structured sample can be observed. The height of the structure is 1.84 µm. (b) EDX colour map. Copper is identified as purple and tin as green.

In figure 20, no difference is observed in the phase morphology of the layers between minimum and maximum of the surface texture. Moreover, by comparing the cross-sections of the non-textured and textured sample it can be concluded that the sequence of the layers does not undergo any change after exposing the surface to the interfering laser beams. There is no further phase transformation during texturing, although the phase transformation is a diffusional process, which occurs spontaneously at room temperature and increases with higher temperatures. Somehow, this can be explained considering some kinetic aspects of the system Cu-Sn. During the process of laser texturing, the material is exposed to high temperature gradients and therefore, the system is far from the thermodynamic equilibrium. However, whether or not the intermetallic phase is formed depends primarily on kinetics. It has been postulated that those phases with the least amount of rearrangement or movement of atoms are kinetically favored. Simple isotropic crystal structures with small unit cells are therefore kinetically preferred. The two room temperature stable intermetallic phases Cu_3Sn (orthorhombic) and Cu_6Sn_5 (hexagonal) are more anisotropic and complex compared to the cubic face-centered copper or tetragonal tin. The formation of the IMC, in particular, the ε-phase, requires long-range atomic motions and hence, is not kinetically favored. Another limiting factor for the formation of the IMC is the narrow compositional range. The η-phase is stable over a range of 1.0 at.% Sn, from 43.5 to 44.5 at.% Sn. The Cu-rich phase, ε, is stable over a range of 1.4 at.% Sn, from 24.5 to 25.9 at.% Sn [5].

These effects described above hinder the formation of inpptermetallic phases in the re-solidification of the molten tin during laser texturing. Hence, a local-periodic generation of intermetallic phases is not achieved in the given layer system.

The presence of IMC in tin-plated copper contacts was further studied by Trinh in his work [5,17] by means of EDX line-scans and DRX characterization. The influence of the DLIP process on the IMC growth was also analyzed and discussed in his work. Trinh showed that DLIP leads to a periodic variation of the tin-layer thickness, which is around 2 µm before texturing. The EDX scan-lines indicated that between the bulk material and the surface layer, there is also an intermetallic layer consisting of copper and tin. This kind of layer consists of an upper Cu_6Sn_5 and a lower Cu_3Sn sublayer. These results were supported by a phase analysis through DRX. Measurements showed that the Cu_6Sn_5 intermetallic phase was already present in the initial state and no new phases were generated by laser texturing. See Appendix I for more details.

In figure 20, small precipitates can also be distinguished within the tin layer. In secondary electron contrast, these present the same grayscale as the intermetallic phase. The precipitates are mostly placed in the middle of the layer. These particles partly lead to a curtain effect during the ion milling, reducing the quality of the image.

Figure 21 shows other cross-section of the texture obtained. In figure 21 a two topography maxima and the minimum formed between them can be observed. As indicated, the period of the texture is 14.45 µm. On the left maximum of the figure is easy to notice what is called a double-peak. This type of texture appears when the laser fluence is not high enough for the fronts of the molten metal to encounter and thus, they solidify forming a double maximum. As pointed out in the previous section, some percentage of double-peaks is required in order to ensure the presence of porosity within the texture maxima. Considering the inherent inhomogeneity of the laser beam, there are zones where the laser fluence is higher than others. Therefore, there are zones that are better textured than others. On this basis, it was preferred to obtain double-peaks in those zones where the laser has the lowest energy. In zones with higher fluences, the fronts of molten material do not encounter completely at the interference minima, resulting in single peaks but with porosity.

The presence of porosity within the maxima for a laser power of 5.59 W is confirmed in figure 21, where a magnified view of the pore in the left maximum can be observed in b. In particular, this pore has a width of 0.82 µm and a height of 0.62 µm. However, larges pores with widths of up to 1 µm and heights of 1.25 µm can be obtained by laser texturing.

In the laser interference minima, the surface does not receive any energy input and therefore, if the surface is covered with a layer of lubricant, it should remain there after texturing. Due to the Marangoni effect, the molten metal shift to the interference minima forming the texture maxima. As the lubricant is not exposed to the laser, the molten fronts encounter and solidify enclosing it. Large pores will then imply a large volume of lubricant and therefore, an improvement in frictional performance.

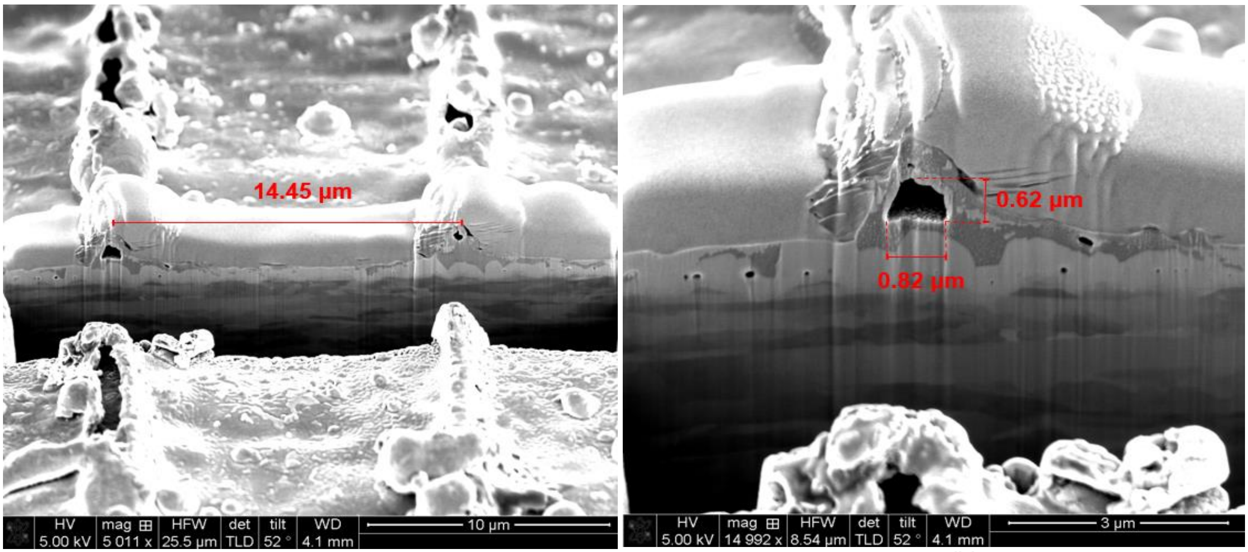

(a) *(b)*

Figure 21. FIB cross-section of a structured sample. (a) Texture with a period of 14.45 µm. A double-peak can be seen on the left bottom of the image. Pores in the maxima and metallic particles on the minimum can also be visualized. (b) Magnified image of the left maximum, which displays a large pore with a width of 0.82 µm and a height of 0.62 µm. Porosity within the minima is also observed.

In addition to the pores in the topography maxima, pores below the surface at the topography minima can be observed in figure 21. These pores are chiefly localized near to the interface between the Cu-strip and the Sn-layer. Hence, they can be identified as Kirkendall voids. These micropores are generally related to the growth of Cu_3Sn. During the phase transformation, there is a change in the volume that can cause the appearance of voids. The Kirkendall voids can also appear due to the condensation of vacancies caused by an unbalanced diffusion of the elements during the formation of Cu_3Sn. Therefore, even though the phase ε is not clearly visualized in the SEM-images, some quantity of this phase might be present due to the existence of Kirkendall voids.

The Kirkendall voids affect the reliability of the electrical connectors. The interface between the Cu-strip and the Sn-layer will be then a critical zone of the connector, susceptible to premature failure since these micropores can derive in cracks due to stress concentration. The Kirkendall voids will also have an effect on the electrical performance, reducing, in general, the electrical conductivity of the connector. They are discontinuities in the electrical current path inducing a resistance to the current flow.

In figure 21 can be seen that the IMC reaches the surface of the pin at the topography minimum. In addition to being detrimental for laser texturing, the IMC growth to the surface implies a lower performance of pins in terms of mechanical and electrical properties. Cu_6Sn_5, the first intermetallic phase to growth, presents a higher resistivity compared to tin (see Table 1). This runs against to the main goal of reducing the contact resistance of the system since the contact resistance shows a direct dependence with the resistivity of the material.

As the resistance in the interface between both parts of the connector is increased, it would be necessary to increase the contact normal force. As previously shown in equation 3.6, there is an inverse relationship between contact resistance and normal force. By increasing the force, the surfaces are brought closer and there is an increment in the number of contacting surface asperities. Consequently, the load bearing area also increases. The oxide layer covering the surface is disrupted and more a-spots for electrical passage are formed. Furthermore, there will exist a permanent flattening (plastic deformation) of the contacting asperities, which reduces the constriction resistance associated with each a-spot and hence the overall resistance contact.

The contact area will then be influenced by some mechanical properties of the material such as hardness and elastic modulus. The yield strength will also impact on the electrical behaviour since it is directly related to the hardness by a factor of approximately three. Both Cu_5Sn_6 and Cu_3Sn present higher hardness and elastic modulus than Sn. Therefore, if the IMC reach the surface, the asperities will not undergo plastic deformation and a good contact will not be established. Accordingly, as commented above, an increase in the normal force will be required in order to compensate a rise in the contact resistance. However, a higher normal force will represent a higher connection force and undesirable stresses on the contact spring/housings. A rise on the insertion force leads to more wear of the surface, which in turn increases corrosion susceptibility by removing the protection provided by the contact finish. This latter degradation mechanism will be partially mitigated by the increase on the surface hardness due to the presence of IMC.

Once verified the existence of porosity in the sample by FIB-cross sections, samples textured with PAO 40 were analyzed by means of Raman Spectroscopy in order to assess the presence of the lubricant within the porosity. Three ways of lubricant application on the pin surface prior texturing process were tested: simply dipping the samples into the lubricant;

dipping and removing the excess of lubricant with a plastic sheet, and third, applying the lubricant using a brush. After texturing, the samples were cleaned in an ultrasonic bath with acetone for 5 minutes and then with 2-Isopropanol for other 5 minutes. The main objective of doing this was to ensure that only the PAO 40 beneath the surface enclosed in the pores of the texture was measured. For the sake of comparison, Raman spectra were also acquired for a non-textured pin and a pin textured without lubricant.

Figure 22 provides the Raman spectra of all the samples for the case of simply dipping the pins into the lubricant prior to texturing. For the other two methods of lubricant application, no Raman signals of PAO 40 were found at the texture maxima. Besides the lower quantity of lubricant that may be left after remove it by means of either the plastic sheet or brush, a large portion of the lubricant may reach its fire point (around 300°C) and may be burned during texturing.

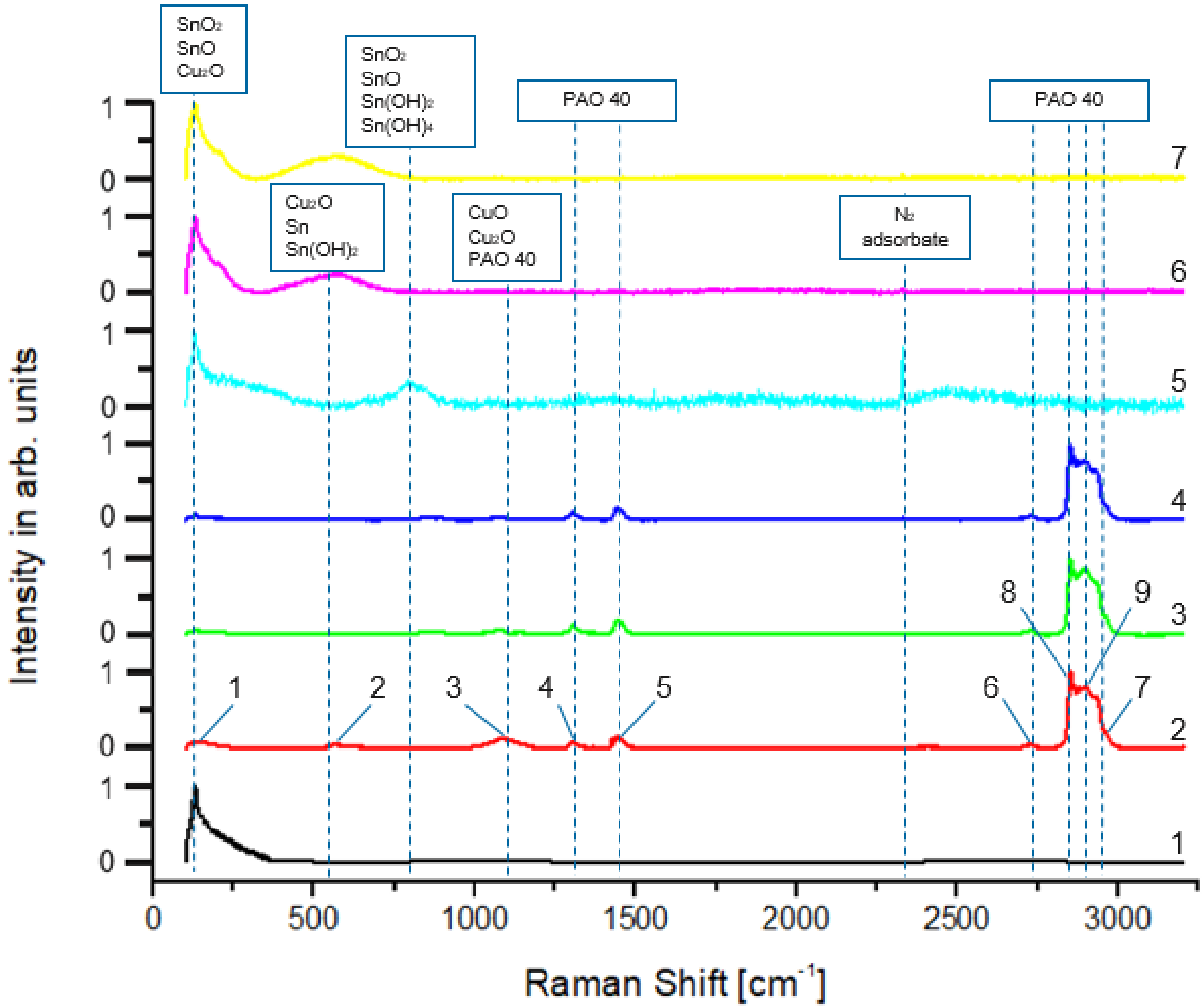

Figure 22. Raman spectra acquired at room temperature for non-textured and textured samples with and without lubricant. Curve 1: non-textured pin. Curve 2: PAO 40. Curve 3: topography maximum; curve 4: topography minimum (1) and curve 5: topography minimum (2) of sample textured with lubricant. Curve 6: topography maximum and curve 7: topography minimum of sample textured without lubricant.

The Raman spectrum of the non-textured sample is represented by curve 1. Curve 2 shows the Raman spectrum of the PAO 40. The spectra taken for the sample textured with lubricant are marked as 3, 4, and 5. Lastly, the Raman spectra of the sample textured without lubricant are indicated as 6 and 7. It should be noted that the Raman spectroscopy was performed in random positions over each sample. In Appendix II, a magnified view of each curve is included for better visualization.

The non-textured sample displays only an absorption peak at 124.74 cm^{-1}, which is ascribed to vibrations of either tin oxides (SnO_2 and SnO), or copper oxide (Cu_2O) on the surface.

The poly-alpha-olefins (commonly abbreviated as PAO) are synthetic, saturated hydrocarbons. The PAO consists of a main carbon chain, or backbone, with flexible alkyl offshoots extending from each carbon. In this work, a PAO SpectraSyn^{TM} 40 by ExxonMobil was used as lubricant. In particular, this PAO stands out because of its uniform, comb-like structure and the absence of short side chains. This type of structure results in rheological advantages, which in turn provides unique benefits as lubricant. Due to its relatively simple structure, it is expected to observe in the Raman spectrum only absorption bands of functional groups such as methyl and methylene bridges. In curve 2, nine absorption peaks can be observed. The positions of the peaks are listed in table 1 of Appendix I. In addition, the chemical bonds that were assigned to each absorption peak and the intensity that they display are also listed.

The Raman spectroscopy of PAO 40 was conducted from a drop of lubricant placed over a glass microscope slide. Therefore, the second peak at approximately 564 cm^{-1} may be attributed to the symmetric stretching vibration of the chemical bond Si-O-Si, which comes from the microscope slide used.

The peak at 1084.52 cm^{-1} is ascribed to the stretching vibrational mode of the chemical bond between the carbons of the macromolecule. Furthermore, this peak can be assigned to the bending or rocking mode of the functional group CH_3. The deformation bending mode of the chemical bond C-H as well as the scissoring/twisting modes of CH_2 display an absorption peak near to 1300 cm^{-1}. The next peak, which is at 1403.04 cm^{-1}, can be attributed either to the bending deformation of C-H, the asymmetric stretching vibration of CH_3 or to the scissoring/twisting deformation of CH_2. The deformation of CH_3 and CH_2 presents also an absorption band near to 2730 cm^{-1}. At 2854.17 cm^{-1} appears a peak, which can be ascribed to the symmetric stretching vibration of CH_2. For $CH_{3,}$ this type of vibration is excited at a Raman shift of 2898.04 cm^{-1}. Lastly, the peak at 2943.63 cm^{-1} can be attributed to the asymmetric stretching vibration of CH_2.

Continuing with the analysis of the Raman spectra, in table 2 of Appendix I are summarized the absorption bands that are found for a sample textured without applying lubricant before texturing. As with the non-textured sample, the majority of the bands are from vibrations belonging to tin oxides. Peaks between 120 -130 cm^{-1} and 190 - 210 cm^{-1} may also be ascribed to the formation of tin and copper oxides on the surface. In addition, the peak at approximately 574 cm^{-1} may be related to the presence of Cu_2O and $Sn(OH)_2$. The peak at 2332.01 cm^{-1} appears due to the adsorption of N_2 at the tin coating surface.

The Raman signals obtained for the sample textured with PAO 40 are listed in table 3 of the Appendix I. For the maximum of the texture, the first two peaks that can be distinguished in curve 3, at 129.42 cm^{-1} and 877.34 cm^{-1}, can be assigned to tin oxide vibrations. In addition to these peaks, which were also observed in curve 1 for the non-textured sample, the Raman spectrum of the topography maximum presents bands that can be attributed to the presence of lubricant. The peaks at 1072.78 cm^{-1} and at 1140.60 cm^{-1} are associated with the main chain vibration of the PAO molecule. As in curve 2, the vibration modes of CH_2 exhibit peaks at 1303.87 cm^{-1}, 1371.69 cm^{-1}, 1445.50 cm^{-1}, 2854.17 cm^{-1}, and 2962.32 cm^{-1}. The CH_3 group reveals a Raman band at 2891.05 cm^{-1}, and together with the CH_2 show an absorption peak at 2728.54 cm^{-1}.

Curve 4 represents a Raman spectrum captured at a random position of a texture minimum. As it can be noticed, the curve follows the same absorption pattern than curves 2 and 3 obtained for the PAO 40 and the texture maximum respectively. Other four runs were carried out at different texture minima. The most representative spectrum was selected and is presented in figure 22 as curve 5. In contrast with curve 4, these spectra mentioned resemble the spectrum of the sample textured without lubricant.

Thereby, it can be concluded that the laser texturing provides a successful way to enclosure lubricant beneath the surface. Besides the lubricant enclosed at the porosity of the texture maxima, there was found PAO at the minima of the texture. During texturing, due to the high driving force generated by the extreme temperature difference between interference maxima and minima, the molten material may flow towards the interference minima in a turbulent way. The high flow velocity could cause the formation of bubbles that remain as porosity when the metal solidifies. Furthermore, when two molten fronts encounter at the interference minima, a portion of fluid could be ejected towards the interference maxima, covering the surface and solidifying leaving porosity.

Based on the Raman spectroscopy results, further chemical characterization of the surface after texturing was conducted in order to assess the presence of oxidation products. For this purpose, an EDX mapping of the surface of a pin textured without lubricant was acquired. At this point, it should be clarified that samples textured with PAO cannot be analyzed by means of SEM, and therefore, by FIB or EDX. Since the sample chamber is at vacuum conditions, the PAO may undergo a phase change. Any gas evaporating from the sample would be hazardous for the imaging tool, as it could contaminate the electron column or the detector, compromising the functionality of the microscope or affecting the image quality.

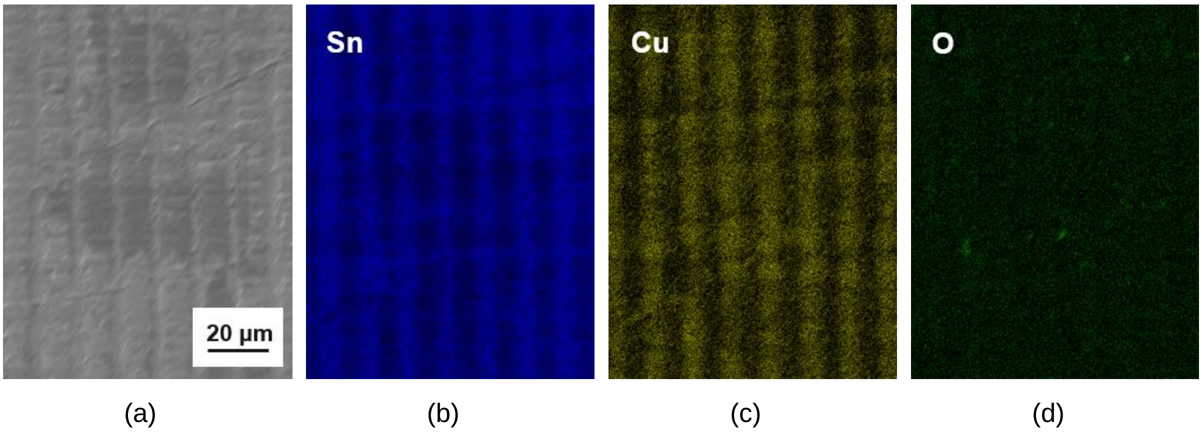

(a) (b) (c) (d)

Figure 23. EDX-Mapping on the surface of a textured sample. (a) SEM-image of the area where the EDX analysis was run. Elements distribution: (b) Tin signal; (c) Copper signal; and (d) Oxygen signal.

Figure 23 (a) shows a SEM capture of the area of the surface where the EDX analysis was performed. Figure 23 (b) shows the Sn-signal. The texture maxima can be clearly identified in the figure because the signal of Sn seems stronger at this position. This can be explained considering the reflection and attenuation of the signal coming from the texture minima before reaching the detector. Figure 23 (c) presents the distribution of Cu. This signal cannot be attributed to the presence of IMC in that the EDX has a depth penetration of up to 2 µm and thereby, the copper substrate under the Sn-coating layer can be measured over all the surface. The signal of oxygen is exhibited in figure 23 (d). As mentioned previously in the introduction, tin is resistant to corrosion since it is passivated by a protective oxide film that is formed on the surface. In spite of the formation of this isolated oxide layer, the contact resistance is not affected due to a disruption of this thin and brittle layer during the connection. Unlike the other elements, no difference between interference maxima and minima can be distinguished for the oxygen. Although it cannot be observed in the EDX-mapping of figure 23, the oxide thickness at the texture maxima tends to be higher than at the texture minima. In his doctoral thesis Trinh has demonstrated that an increase in the oxide layer thickness is promoted by the temperature rise during laser texturing [5]. At the topography minima, the layer was three times thicker than before texturing, while at the topography maxima the thickness increased by a factor of about 4.5. Thermal simulations show that a temperature gradient in the order of magnitude of 100 K can be present between interference minima and maxima as a result of the DLIP process. A higher temperature difference can be generated depending on the laser fluence and the wavelength. Due to the lower tin layer thickness in the topography minima, the heat can diffuse faster into the copper. In the topography maximum, however, the diffusion path is longer and therefore, there is more time available for the oxide layer growth.

Concluding this section, it may be highlighted that by means of Raman spectroscopy it was demonstrated that it is feasible to enclosure lubricant within the topography maxima. To achieved this, the pins were textured with a laser power of 5.54 W. Both texture maxima and minima may present porosity that can retain lubricant. Unlike the minima, which are formed in an uncontrollable way, the enclosing of lubricant within the maxima can be controlled by optimizing the parameters of laser texturing such as laser power and interference period. It was found that the best option for applying the PAO 40 on the surface is to dip the pin into a recipient with lubricant and, without removing the fluid, place it at the sample x-y stage for texturing.

It should be pointed out that at this stage only the possibility to enclosure PAO in the texture was analyzed. The quantity of the lubricant and the efficiency of the method will be assessed in the following section, where the results of the mating force measurements will be presented.

6.3 Insertion Force

In this section, the reduction on the insertion force by enclosing PAO 40 within the texture was verified by reproducing the mating-unmating process. First, the insertion forces measured for textured pins are compared with the values obtained for non-textured pins. Two different specimens were tested. As for the Raman spectroscopy, some pins were cleaned in an ultrasonic isopropanol bath before being tested in order to check that, in effect, the improvement on the insertion force was due to the PAO 40 underneath the surface, inside the porosity of the texture. As-textured pins without cleaning were also tested. In addition, the measurement results of these specimens were compared to each other. On the basis of these, possible areas of improvement on the texturing process were evaluated. The option of applying a further step of brushing the pins surface after the texturing was analyzed. The main aim of this is to give a final conditioning to the surface that could represent an additional reduction on the insertion force.

Since the mask used to select the most homogeneous zone of the laser spot had an area of 1.5 x 1.5 mm^2, the entire length of the pin was texturing by repeating the exposure of the surface to the interfering laser beams throughout the longitudinal direction. To avoid zones without texture, the laser spots were overlapped in approximately 0.05 mm. In figure 24, the overlap of the different textured areas is distinguished. Moreover, in this figure is possible to identify the wear tracks generated during the mating and unmating process. In particular, these wear tracks were obtained after 10 connection cycles. As described in the materials chapter, the receptacle part of the connector present two independent contact springs on opposite sides. Each of these lamellar springs produces two contact points over the pin surface, which are visualized in figure 24. These contact points are positioned one behind the other in order to stabilize the position of the connector pin relative to the receptacle.

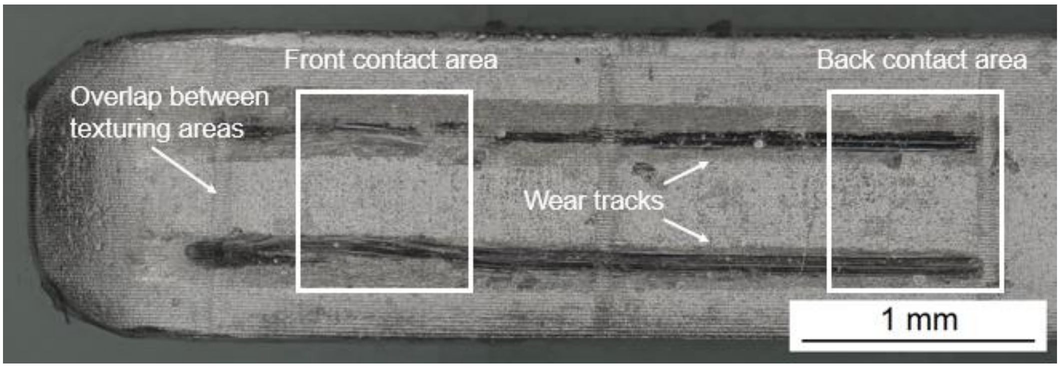

Figure 24. Textured pin after 10 mating-unmating cycles. In addition, in this picture, the overlap between the laser texturing subsequent spots can be distinguished.

Figures 25 to 28 show the force-distance curves obtained for different pins, textured as well as non-textured pins, by testing the connection process. The evolution of the force with the insertion distance is characterized by the presence of two stages, a spreading stage and a sliding stage, which, in general, can be distinguished in the curves. During mating, the pin in the male half of the connector will make contact with the spring beams inside the female half of the connector. As the pin is inserted into the receptacle, it will slide across and will start to deflect the springs. This deflection will cause the normal force necessary for establishing a good electrical contact. The force will rise as the pin moves along the axis of the receptacle and as the stress of the spring elements increases. Theoretically, the force-distance curve will show a prominent peak. The maximum insertion force will depend on the contact normal force affected by the coefficient of friction and the contact geometry. In general, the number of contact points may also influence the maximum value obtained, however, in this case, only a single pin is measured. Once the spring beams are fully deflected, they will touch the flat side of the pin and they will no longer be under stress. The curve then tends to a constant value. The value at which the force is stabilized will depend on the friction force. This latter will act in the insertion direction and will also depend on the normal force and the coefficient of friction. By removing the pin, switches the force direction. The maximum withdrawal force will be equal to the friction force.

Figure 25 shows the force-distance curves of 10 mating-unmating cycles obtained for a non-textured pin degreased in an ultrasonic isopropanol bath for 5 minutes. It should be clarified that the number of cycles was restricted to 10 because copper alloy contacts plated with a cheap non-noble metal like tin may only last as few as 10 to 50 cycles. Hence, most of the connector life is covered by measure the insertion force during 10 mating-unmating cycles.

In contrast to the theoretical description of the force-distance curve commented above, an increase in the force is observed only after the pin moves a distance of about 1 mm. This is because, at the beginning of the test, the tip of the pin is placed at the start of the metal casing of the receptacle. There is a certain distance until the pin reaches the spring beams and the force begins to rise. After an initial force increase due to the spring deflection, the force keeps growing and stabilizes at around 6 N. As the force is higher in the sliding stage, it is not that easy to identify the typical peak of the first stage.

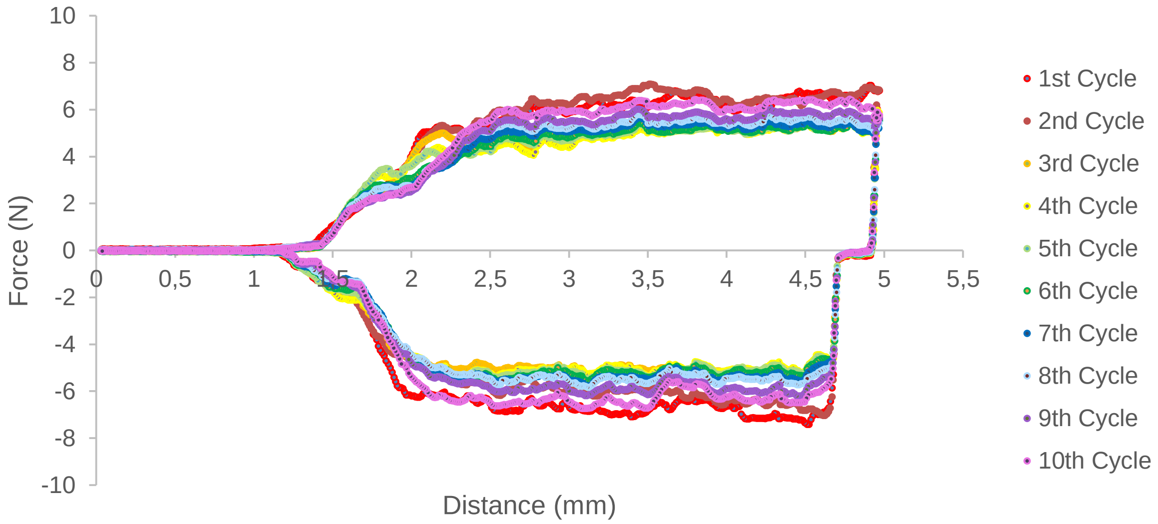

Figure 25. Measured insertion force as function of insertion distance for a non-textured pin cleaned in an ultrasonic isopropanol bath for 5 minutes.

Figure 26 presents the results of 10 mating-unmating cycles obtained for a textured pin. Before the measurement, the pin was also degreased in an ultrasonic isopropanol bath with the pursuit of focusing the results only on the influence of the lubricant enclosed within the texture. The shape of the curves is the same than for the non-textured sample. As can also be seen in figure 25, there is a spread in the force values for the different connection cycles. However, in this case, there is a significant difference between the first cycle and the next ones. The first mating requires a higher insertion force than the others cycles. The force value is stabilized at around 8 N, which is even higher than the one obtained for the first cycle of the non-textured pin. The force decreases for the second cycle but it is still higher than the rest of the cycles. After this cycle, the force remains at around 2 N. This value represents a reduction on the insertion force of more than 50% compared to the non-textured pin.

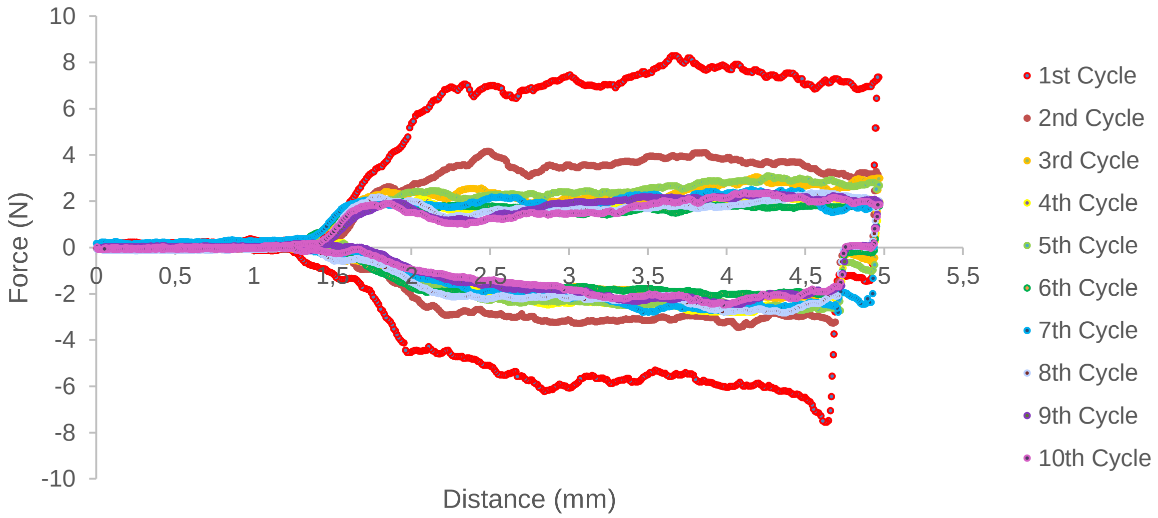

Figure 26. Measured insertion force as function of insertion distance for a textured pin cleaned in an ultrasonic isopropanol bath for 5 minutes.

The change on the maximum insertion force in function of the cycle number is plotted in the following chart for both textured and reference samples. Each point represents the average of the maximum forces obtained for a set of five samples. Due to the reduced number of samples, the dispersion on the results, and therefore, the error bars, are significant. Instead of error bars, in figure 27, the maximum and the minimum forces measured on each set of pins are marked with dashes.

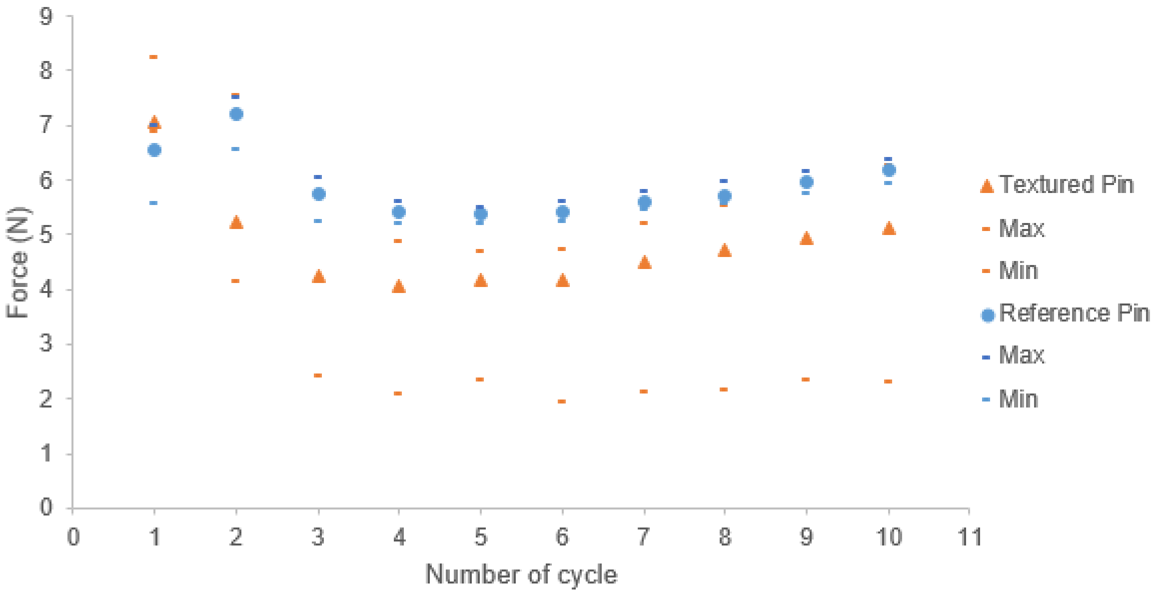

Figure 27. Average of the maximum insertion forces as function of cycle number for textured and non-textured pins cleaned in an ultrasonic isopropanol bath for 5 minutes. The dashes represent the maximal and minimal insertion force measured for each set of samples.

In general, and as can be observed for the reference pins, the force increases during the second cycle. In spite of degreasing the pins with isopropanol prior the measurement, some grease/oil can remain on the surface during the sample handling and placement on the measure machine. This grease acts as lubricant reducing the friction and, therefore, the insertion force. In the second cycle, this grease is no longer available on the surface and the force increases. The asperities of the surface become enough deformed for the surface roughness to decrease. As the roughness is reduced, the coefficient of friction gets lower and so the insertion force. After a certain number of cycles, the force begins to increase again. This can be explained considering that the tin plating wears out throughout the mating-unmating cycles and the basis material is reached at some point.

The minima and the maxima of the reference pins do not differ greatly from the average values. The biggest dispersion is found for the first connection. The main reason may be the difference in the quantity of the grease mentioned above.

The first cycle of the textured samples displays a higher insertion force than the non-textured ones. In the second cycle, there is already a reduction of the 30% on the average insertion force. Unlike the non-textured pins, the second connection presents a force lower than the first connection. From the third cycle, the difference between the insertion force of both set of sample stays around 20%.

Furthermore, both average forces change with the cycle number in a similar way. For the textured pins, the dispersion of the results is higher. The inhomogeneity of the laser energy profile as well as the texture inhomogeneity that is generated may cause this variation. The quantity of lubricant that can be enclosed may also vary due to this inhomogeneity and therefore, its effect on the coefficient of friction.

Although the difference on the average forces is a promising result, the minimum forces shown in figure 27 indicate the capability of the laser texturing to reduce the insertion and withdrawal forces up to in a 60%. This could be obtained by improving the selection of the laser texturing parameters and improving the laser energy profile.

In a real manufacturing process, the implementation of the degreasing with isopropanol is not an option. Therefore, the force measurements were replicated for textured and non-textured pins without cleaning. Figure 28 shows the force-distance curves of 10 mating-unmating cycles obtained for this case. Compared to figure 25, the curves have the same shape, but the insertion force is lower for all the cycles, being around 4.5 N.

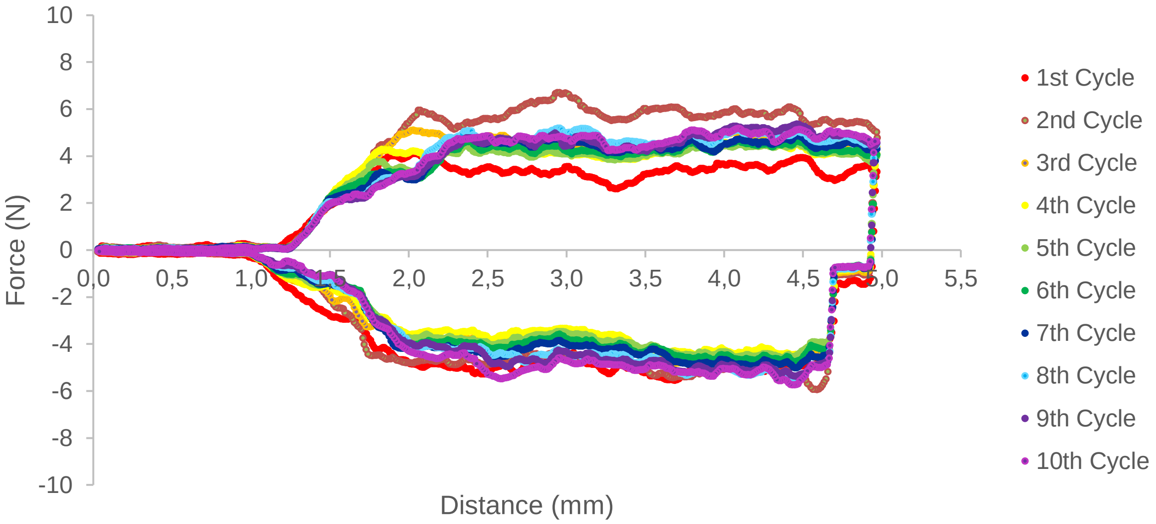

Figure 28. Measured insertion force as function of insertion distance for a non-textured pin without cleaning.

Figure 29 presents the results obtained for a textured pin. As can be clearly seen, the force decreases from one cycle to the other reaching a value below 2 N in the last cycles. The major reduction occurs between the first three cycles. In figure 30, the change on the maximum insertion force as function of the cycle number is plotted for both textured and reference samples without cleaning.

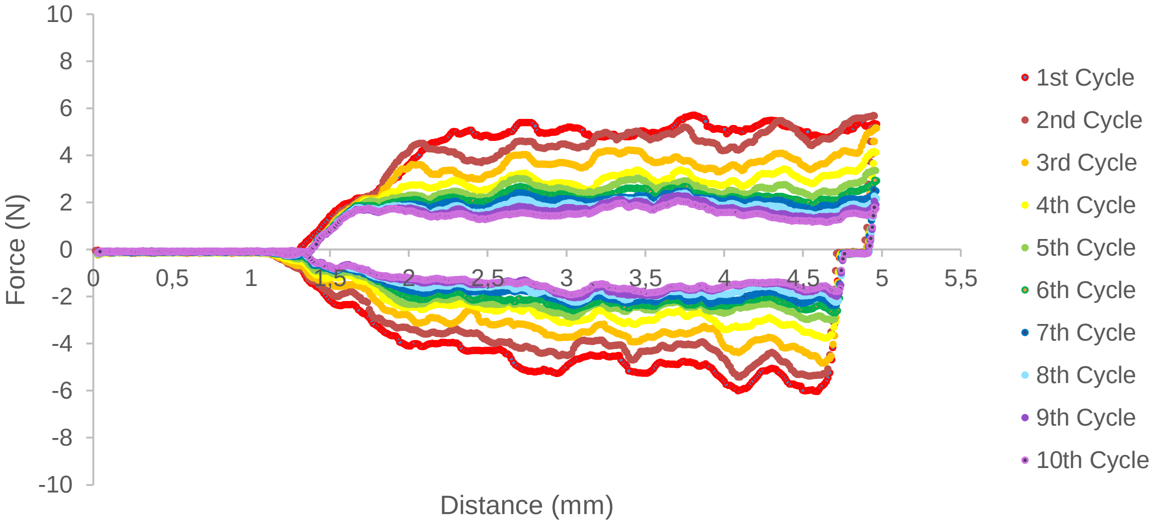

Figure 29. Measured insertion force as function of insertion distance for an as-textured pin.

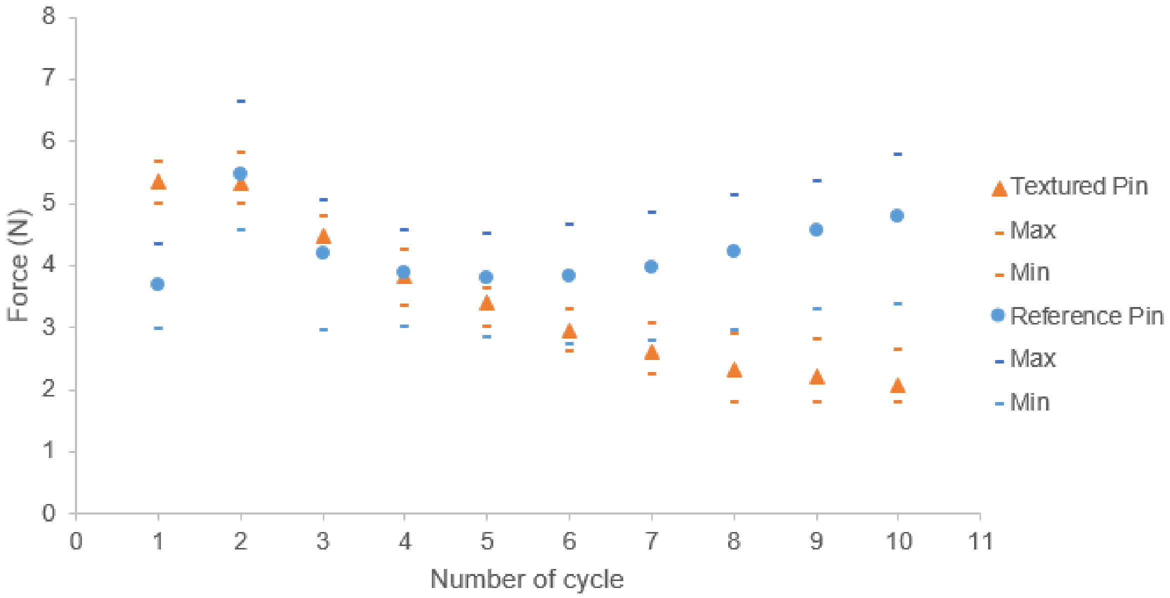

Figure 30. Average of the maximum insertion forces as function of cycle number for textured and non-textured pins without cleaning after the texturing process. The dashes represent the maximal and minimal insertion force measured for each set of samples.

As in figure 27, for the non-textured pins, the force increases in the second connection and then, decreases cycle by cycle, until the sixth cycle where it begins to increase again. The dispersion of the results in this case is higher than for the degreased pins. This can be caused by the lack of cleaning before the measurement. The grease/dirty accumulated on the surface during storage and handling differs from one sample to the other, and therefore, the frictional component of the insertion force varies between them.

In the case of the textured pins, the force decreases continuously by increasing the number of the connections. Only after the fifth cycle, the textured samples display a low insertion forces compared to the average forces obtained for the non-textured set. The spread between the results for each cycle is smaller than in figure 27. This may be explained taking into account that the influence of the inhomogeneity and therefore, the quantity of lubricant retained within the surface, are reduced by the presence of lubricant remaining after the laser texturing of the surface. Furthermore, the lubricant on the surface avoids differences in the coefficient of friction caused by the variation in the surface roughness that may be present for the different textures obtained.

An important advantage that may represent not cleaning the remaining lubricant on the surface after texturing is the protection against corrosion that it implies. Pins textured without lubricant presented oxide over the surface after some weeks, while pins textured with PAO 40 did not show any evidence of oxidation. The formation of this oxide will be not characterized because it is out of scope of this work. The influence of laser texturing on the oxide layer formation was studied by Trinh in [5].

Additionally, the surface of a textured pin was imaged after the first, the fifth and the last mating-unmating cycle in order to complement the force measurement results. Figure 31 shows the evolution of the texture wear by increasing the number of connections. In the fifth cycle, the texture is still well-defined. The topography maxima can be readily distinguished in figure 31 (b). This explains why there is no great difference between the insertion force of the textured and non-textured pins until the fifth connection. After this point, the wear is enough to reach the pores within the texture. Thus, the lubricant enclosed in them will be released and the coefficient of friction will decrease, which in turn reduces the contact normal force and therefore, the insertion force.

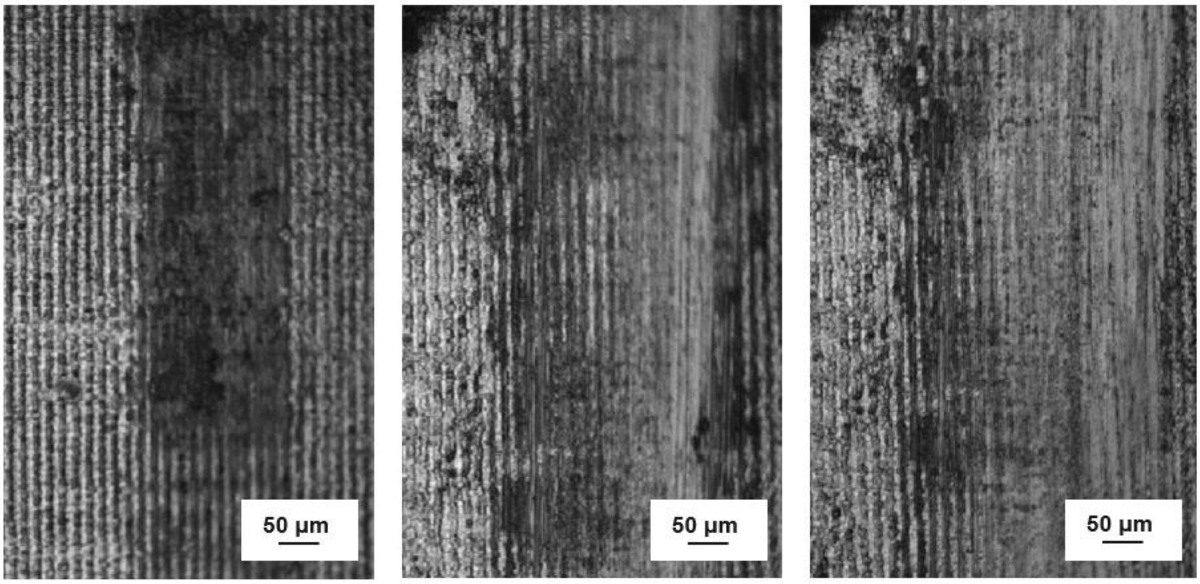

(a) (b) (c)

Figure 31. Nanofocus images of the surface of a textured pin after (a) one mating-unmating cycle, (b) five mating-unmating cycles and (c) ten mating-unmating cycles.

In order to reduce the number of cycles before the release of the lubricant, it was proposed to wear the surface on both sides of the textured pins with a nylon brush. Figure 32 shows the force-distance curves of 10 mating-unmating cycles obtained after brushing a pin.

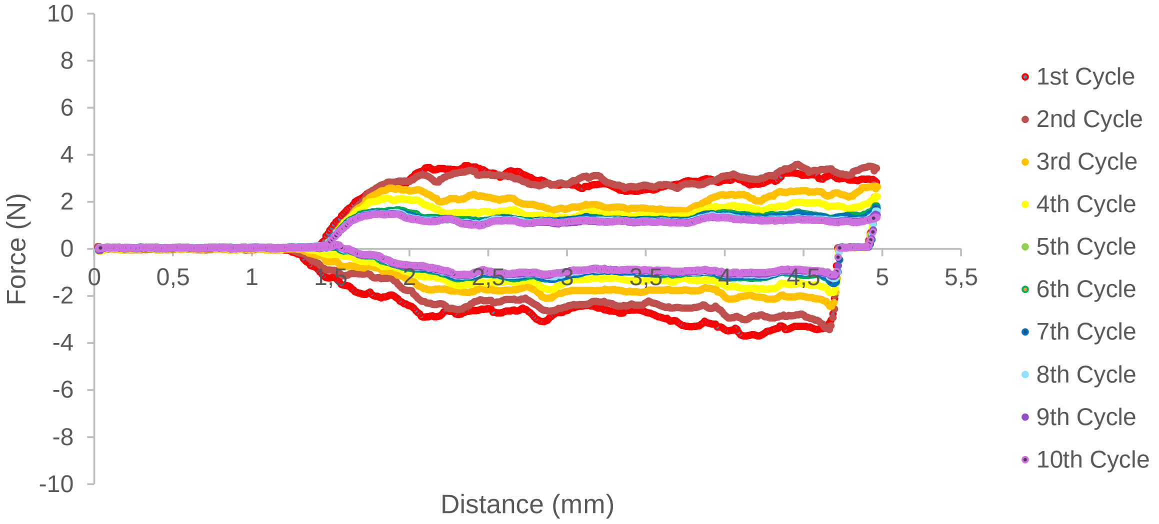

Figure 32. Measured insertion force as function of insertion distance for a textured pin brushed after the texturing process using the nylon brush accessory of a Dremel rotary tool.

Compared to figures 28 and 29, the insertion force for each cycle is clearly reduced. As in figure 29 for the textured pins, the force decreases from one cycle to the other reaching values around 0.5 N lower in the last cycles. Furthermore, a difference in the shape of the curves can be identified after brushing and wearing the texture. If the curves are carefully observed, it can be noticed that they seem more like the theoretical description provided above. The frictional component of the insertion force is lower for the brushed pins, therefore the peak of the first stage of the curve can be recognized from the first cycle. Previously, for all the rest of the measurements, this characteristic peak could be distinguished only in the last cycles. It can be considered that the surface after texturing presents a high degree of roughness. As can be seen in figure 18, the textured surface, besides the typical peaks and valleys of texture, shows metal particles and streaks on the minima that increase the roughness. By brushing, the surface is flattened. As a result of this, the coefficient of friction is expected to be lower.

Figure 33 displays the average of the insertion force as a function of the mating-unmating cycle obtained for a set of five samples textured and later brushed. As the cases shown above, the maximum and the minimum forces measured in each set of samples are also plotted. For the sake of comparison, the results of non-textured pins from figure 30 are included in the graph.

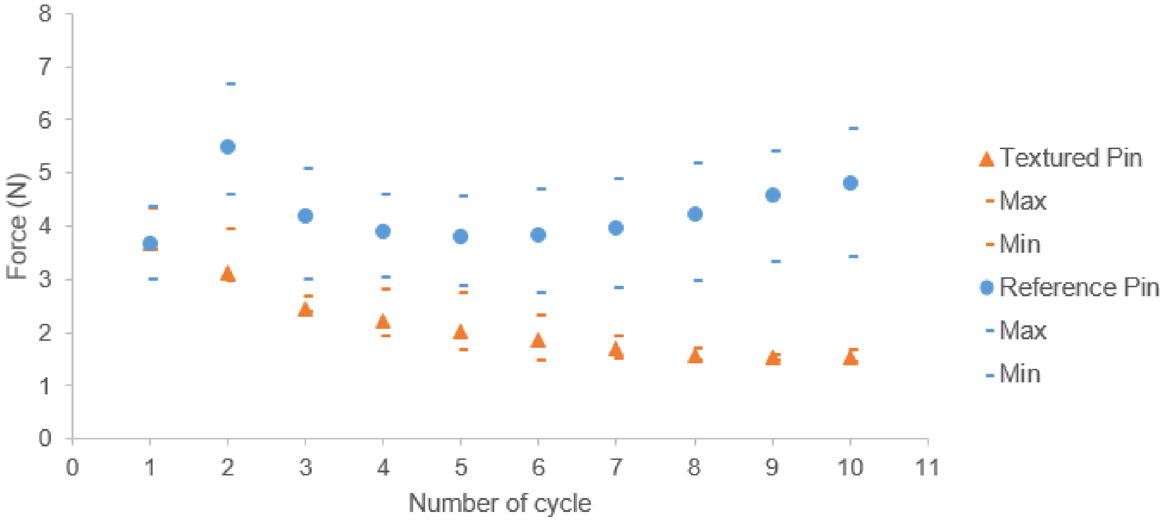

Figure 33. Average of the maximum insertion forces as function of cycle number for textured and non-textured pins without cleaning after the texturing process. Prior the force measurement, the surface at the tip of the textured pins were brushed with a Dremel nylon brush. The dashes represent the maximal and minimal insertion force measured for each set of samples.

By including a stage of brushing after the pin is textured, the insertion force is clearly reduced for all the cycle numbers. An enhancement in the force is already obtained for the first connection. In the previous cases, for the first cycle, the average insertion force of the textured pins was higher than the force of the non-textured pins. However, after brushing both surfaces of the pins, they display a similar insertion force to the reference pins. The difference between the average forces increases with the number of the connection cycle as the force of the textured pins decreases. In the second cycle, a reduction of approximately 50% can be observed. By increasing the cycle number, it can be noted that the force tends towards a minimum value of 1.5 N. In figure 30, this value is reached only in the last cycle, but in figure 33, the force is reduced below 2 N already in the fifth cycle.

Finally, as conclusion of this section, it may be highlighted that is feasible to reduce the force during the connection of the automotive electrical connectors by simply texturing the surface of the male part of the connector. The main idea of the proposed technique is to apply lubricant before the texturing process aiming to enclose it inside the pores formed at the texture maxima. During the connection, the texture will be damaged and the lubricant will be released reducing the coefficient of friction and therefore the frictional component of the insertion force. Initially, an important reduction on the force was obtained only in the last connection cycles being higher than for the non-textured pins for the first connection. From the results it is observed that it takes more than 5 cycles to damage the texture enough for the lubricant to be released. From this cycle, the gap between the insertion forces of the textured and non-textured also begins to increase. On this basis, it was proposed to wear both surfaces of the pin using a brush in order to reduce the number of cycles for the release of the lubricant. Thereby, the insertion force was significantly decreased. Insertion force values below 2 N were achieved from the third cycle. Furthermore, there was a significant improvement already in the first cycle.

Better results may be obtained by controlling the laser inhomogeneity. This would be fundamental in order to generate a texture more homogeneous and to facilitate the selection of the laser parameters. In addition, a larger texturing area would be required to avoid the formation of the overlap of different texturing areas that could also lead to an increase in the insertion force.

6.4 Tribological characterization

This section presents the results of a tribological characterization that was carried out for the pins. The measurement of the coefficient of friction is discussed and correlated with the tendency of the insertion force with the connection cycle. The following figures show the results obtained for textured and non-textured pin by applying a normal force of 1N and a cyclic displacement of 1 mm. All the tribological and electrical characterization presented in his section was carried out using uncleaned pins. Figure 34 provides typical curves of coefficient of friction (COF) as a function of the slide path. Three curves can be distinguished, for the case of the textured pins, pins with and without brushing after texturing were analyzed.

First, it should be commented that in figure 34, as the movement was cyclical, the sign of the COF changes with the direction of the movement. For the non-textured pin, the COF was initially 0.20 and subsequently begins to rise with the slide path, reaching a value of 1.10 and fluctuating around it. In the case of the textured pin (without brushing), the COF starts at 0.27 and increases reaching a maximum value of 1. After sliding a total of 8 mm, the COF decreases with the distance until it reaches a minimum of 0.48. The textured pin brushed after the texturing process displays a lower COF in all the slide path. The COF was initially 0.21 and its value fluctuated around 0.50 during all the test.

As in the previous section, a set of five pins were measured for each case. The COF average of each set were calculated and plotted in figure 35. This figure shows the change of the coefficient of friction with the number of the slide cycle and compared to figure 34, allows to understand better the difference between the samples. Each cycle represents 2 mm of movement, 1 mm back and 1 mm forth.

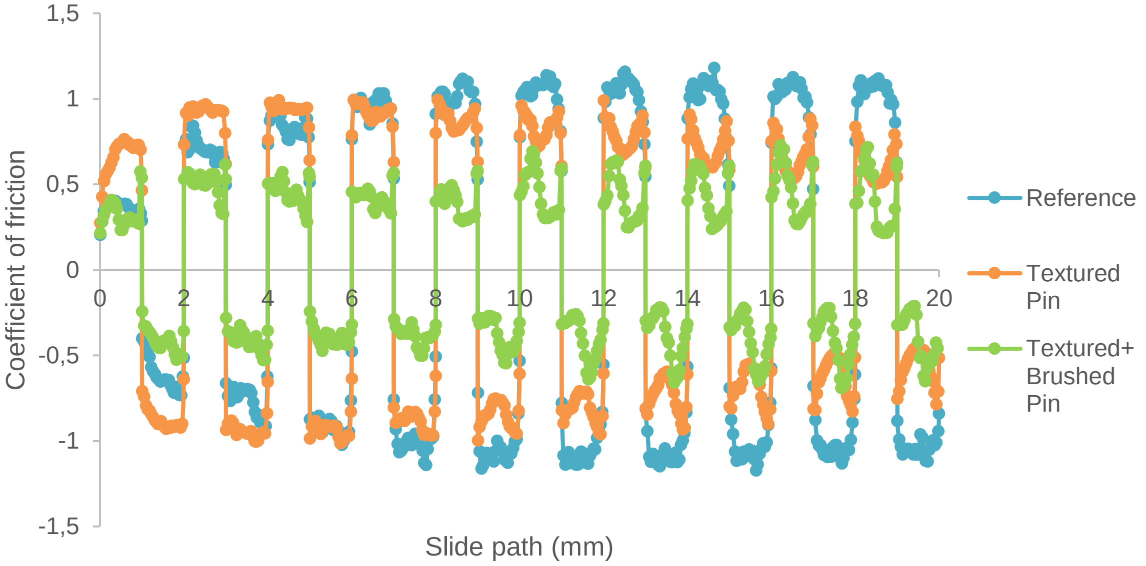

Figure 34. Coefficient of friction as function of the slide path. Measurements for both textured and non-textured pins are plotted. The coefficient of friction was measured by applying a normal force of 1N.

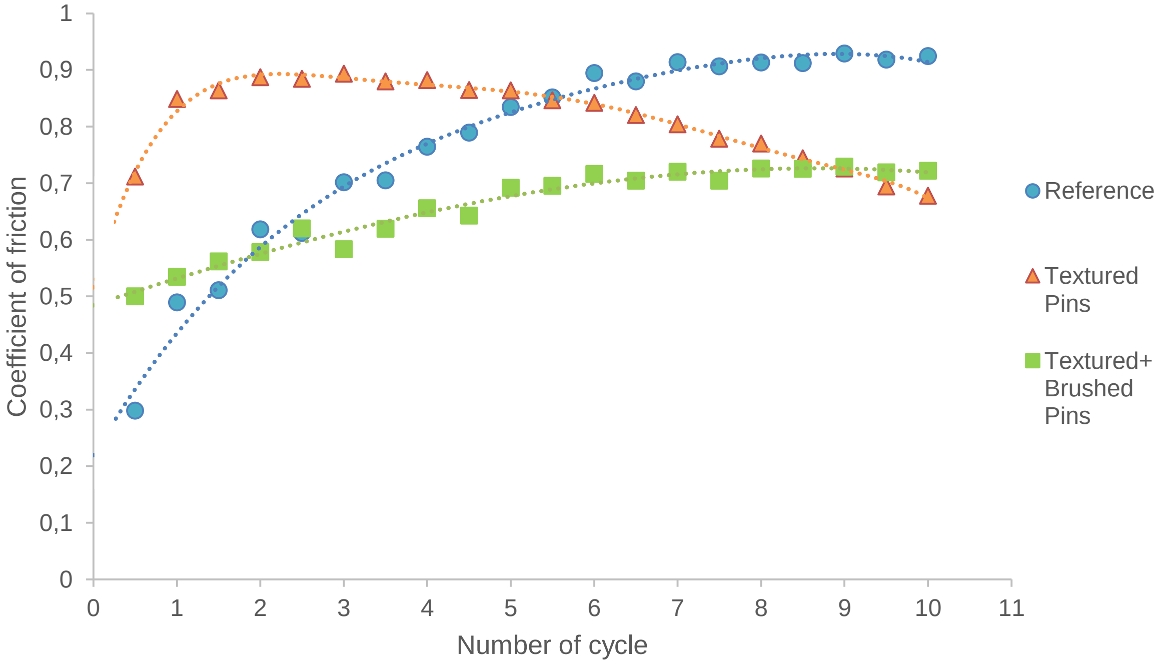

Figure 35. Average of the coefficient of friction as function of the number of the slide cycle for textured and non-textured pins at a normal force of 1N.

For the non-textured pins, the COF increases continually with the number of the sliding cycle from a mean value of 0.3 up to 1. Initially, the textured pins show a COF higher than the reference sample, about the double. It keeps growing until it reaches a maximum value in the second cycle. From this cycle, the COF begins to decrease and only after the fifth cycle it shows a value lower than the non-textured pins. By brushing the surface, the COF is decreased. Already in the first cycle, the COF shows a mean value of 0.5 and it grows continuously with the number of the slide cycle. In this case, after the second cycle, the COF is already lower than the non-textured pins and only after the ninth cycle it reaches the curve of the textured pins without the surface modification. Moreover, the slope of the curve is lower than for the non-textured pins.

As shown in the previous section, the insertion force is strongly influenced by the COF. This latter also depends on several factors such as the type of surface deformation (elastic or plastic); the coating thickness, particularly when the surface deformation is plastic; the surface roughness, and moreover, the material hardness.

The reference pins show initially low COF values due to the grease/dirty accumulated on the surface during the storage and handling of the pins, as explained above for the insertion force. After the fifth cycle, there is a flattening of the curve. Over the sliding cycles, the surface wears out. After some number of cycles, the IMC, or even the basis material, are reached. The hardness of these materials is about seven times greater than the hardness of tin (see table 1), which leads to a lower plastic deformation of the surface. The adhesion between the surfaces decreases and as a result, the coefficient of friction is also reduced. As said, the insertion force is directly related to the COF. The insertion force should also decrease by reducing the COF. However, in figure 30, the insertion force increases after the fifth cycle. As it was already seen in the introduction, the insertion force depends on the normal force, which is directly proportional to the hardness. By increasing the hardness of the surface, a higher normal force is required and hence the insertion force increases.

In figure 35, the COF of the textured pins decreases only after the fifth cycle. As was shown in figure 30 for the insertion force, these values are lower than for the non-textured pins only after this cycle. The COF of the textured pins modified by brushing the surface increases with the number of cycles. However, the slope of the curve is gradually waning. In figure 30, the average insertion force of this set of pins decreases from the first cycle and as the growth rate of the COF is reduced, its slope is also waned. As the non-textured pins, this decrease in the growth rate of the COF is due to the IMC that are reached as the surface is worn out.

Additionally, the contact resistance was measured for each set of pins. This value is plotted in figure 36 as a function of the slide path for the three cases. As expected, the textured pins show the lowest contact resistance with an average value of 0.16 mΩ. The contact resistance for the non-textured pins is, in average, 0.69 mΩ. These samples also show more dispersion in the contact resistance as function of the slide path. By brushing the surface of the textured pins, the contact resistance increases to an average value of 0.57 mΩ, which is similar to the contact resistance of the non-textured pins. Furthermore, the curve has a higher dispersion.

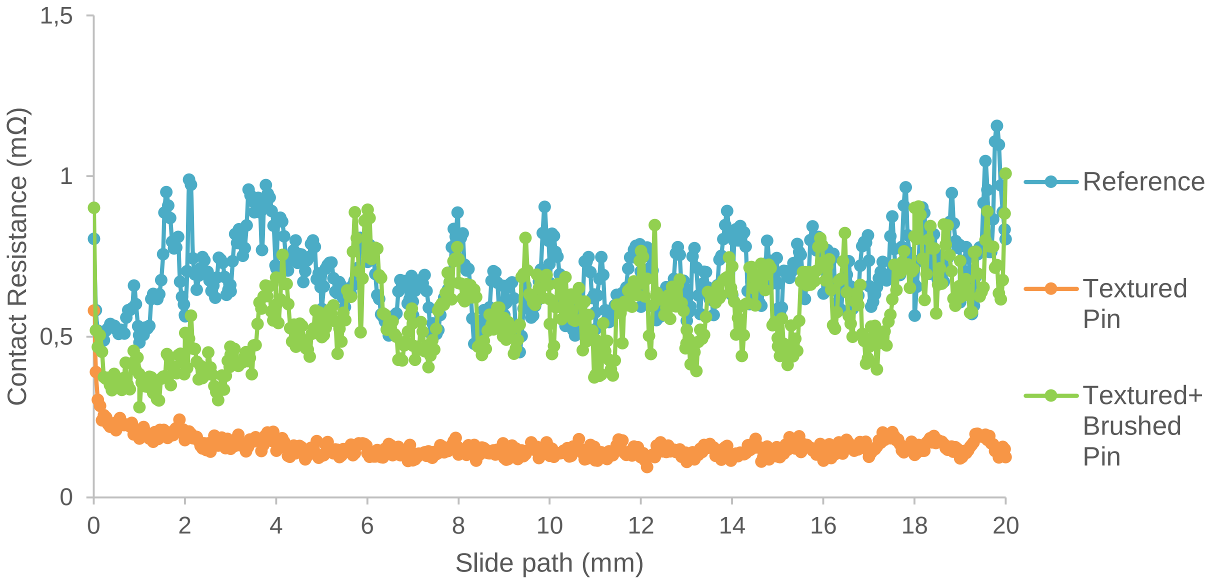

Figure 36. Contact resistance as function of the slide path. Measurements for both textured and non-textured pins are plotted. The contact resistance was measured by applying a normal force of 1N.

In the three cases, the contact resistance decreases abruptly after the first measurement. This is caused by the rupture of the oxide layer covering the surface of the pins. The textured pins modified by brushing the surface show a higher contact resistance than the textured pins since the texture is worn out. The peaks of the surface are flattened and therefore, the surface present a typical hertzian behavior. The resistance of both reference pins and brushed pins tends to increase with the slide path. This can be explained considering the wear of the surface by increasing the number of slide cycle. As commented above, the IMC has a higher hardness and therefore, a higher normal force is required in order to generate more a-spots. In this test, the normal force was constant. Hence, as the hardness increase, the surface is deformed in a minor degree and less a-spots arise. The constriction resistance is directly related to the number of a-spots. As this number decreases, the contact resistance increases.

Concluding this section, it can be highlighted that brushing the surface of the pins after texturing reduces the surface roughness in addition to promote the release of the lubricant without the need of wear the texture through the mating-unmating cycles. This favors a lower coefficient of friction and therefore, lower insertion force. However, the electrical resistance is jeopardized. The brushed textured pins show a higher contact resistance than the normal textured pins, similar to the non-textured pins. The textured pins present a worse frictional performance, but the lowest contact resistance. This latter value is, in average, about 75% less than for the non-textured pins. Although these pins in the first cycles has a higher coefficient of friction than the non-textured pins, this decreases with the number of the cycle. Optimizing the laser system and laser texturing parameter may be a good approach in order to reduce the coefficient of friction and the insertion force without compromising the electrical behavior of the textured pins.

6.3 Electrical characterization

Although the aim of this work is to reduce the insertion force during the connector mating, it is expected that the electrical properties of a connector are affected. The electrical performance of the textured pins is evaluated. First the electrical resistances as function of the normal force is measured. Then, the resistance of the pins against fretting corrosion is examined. In addition, the current derating with temperature is compared between textured and non-textured pins and finally, the long-term behavior of the pins is studied.

In the previous section, the change of the resistance as function of the accumulated friction path for both non-textured and textured pins was presented. As it was shown, while the resistance of the reference contacts oscillates around a value of $R \sim 0.7 m\Omega$, the mean value for the textured pins is $R < 0.2 m\Omega$. This confirms the reduction of the electrical contact resistance by texturing the surface of the samples. This behavior was already shown in [19] and can be attributed to the effect of the optimized surface pressure discussed in [16] for the textured samples, which enhances the current density distribution and results in a larger contact point radius.

Figures 37 and 38 show the resistance as a function of the contact normal force for non-textured pins and textured pins respectively. At a contact normal force of $F_N = 1$ N, the samples were displaced 1 mm in order to break up the tin oxide layer covering the pin surface. This simulates the insertion process, where the surface is worn out through the mating-unmating cycles. After reaching a maximum value of $F_N = 5$ N, the normal force is gradually released.

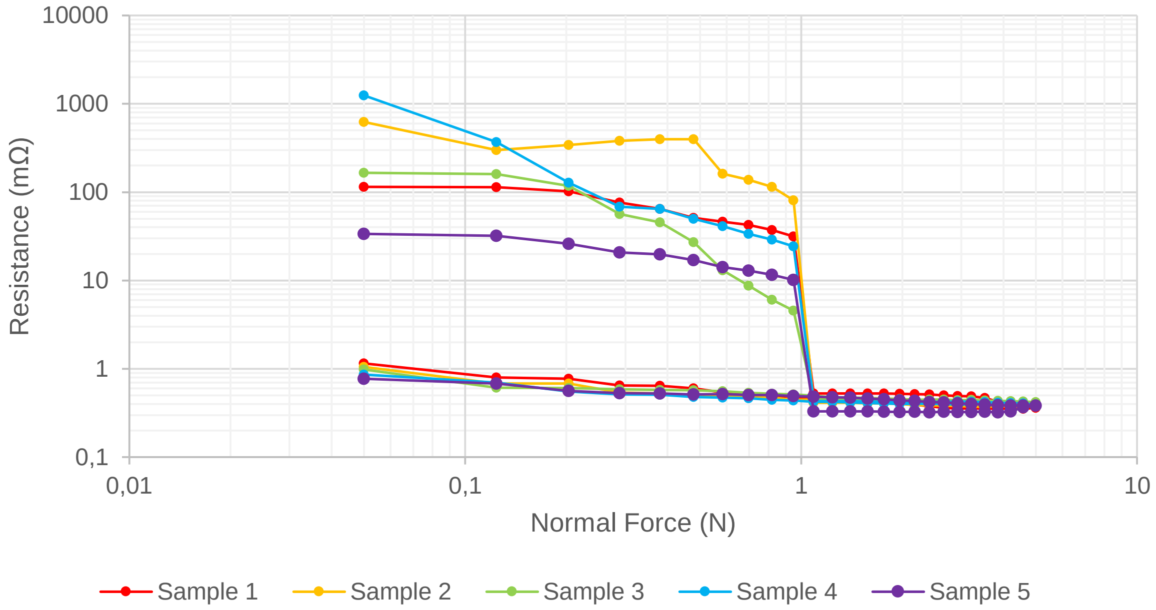

Figure 37. Contact resistance as function of normal force for non-textured pins. The contact resistance was measured applying normal forces ranging from 0.01 N to 10 N. At 1 N, the samples were displaced in order to rupture the oxide layer covering the surface.

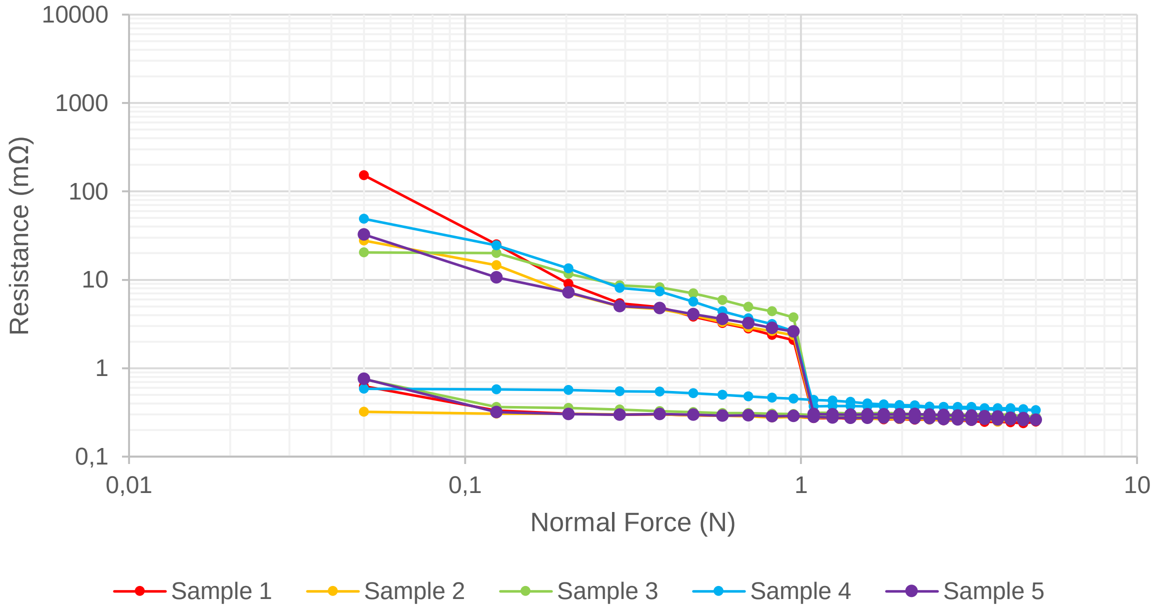

Figure 38. Contact resistance as function of normal force for textured pins. The contact resistance was measured applying normal forces ranging from 0.01 N to 10 N. At 1 N, the samples were displaced in order to rupture the oxide layer covering the surface.

The contact resistance of the textured samples is lower than that of the non-textured sample over the whole load range. For both samples, the resistance drops during loading and increases again during unloading, without reaching the initial resistance value (i.e., hysteresis). During loading, the resistance curves of the textured samples are clearly below those of the reference contacts for values of F_N <1 N. After the relative movement at F_N = 1 N, only a resistance difference of $\Delta R = 0.2$ mΩ can be measured. This latter is of the same order of magnitude than the resistance difference shown in figure 36 between textured and non-textured pins. In figure 36, the resistance was measured during the relative movement of the samples at a $F_N = 1$ N, while in figures 37 and 38 this was measured statically varying the normal force applied. It should also be noted here that the measured contact point resistance does not exactly correspond to the constriction resistance. Instead, there is a specific offset of around 0.1 mΩ due to an intrinsic resistance of the measurement set-up (see [98]).

Subsequently, the electrical resistance of the whole connector was measured as a function of the mating-unmating cycle for both textured and non-textured pins. The results are shown in table 4. As commented before, the female terminal was the same for both types of pins. In order to measure the electrical resistance, cables of 0.7 mm^2 were used.

Table 4. Electrical resistance as function of the mating-unmating cycle for textured and non-textured pins.

Non-textured pins										
Cycle	1	2	3	4	5	6	7	8	9	10
Sample	mΩ	mΩ	mΩ	mΩ	mΩ	mΩ	mΩ	mΩ	mΩ	mΩ
1	0,70	0,70	0,69	0,70	0,70	0,70	0,70	0,75	0,78	0,77
2	0,73	0,73	0,76	0,76	0,76	0,75	0,75	0,77	0,76	0,79
3	0,70	0,71	0,70	0,69	0,70	0,70	0,72	0,71	0,77	0,77
4	0,72	0,72	0,73	0,77	0,77	0,75	0,77	0,76	0,76	0,79
5	0,70	0,73	0,73	0,72	0,76	0,73	0,75	0,75	0,77	0,78
Average	0,71	0,72	0,72	0,73	0,74	0,73	0,74	0,75	0,77	0,78

Textured pins										
Cycle	1	2	3	4	5	6	7	8	9	10
Sample	mΩ	mΩ	mΩ	mΩ	mΩ	mΩ	mΩ	mΩ	mΩ	mΩ
1	0,74	0,72	0,75	0,72	0,75	0,73	0,73	0,72	0,74	0,77
2	0,74	0,73	0,72	0,74	0,73	0,73	0,76	0,74	0,70	0,74
3	0,73	0,70	0,75	0,75	0,74	0,75	0,71	0,76	0,73	0,77
4	0,73	0,72	0,72	0,72	0,73	0,74	0,74	0,73	0,73	0,74
5	0,74	0,72	0,71	0,72	0,74	0,75	0,72	0,74	0,75	0,74
Average	0,74	0,72	0,73	0,73	0,74	0,74	0,73	0,74	0,73	0,75

Considering that the contact resistance of the textured pins is lower than the reference pins, it is expected that the former show also a lower electrical resistance. However, as can be seen in the table above, there is no difference in the electrical resistance of the whole connector between textured and non-textured pins. In chapter 4, it was commented that the MCON contact family used in this work presents a total of 8 contact points. Due to the interaction between the parallel contacts the small difference between the contact resistance of each single contact is no longer detected in the electrical resistance of the whole connector

[98]. Furthermore, the textured pins have lubricant enclosed in the peaks, which is a non-conductive medium.

The most important failure mechanism of the tin-plated electrical contacts is the fretting corrosion. Because of either external forces or local difference in thermal expansion, male and female connector parts can move relative to each other in small displacements called as micro-motions. These micro-motions lead to fretting corrosion. The contact resistance increases by increasing the number of the cyclic micro-motions, since there are oxidation products that are displaced with each motion and are accumulated at the whole contact surface [112].

Figures 39 and 40 show curves of resistance as a function of the number of the micro-motions for non-textured pins and textured pins respectively.

As can be seen, the textured pins result more stable against the fretting corrosion than the non-textured pins. It is considered that the connector failures by fretting when the contact resistance exceeds 1 mΩ. Under this convention, the reference pins failures after an average of 150 cycles. The textured pins show a better behavior against the fretting corrosion. By modifying the surface of the pins using DLIP, the resistance reaches a value of 1 mΩ after 300 cycles in average. The textured pins can resist, then, the double of cycles than the non-textured pins.

The fretting resistance is influenced by four main factors: the static COF, the normal force, the spring rate in direction perpendicular to the normal force and the displacement due to a difference on the thermal expansion. In order to prevent the micro-motions, a high static COF is required. However, once the contact surfaces begin to move relative to each other, a low COF is desirable in order to reduce the fretting wear. Therefore, the presence of lubricant enhances the stability of the textured pins against the fretting corrosion by reducing the dynamic COF. High normal force and low spring rate components contribute also to prevention of the motions. In this work, the same design of the female part of the connector is used for both textured and non-textured pins. The normal force as well as the spring rate are the same for both types of samples. It is important to clarify that a higher normal force would lead to an increase in the insertion force and in the wear of the surface.

The difference on the fretting resistance between the textured and the reference pins can also be attributed to the fact that tin oxides covering the pin surface are more easily broken for the case of the textured pins. This can be explained considering the sinusoidal topography since the oxide layer is better broken due to the high contact pressure generated. In addition, the lubricant embedded in the texture acts as an oxidation inhibitor when is released from the pores. For this specific purpose, further fretting tests with different lubricants / anti-fretting oils may be carried out in a future work.

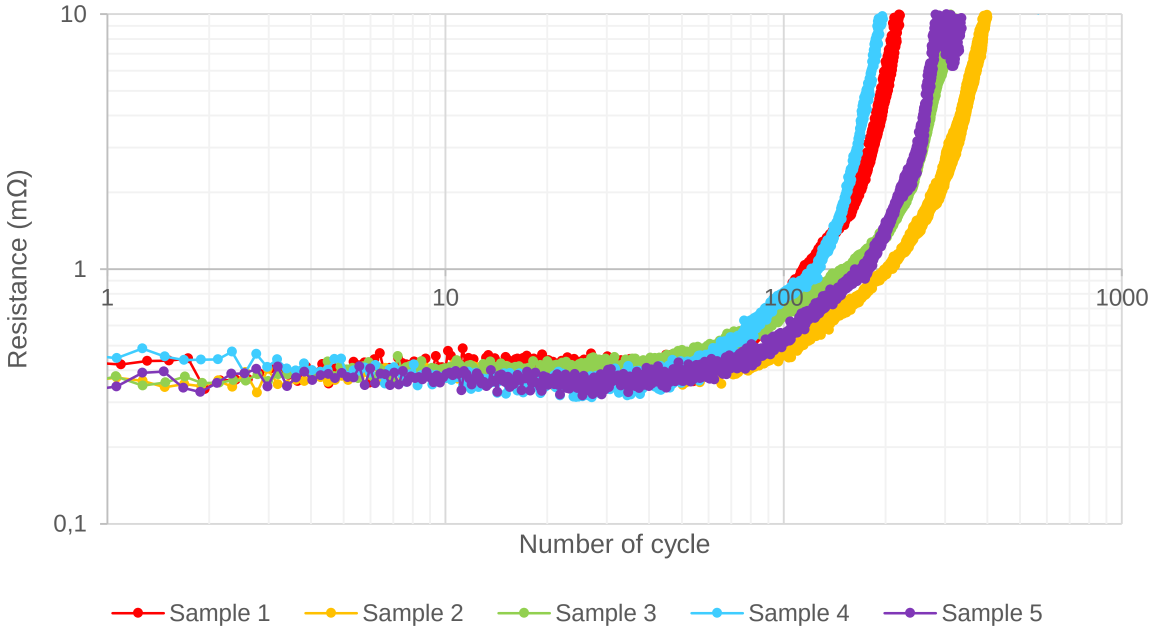

Figure 39. Fretting resistance evaluation. Resistance as function of the number of cycle (micro-motion) for non-textured pins.

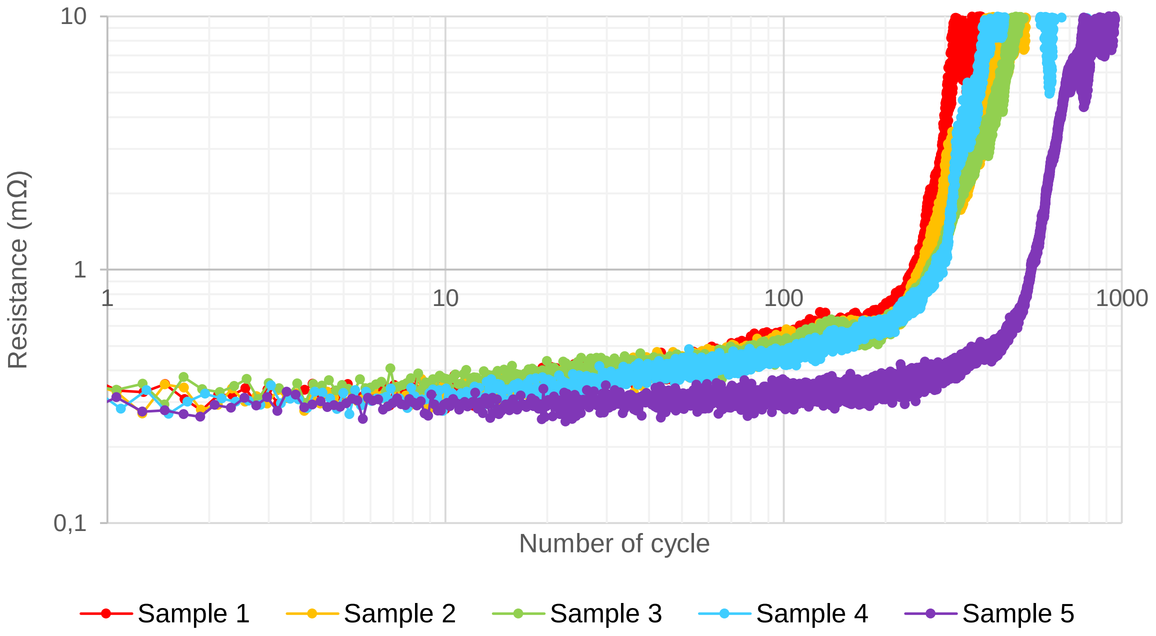

Figure 40. Fretting resistance evaluation. Resistance as function of the number of cycle (micro-motion) for textured pins.

After the previous testing, the temperature rise of the textured and non-textured pins by changing the current applied to the whole electrical connector was compared. As explained in the section 5.4.3, the temperature rise was measured following the standard DIN-EN 60512-5-2. The temperature was obtained at three different current loads: 8 A, 12 A and 16 A. These current loads were randomly selected considering that the 0.7 mm^2 cable used for establishing the electrical circuit allows a maximum current load of 17A. The temperature rise was calculated considering the room temperature as reference. Plots on figure 41 were obtained taking into account that the temperature rise can be modeled as a quadratic function of the current load. A security factor of 0.8 recommended in the standard is already applied in both curves.

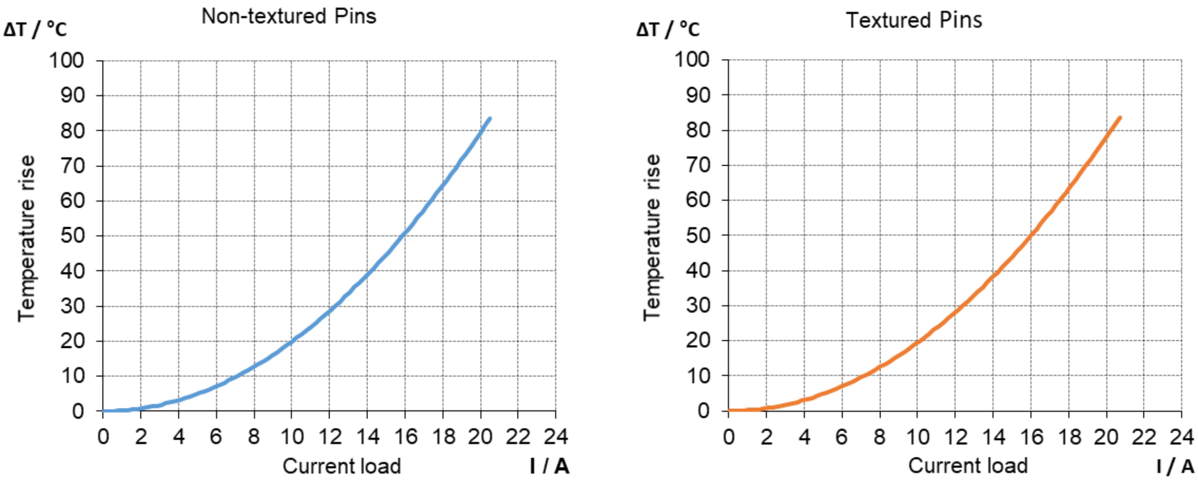

Figure 41. Temperature rise as function of the current applied to the electrical connector. Links: non-textured pins and right: textured pins.

Once the curves above are obtained, the derating curves can be calculated. These latter are shown in figure 42. The derating curve is used to know which current can flow through the electrical connector when the component is subjected to a certain ambient temperature below its maximal temperature. For the MCON 1.2 family, this temperature is 130°C. The upper limit temperature of the connector is determined by the materials used. The sum of the ambient temperature plus the temperature rise caused by the current load due to the well-known joule effect may not exceed the upper limit temperature of the component, otherwise it will be partially or even completely damaged.

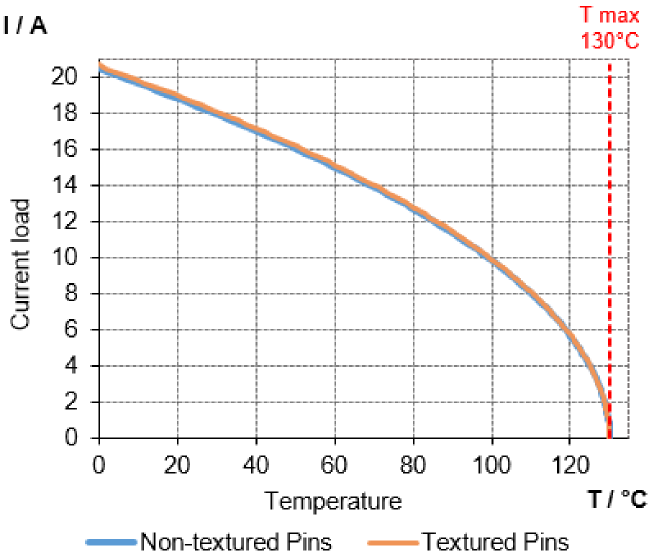

Figure 42. Derating curve for textured and non-textured pins.

Additionally, a thermogram of each connector was recorded in order to visualize the distribution of temperature along the component. The thermography is usually used for inspection of electrical components/installations on-site. This non-destructive method is based on the fact that there is a localized increase in temperature where exists a loss of conductivity. These hot-spots generated are caused normally by the presence of surface oxidation or corrosion, which increases the resistance of the component. The thermography could also be used to record the temperature change as function of the current applied to the circuit in order to obtain the derating curve. However, this method is generally more demanding and complicated than the thermocouple procedure.

In order to ensure the accuracy of the thermography method, the surface of the samples was previously prepared by applying a black paint. This coating is aimed at enhancing and homogenizing the absorptivity and emissivity of the surfaces. A matte coating also reduces the reflection causing a high-quality thermogram. In general, for a correct measurement is necessary to know the exact emissivity factor. This value is dependent on the material, the surface polishing and temperature of the body. Currently, there are some methods that eliminate the influence of the emissivity factor. In this work, a JENOPTIK VarioCAM HD was used as thermography camera. This high definition camera features a built-in laser rangefinder for optimal temperature correction. The VarioCAM also has other correction functions for the emissivity and transmissivity. The emissivity correction can be manual or by using a material table that is already include in the camera system.

Figure 43 shows the thermogram of one of the reference connectors at a current load of 16 A. As said above, this value is almost the maximum current load for the cable used for the test. Figure 44 shows, in turn, the thermogram of a textured connector.

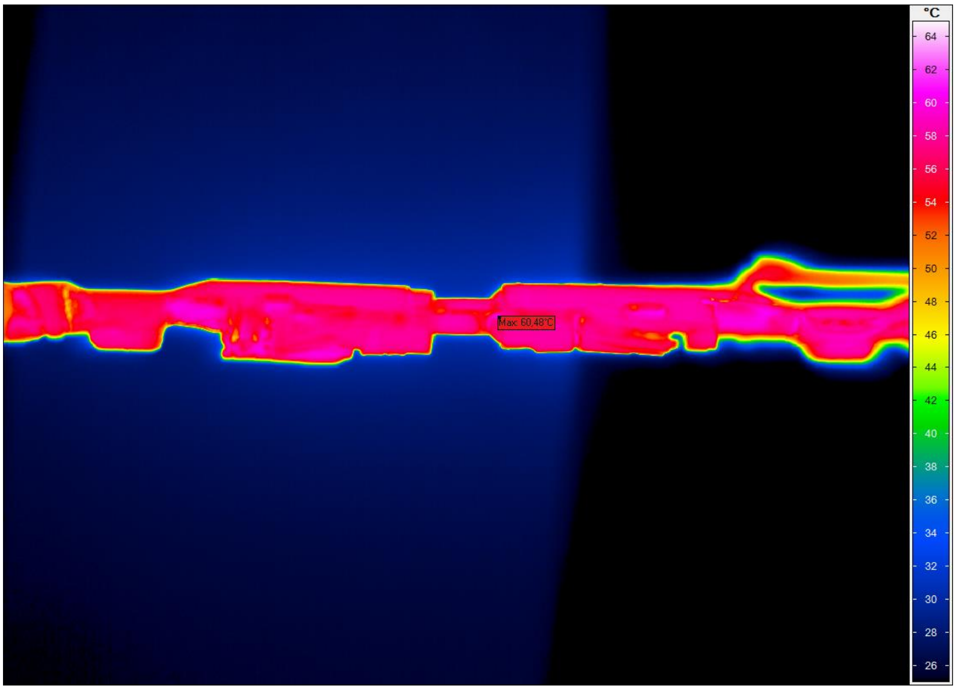

Figure 43. Thermogram of a non-textured pin by applying a current of 16 A. The maximum temperature measured is of 60.48 °C.

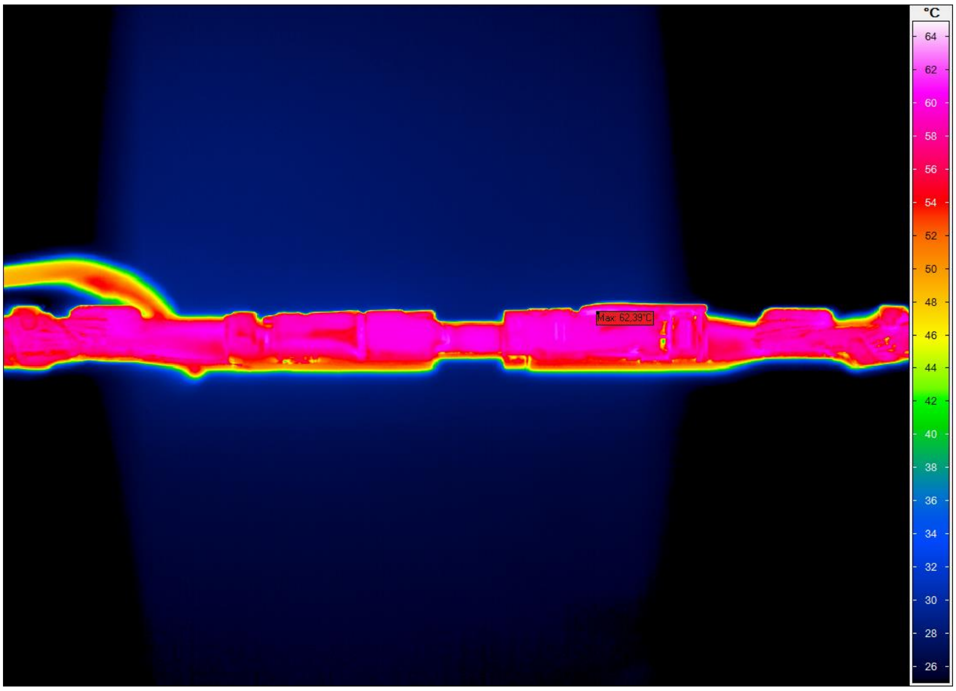

Figure 44. Thermogram of a textured pin by applying a current of 16 A. The maximum temperature measured is of 62.32 °C.

As mentioned above, a black coating was applied over the surface of the connectors in order to obtain thermograms that represent accurately the reality behind the temperature rise on the connector. Despite this, the quality of the thermogram is not very high. Probably, the coating was not sufficiently well applied and as a result, the emissivity/reflection on certain parts of the surface was higher. As the emissivity or the reflection is higher, some parts can be seen warmer than they actually are. The emissivity of objects is dependent on their surface material and its oxidation, but this is also influenced by the roughness of the surface, the temperature and even the viewing angle. On the other hand, polished materials are more reflective. Disregarding this difference in the temperature and assuming that the black paint was not well-applied, it can be said that the temperature is homogeneously distributed along the connectors. This means that no hot-spots are observed among the samples. Therefore, the connectors do not show a punctual zone where the electrical resistance is highly increased due to a failure. Figures 43 and 44 also show the point where the maximum temperature was registered for each sample. For the reference connector the maximum temperature measured was of 60.48 °C and for the texture sample a temperature of 62.32 °C was recorded. These points were located at different positions among the connectors.

The electrical resistance of the whole connectors was also measured before and after the derating testing for further comparison. The results of these measurements are shown in table 5.

Table 5. Electrical resistance before and after the derating test for textured and non-textured pins.

Before Derating Test			
Non-textured pins		Textured pins	
Sample N°	Resistance (mΩ)	Sample N°	Resistance (mΩ)
1	0.74	4	0.69
2	0.70	5	0.73
3	0.71	6	0.70
Average	0.72	Average	0.71

After Derating Test			
Non-textured pins		Textured pins	
Sample N°	Resistance (mΩ)	Sample N°	Resistance (mΩ)
1	0.78	4	0.73
2	0.70	5	0.73
3	0.73	6	0.75
Average	0.74	Average	0.74

As discussed before, the textured and non-textured pins do not show a difference on the electrical resistance of the whole connector. After the derating test, there is no change in the electrical resistance. This is mainly because the highest current load used for the test was below the maximum current admissible for room temperature.

Lastly, the long-term reliability of the connectors was evaluated by storing the samples in a furnace chamber at 120°C during 1000 hours. The electrical resistance of the whole connector was measured before and after the aging test. The results of this measurement are listed in table 6.

Table 6. Electrical resistance before and after the long-term behavior test for textured and non-textured pins.

Before Long-term behavior test			
Non-textured pins		Textured pins	
Sample N°	Resistance (mΩ)	Sample N°	Resistance (mΩ)
1	0.71	6	0.73
2	0.70	7	0.67
3	0.70	8	0.71
4	0.73	9	0.69
5	0.72	10	0.70
Average	0.71	Average	0.70

After Long-term behavior test			
Non-textured pins		Textured pins	
Sample N°	Resistance (mΩ)	Sample N°	Resistance (mΩ)
1	1.10	6	0.91
2	1.11	7	0.96
3	0.96	8	1.03
4	1.00	9	1.12
5	0.89	10	1.03
Average	1.01	Average	1.01

After the heat aging, both set of samples show a rise in the electrical resistance. The resistance becomes greater in approximately 60%. In both cases, a resistance increase from ~ 0.7 mΩ to ~ 1 mΩ can be observed. This change is mainly due to a relaxation of the contact springs. The female terminal is the same for both pins variants. The growth of the intermetallic phase could also play a role on the electrical resistance increase. However, this influence has not been investigated in this work.

Subsequently, the insertion force of the aged samples was registered for nine mating-unmating cycles. Figure 45 shows the force-distance curves of the mating-unmating cycles obtained for a non-textured pin, while figure 46 shows the curves for a textured pin. No insertion force is shown for the first cycle, since after the aging test, the electrical connectors were disconnected in order to carry out a visual inspection, which is presented below.

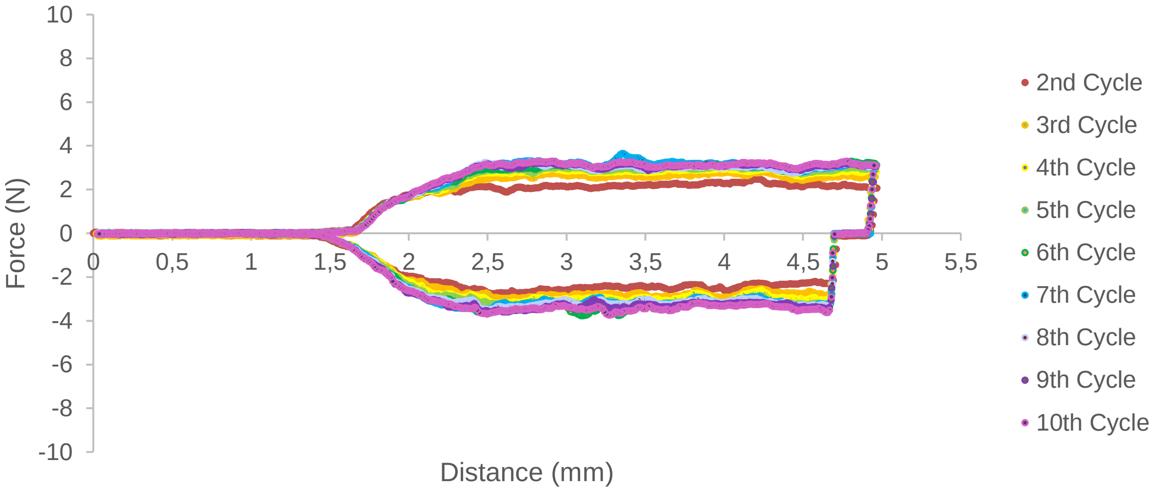

Figure 45. Measured insertion force as function of insertion distance for a non- textured pin after long-term storage.

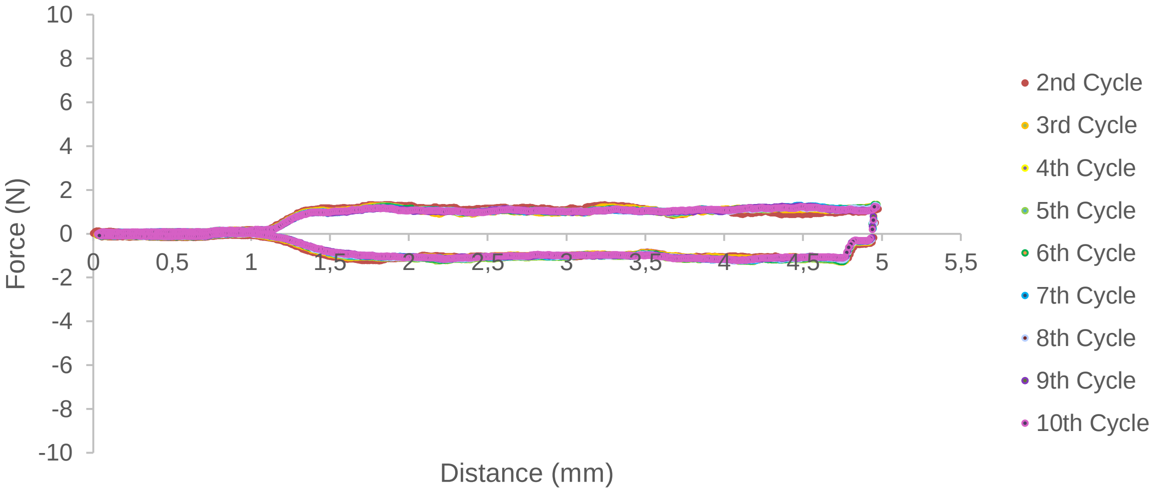

Figure 46. Measured insertion force as function of insertion distance for a textured pin after long-term storage.

After the long-term behavior test, both samples display a decrease in the insertion force. This can be explained considering that the material undergoes a relaxation by being exposed to high temperatures during long times. The contact normal force exerted by the spring beams is reduced as a result of this relaxation, and therefore, there is a reduction in the insertion and withdrawal forces. Figure 47 shows the average of the insertion force as a function of the mating-unmating cycle obtained for both set of textured and non-textured pins for further comparison. As in section 6.3, the maximum and the minimum forces measured in each set of samples are also plotted.

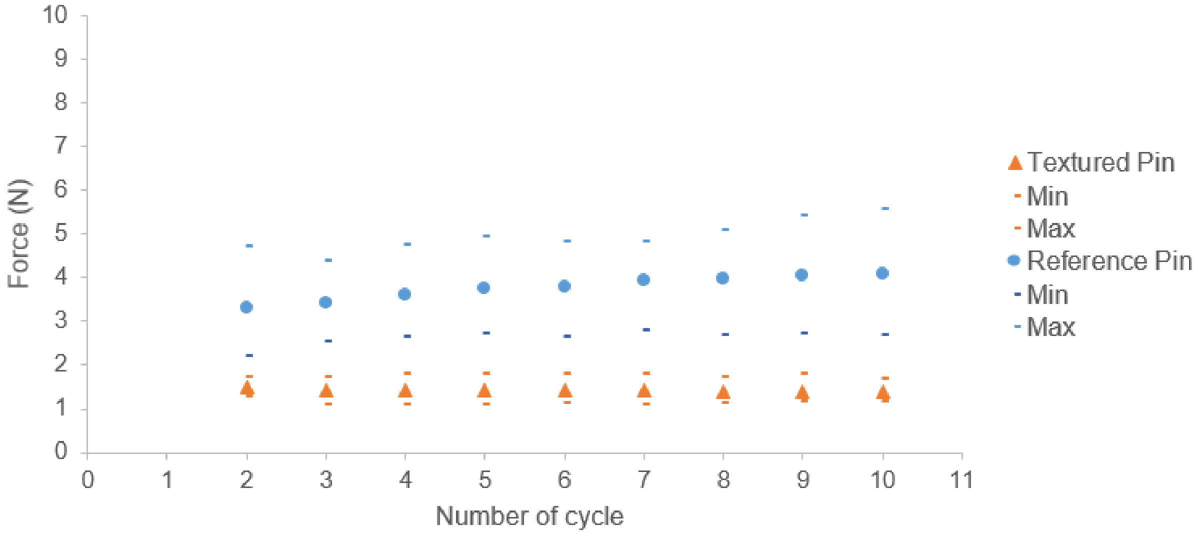

Figure 47. Average of the maximum insertion forces as function of cycle number for textured and non-textured pins after the long-term behavior test. The dashes represent the maximal and minimal insertion force measured for each set of samples.

In figure 47, it is observed that the textured pins show a lower insertion force for all the mating-unmating cycles than the non-textured pins. As seen in section 6.3, the textured pins also display a smaller scattering of the results for each cycle than the reference samples. While the insertion force of the modified pins remains constant over all the mating-unmating cycles, the insertion force of the reference pins increases continually. The average force takes values of ~ 1.5 N for the textured sample. This corresponds to a reduction of the insertion force by more than a factor of 2 compared to the reference contacts by increasing the number of the mating cycle. The non-textured pins show an average force higher than 3 N. At the last cycle, the force reached values up to 5.5 N. As both set of samples have the same spring beams, and the heat was assumed to be homogeneously distributed in the furnace chamber, the relaxation rate of the spring beams is considered to be the same for both of them. Therefore, the difference on the reduction rate of the insertion force should be attributed to the presence of lubricant over the surface of the textured pins. Furthermore, the peak observed in figure 30 for the non-textured sample at the second cycle is not present in figure 47. As previously commented, some grease/oil can remain on the surface during the sample handling and placement on the testing machine. This grease acts as lubricant reducing the friction and, therefore, the insertion force during the first mating-unmating cycle. However, in the second cycle, this grease is no longer available on the surface. The asperities of the surface become enough deformed in order to decrease the surface roughness. After a certain number of cycles, the force increases since the tin plating wears out throughout the mating-unmating cycles and the basis material is reached at some point. All this process is retarded due to the relaxation of the spring beams and also due to the presence of more IMC, which grow during the storage at high temperature and may reach the surface of the pin.

Finally, the results of the visual inspection are presented. The samples were imaged using a camera adapted to a magnifying glass. Figure 48 shows the pictures captured for a textured and a non-textured pin after the storage in the furnace.

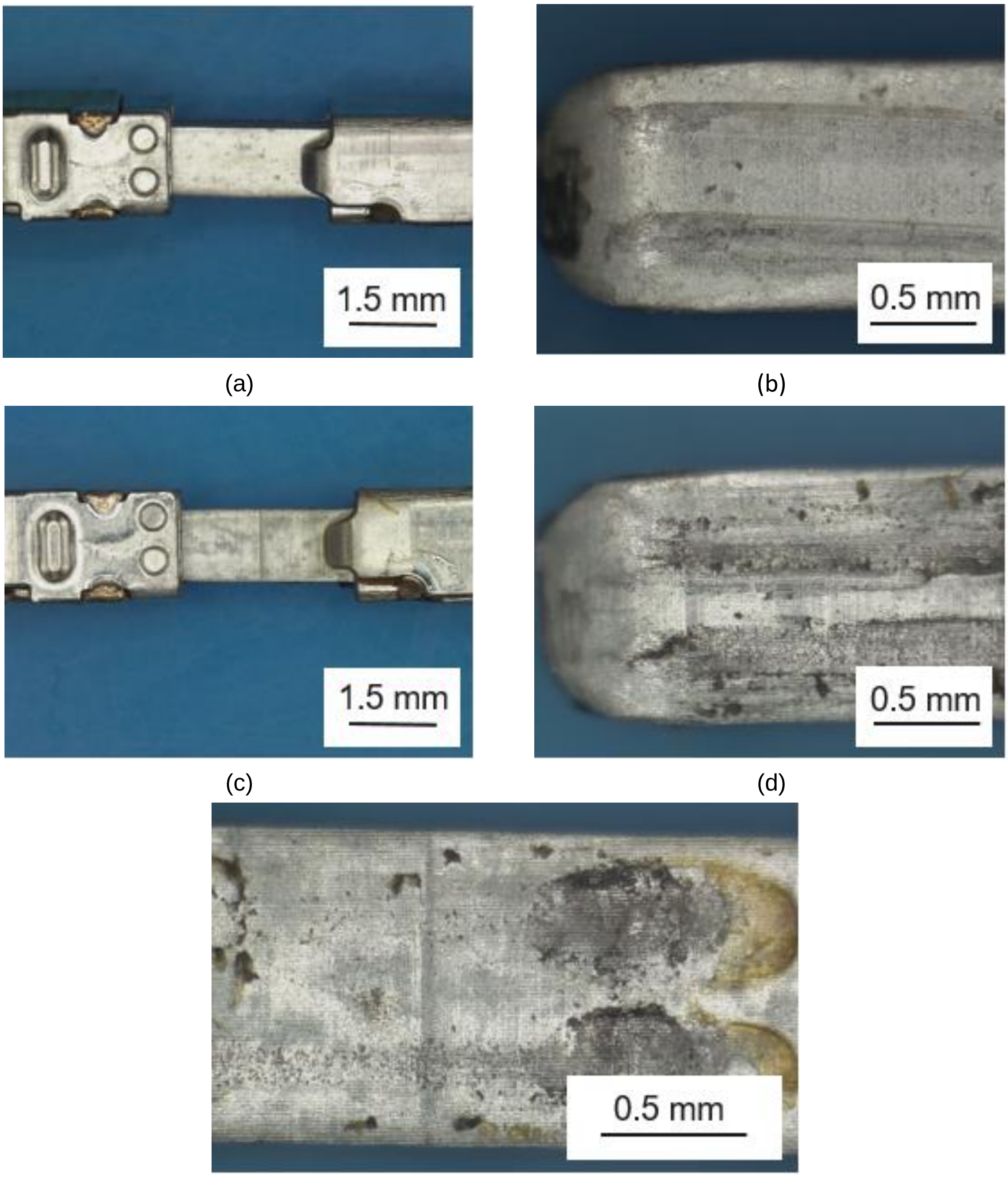

(a) (b) (c) (d) (e)

Figure 48. Pictures of the samples after the long-term aging test. Non-textured pin at a magnification of: (a) 1x and (b) 3x. Textured pin at a magnification of: (c) 1x, (d) 3x and (e) 5x.

There is no difference observed between the non-textured and textured pins shown in figure (a) and (c) respectively.

Concluding this section, it can be highlighted that the textured and non-textured pins show a quite similar electrical response. In spite of having a lower contact resistance, the textured pins present the same electrical resistance as the reference sample. Additionally, no correlation was detected between the electrical resistance of the whole connector and the mating-unmating cycle number. In terms of fretting, a higher fretting resistance was observed for the textured pins. By subsequently measuring the joule heating of the samples, it was demonstrated that both textured and non-textured pins show the same current derating curve. Finally, the pins were aged in order to compare the long-term behavior. The electrical resistance of the connectors increased after the aging test, while the insertion force decreased. Both samples showed the similar increment on the resistance, but in terms of insertion force, the textured pins required lower forces during the mating-unmating cycles. More detailed investigations for comparison are still pending.

7. Conclusion

The demands on electrical connectors have been recently increased driven by the trends in miniaturization and electrification in the automotive industry. The next generation of electrical connectors should comply three main requirements:

- low and stable electrical contact resistance
- high wear resistance against fretting corrosion and,
- reduced insertion and removal forces.

These goals can be achieved by either changing the environment condition, such as high operating temperatures, or selecting a non-noble plating material. In addition to the surface material, the surface finishing has an important role on the electrical and the tribological behavior of connectors. It has been shown that by texturing the surface of the male side of a tin-plated contact, the electrical contact resistance for a given contact normal force can be reduced by a factor of 2. However, this modified surface shows disadvantages in terms of tribology. In this work, an innovative way of enhancing the tribological properties was studied. The main goal of the project was to reduce the insertion force of electrical connectors by enclosing a lubricant within the texture maxima of the surface of pins modified by means of direct laser interference patterning (DLIP). The principal conclusions of this work are detailed here below.

- The presence of porosity within the topography maxima is determined by the period of the texture. The optimal period for this is around 15 µm. The capability of obtaining porosity is also influenced by the laser fluence. Areas irradiated with laser intensities lower than 1000 mJ/cm^2 presented topographies poorly defined and double-peaks in a large area of the pattern. The texture obtained was improved for higher fluences. The laser spot used for texturing presented a significant fluctuation in the intensity distribution. This resulted in an inhomogeneous texture, whereon different regions showed different levels of texturing. Despite the inhomogeneity in the surface depth profile, the peaks increased in height and fewer double-peaks were observed for high fluences. Spots textured with laser fluences between 1050 and 1150 mJ/cm^2 displayed the most homogeneous topography. If the intensity was even higher, the resulted texture was less homogeneous. As the volume of molten material increases, the collision between the different fronts at the interference minima produces liquid drops that solidify at the texture minima forming metallic particles over the surface.

- By means of SEM imaging and FIB cross-sections, the presence of porosity within the texture maxima was confirmed. Both non-textured and textured pin presented formation of intermetallic compounds in the interface between the basis material and the tin-coating layer. The intermetallic phase covered around 60% of the coating layer. No difference was observed in the intermetallic layer after exposing the surface to the interfering laser beams. In addition to the pores in the peaks of the texture, Kirkendall voids were detected between the copper strip and the intermetallic compound layer. Once verified the existence of porosity, samples were textured with PAO 40. They were analyzed through Raman spectroscopy in order to assess the presence of the lubricant within the porosity. The samples were cleaned in an ultrasonic bath prior to carry out the spectroscopy in order to remove all rest of lubricant remained over the surface after the texturing process. PAO 40 signal was obtained for texture maxima as well as for texture minima.

- The insertion force was measured during 10 mating-unmating cycles for textured and non-textured pins. The non-textured pins required an insertion force of 4.5 N in average. For the textured pins, the force decreased continuously by increasing the number of the connections, reaching a force of 2 N in the last cycle. Only after the fifth cycle when the lubricant is released from the texture maxima, the insertion force had a lower value than for the non-textured pins. In order to reduce the number of cycles before this happens, it was proposed to wear the surface on both sides of the textured pins with a nylon brush. In this case, an enhancement in the force was already obtained for the first connection. In the second cycle, a reduction of approximately 50% in the insertion force was observed. By increasing the cycle number, the force stabilized at 1.5 N.

- The coefficient of friction of the textured pins was lower than the value of the reference only after the fifth cycle. As expected, the coefficient of friction was decreased by brushing the surface. It can be explained by considering that brushing reduces the surface roughness in addition to promote the release of the lubricant without the need of wear the texture through the mating-unmating cycles. This favors a lower coefficient of friction and therefore, promotes a lower insertion force. However, the electrical resistance vs. the slide path is jeopardized. The brushed textured pins showed a higher contact resistance than the normal textured pins, similar to the non-textured pins. While the resistance of the reference contacts oscillated around a value of $R \sim 0.7 m\Omega$, the mean value for the textured pins is $R < 0.2 m\Omega$. Optimizing the laser system and laser texturing parameter may be a good approach in order to reduce the coefficient of friction and the insertion force without compromising the electrical behavior of the textured pins.

- The contact resistance was also measured as function of the normal force. The textured samples showed a lower contact resistance over the whole load range than the non-textured samples. In addition, there was no difference in the electrical resistance of the whole connector between textured and non-textured pins, mainly due to the interaction between the parallel contact points.

- The fretting resistance of the textured pins was compared to the non-textured pins. The fretting corrosion is the most important failure mechanism of the tin-plated electrical contacts. Under the convention that a connector failures by fretting when the contact resistance exceeds 1 mΩ, the textured pins resulted more stable against fretting corrosion. They resisted the double of cycles than the non-textured pins. This was achieved by reducing the dynamic COF due to presence of PAO 40.

- The temperature rise of the textured and non-textured pins was also compared. By changing the current applied to the whole electrical connector, no difference between textured and non-textured pins was observed. Both samples showed a maximal current capacity of around 20.5 A.

- Lastly, the long-term reliability of the connectors was evaluated. After aging, both textured and reference samples showed a rise in the electrical resistance of approximately 60%. In addition, both samples displayed a decrease in the insertion force. This can be explained considering that the material undergoes a relaxation by being exposed to high temperatures during long times. The insertion force took values of ~ 1.5 N for the textured sample. This corresponds to a reduction of more than 50% compared to the reference contacts.

It was demonstrated that a decrease in the insertion force of pins is obtained by enclosing lubricant in the porosity of the texture obtained by DLIP. The enhancement in the mating-unmating process was achieved without compromising the electrical performance of the connectors.

8. Future perspective

Based on the above conclusions, the goal for the future is to achieve a significant reduction in the insertion force from the first cycle. Some practical suggestions for future research are made here below:

- To texture the surfaces by means of a higher-power monolithic laser, which could be a good solution. This would allow a homogeneous texturing of the entire pin surface with only one laser pulse.
- To adjust the laser power in such way pores are obtained more near the maxima surface or even, maxima partially opened could be obtained. In these cases, the lubricant would be released without the need of wear the texture a lot, favoring a low insertion force already in the first connection without compromising the electrical performance of the contact.
- To study further material properties after texturing. Laser treatment may influence the microstructure, the grain size and orientation, and the defect density. This could lead to a change in the mechanical properties such as hardness, which directly influences the frictional and electrical properties.
- To characterize the intermetallic compounds between the copper and the tin layer. As these compounds may have different properties to the initial material such as the absorption coefficient and the thermal diffusivity, they can affect the texturing process.

9. References

[1] MarketsandMarkets (2017, March). *Automotive Connectors Market by Connection Type (Wire to Wire, Wire to Board, Board to Board), Application (Body Control & Interiors, Engine Control & Cooling System), System Type (Sealed, Unsealed), Vehicle Type, and Region - Global Forecast to 2021.* Retrieved from https://www.marketsandmarkets.com/PressReleases/automotive-connector.asp

[2] Trinh, K.; Mücklich, F.; Leidner, M.; Schmidt, H. (2015) *Einfluss von Laser-Oberflächentexturierung auf die Mikrostruktur und das elektrische Verhalten zinnbeschichteter Steckverbinderwerkstoffe.* In 5. Symposium Connectors, Lemgo.

[3] Leidner, M. (2009) *Kontaktphysikalische Simulation von Schichtsystemen* (Doctoral Dissertation).

[4] Gissila, Tibebu. (2013) *Connectors and Vibrations – Damages in Different Electrical Environment* (Master’s Thesis).

[5] Trinh, K. (2015) *Laserinterferenztexturierung elektrischer Steckverbinder für die Automobilindustrie* (Doctoral Dissertation).

[6] Park, Y.W.; Sankara Narayanan, T; Lee, K. Y. (2007) *Fretting corrosion of tin-plated contacts: Evaluation of surface characteristics*. Tribol. Int., Vol. 40, pp. 548-559.

[7] Park, Y.W.; Sankara Narayanan, T; Lee, K. Y. (2007) *Effect of temperature on the fretting corrosión of tin plated copper alloy contacts.* Wear, Vol. 262, pp. 320-330.

[8] Park, Y.W.; Jung, J. P.; Lee, K. Y. (2006) *Overview of fretting corrosion in electrical connectors*. International Journal of Automotive Technology, Vol. 7, No. 1, pp. 75□82

[9] Mroczkowski, R. S. (1993) *Connector Design/Materials and Connector Reliability*. AMP Incorporated (Technical Paper).

[10] Ito, T.; Matsushima, M.; Takata, K.; Hattori, Y. (2007) *Factors Influencing Fretting Corrosion of Tin Plated Contacts.* SEI Technical Review, No. 64, pp 03-08

[11] Watanabe, H.; Saka, Y.; Furukawa, K.; Saitoh, Y. (2017) *Terminal Plating to Lower Insertion Force of Multiway Connectors*. SEI Technical Review, No. 84, pp 131-136.

[12] Groover, M. (2010) *Fundamentals of Modern Manufacturing: Materials, Processes and Systems.* United States of America: John Wiley & Sons, Inc.

[13] Gedeon, M. (2012) *Connector Insertion Force*. Materion Brush Performance Alloys. Technical Tidbits. Issue No. 44.

[14] Hsu, Y.L; Hsu, Y.C; Hsu, M.S (2002) *Shape Optimal Design of Contact Springs of Electronic Connectors.* Journal of Electronic Packaging, Vol. 124, Issue No. 3.

[15] Larsen, R. (2016) *A New Technology for High Current, Low Insertion Force, Low Resistance and Long Cycle Life Power Connectors*. Methode Power Solutions (Technical White Paper).

[16] Leidner, M.; Myers, M.; Schmidt, H.; Sachs, S.; Thoss, S. (2014) *Enhancing the contact interface by matching the surface pressure and current density distribution.* 27th International Conference on Electrical Contacts, pp. 1-6.

[17] Trinh,K.; Mücklich, F.; Ramos-Moore, E. (2014) *The role of microstructure and surface topography in the electrical behaviour of Sn-coated Cu contacts*. 27th International Conference on Electrical Contacts, pp. 243-248.

[18] Trinh, K.; Ramos-Moore, E.; Green, I.; Pauly, C.; Zamanzade, M.; Mücklich, F. (2017) *Topographical and Microstructural Effects of Laser Surface Texturing on Tin-Coated Copper*

Electrical Connectors Under Load Cycling. Components, Packaging and Manufacturing Technology, Vol. 7, No. 4, pp 582-590.

[19] Leidner, M.; Thoss, S.; Schmidt, H.; Reinert, L.; Trinh, K.; Schäfer, C. (2017) *Verbesserung der tribologischen und elektrischen Eigenschaften von Zinn-Kontaktoberflächen durch Partikel/Schmierstoff-Einbettung mittels Laser-Texturierung.* In 6. Symposium Connectors, Lemgo.

[20] Braunovic, M.; Konchits, V. V.; Myshkin, N. K. (2007) *Electrical Contacts: Fundamentals, Applications and Technology*. Boca Raton, United States of America: Taylor & Francis Group, LLC.

[21] Advanced Probing Systems, Inc. (1999, May) *Fundamentals of Contact Resistance, Part I – Contact Theory*. Technical Bulletin H.

[22] Holm, R. (1967) *Electric Contacts: Theory and Application*. New York, United States of America : Springer-Verlag Berlin Heidelberg.

[23] Tyco Electronics (2009) *Connectors 101: What Lighting Designers Need to Know*. Retrieved from: http://www.te.com/content/dam/te-com/documents/industrial-intelligent-buildings/global/TE_Connectors_101_Lighting_Article_0409.pdf

[24] Schmidt H. (2010) *Steckverbinderkontakte*. EKON/ITG-Fachtagung 2010.

[25] Kugler, M. (2014) *Evaluierung der mechanischen und elektrischen Eigenschaften nicht Hertzscher Kontaktpaare* (Bachelor’s Thesis).

[26] Kaiser, V. (2016, August) *Connectors - Technologies and Trends -.* ZVEI, German Electrical and Electronic Manufacturers’ Association.

[27] Knoblauch, G. (2006) *Steckverbinder II: Neue Technologien, Produkte und Management-Konzepte.* Reinningen, Germany: Expert Verlag.

[28] Heile, I.; Hüske, R. (2017) *Contact plating material options for electronic connectors: A comparison of hard gold and hard gold flashed palladium-nickel (80/20)*. (White Paper) HARTING AG & Co. KG.

[29] Locker, G. (1998) *Fretting Corrosion of Tin Plated Separable Connectors Used in Automotive Applications* (Doctoral Dissertation).

[30] Gunnarsson Sarius, N. (2010) *Surface Technology for Optimal and Electrical Connectors* (Doctoral Dissertation).

[31] Song, J.; Wang, L.; Zibart, A; Koch, C. (2012) *Corrosion Protection of Electrically Conductive Surfaces.* Metals, 2, pp 450-477.

[32] Gedeon, M. (2011) *Coating Electrical Contacts*. Materion Brush Performance Alloys. Technical Tidbits. Issue No. 31.

[33] Goradia, P.; Ijeri, V.; Shah, K.; Dere, T.; Gurav, S. (2014) *Plating of tin and tin alloys from methanesulfonic acid baths*. In Indian Surface Finishing Conference, Mumbai.

[34] MFSA (1987) *Tin and Tin Alloys Coatings*. Quality Metal Finishing Guide, Vol. I, No. 3. Retrieved from: http://infohouse.p2ric.org/ref/25/24481.pdf

[35] Schlesinger, M.; Paunovic, M. (2010) *Modern Electroplating.* Hoboken, United States of America: John Wiley & Sons, Inc.

[36] Elmgren, P.; Dixon, D.; Hilty, R.; Moyer, T.; Lal, S.; Nitsche, A.; Teuber, F. (2018*) Pure Tin - The Finish of Choice for Connectors*. Retrieved from: http://www.heilindasia.com/rohs/fci/LF_Joint_Position_Connector_Industry.pdf

[37] Cornelius, B.; Treivish, S.; Rosenthal, Y.; Pecht, M. (2017) *The phenomenon of tin pest: A review.* Microelectronics Reliability, vol.79, pp 175-192.

[38] Böwering, N. (2017) *Induction of tin pest for cleaning tin-drop contaminated optics.* Materials Chemistry and Physics, vol.1-98, pp 236-242.

[39] STMicroelectronics (2006) *Control of whisker growth in Tin alloy coatings*. Application Note AN2035.

[40] Osterman, M. (2006) *Assessing the Risk Posed by Tin Whiskers* (PowerPoint Presentation). Center for Advanced Life Cycle Engineering. University of Maryland. Retrieved from: https://web.calce.umd.edu/lead-free/SMTAOnline.pdf

[41] Lavery, P. *Strategies to mitigate the tin whisker phenomenon* (White Paper) Vicor Corporation. Retrieved from: http://www.vicorpower.com/documents/rohs/tin_whisker_mitigation_strategies.pdf

[42] Tu, K.; Suh, J.; Wu, A.; Tamura, N.; Tung, C. (2005) *Mechanism and Prevention of Spontaneous Tin Whisker Growth.* Materials Transactions, Vol. 46, No. 11, pp 2300-2308.

[43] Kostic, A. D. (2011) *Lead-Free Electronics Reliability – An Update* (Technical Paper). Aerospace Corporation. Retrieved from: https://nepp.nasa.gov/whisker/reference/tech_papers/2011-kostic-pb-free.pdf

[44] Gaylon, F. (2004) *A History of Tin Whisker Theory: 1946 to 2004*. In SMTAI International Conference, Chicago.

[45] Révay, L. (1977) *Interdiffusion and formation of intermetallic compounds in tin-copper alloy surface coatings*. Surface Technology, Vol. 5, pp 57-63.

[46] APL Oberflächentechnick GmbH. (2016) *Intermetallic Copper/Tin Phases* (White Paper).

[47] Saunders, N.; Miodownlk, A. P. (1990) *The Cu-Sn (Copper-Tin) System*. Bulletin of Alloy Phase Diagrams, Vol. 11, No. 3, pp 278-287.

[48] Fürtauer, S.; Li, D.; Cupid, D.; Flandorfer, H. (2013) *The Cu-Sn phase diagram, Part I: New experimental results*. Intermetallics, Vol. 34, pp 142-147.

[49] Olson, A. *What are Intermetallics and how can we overcome the failures associated with them?* (Technical Paper). STI Electronics, Inc.

[50] Slade, P. (2014) *Electrical Contacts: Principles and Applications.* Boca Raton, United States of America: Taylor & Francis Group, LLC.

[51] Reichenecker, W. J. (1980) *Electrical Conductivity of the Copper-Tin Intermetallic Compound Cu3Sn in the Temperature Range -195°C to +150°C*. WRC Bulletin 257, pp 308-310.

[52] Gasser, Ph.; Jacob,P.; Leroy, D.; Oberli, L.; Scheuerlein, C.; Taborelli, M. (2004) *The Effect of CuSn Intermetallics on the Interstrand Contact Resistance in Superconducting Cables for the Large Hadron Collider (LHC)*. Large Hadron Collider Project – Project Report 801. European Organization for Nuclear Research – European Laboratory for Particle Physics.

[53] Shang, P. J.; Liu, Z. Q.; Pang, X. Y.; Li, D. X.; Shang, J. K. (2009) *Growth mechanisms of* Cu_3Sn *on polycrystalline and single crystalline Cu substrates*. Acta Materialia, Vol. 57, pp 4697-4706.

[54] Li, J. F.; Agyakwa, P.A; Johnson, C. M. (2011) *Interfacial reaction in Cu/Sn/Cu system during the transient liquid phase soldering process.* Acta Materialia, Vol. 59, pp 1198-1211.

[55] Chan, Y.; So, A.; Lai, J. (1998) *Growth kinetic studies of Cu–Sn intermetallic compound and its effect on shear strength of LCCC SMT solder joints*. Materials Science and Engineering B55, pp. 5-13.

[56] Weinberg, K.; Böhme, T. (2009) *Condensation and Growth of Kirkendall Voids in Intermetallic Compounds*. Components and Packaging Technologies, Vol. 32, Issue 3, pp 684-692.

[57] Weimber, K.; Böhme, T.; Müller, W. (2009*) Kirkendall voids in the intermetallic layers of solder joints in MEMS*. Computational Materials Science, Vol. 45, Issue 3, pp 827-837.

[58] Park, J.M.; Kim, S.H.; Jeong, M.H.; Park, Y.B (2014) *Effect of Cu–Sn intermetallic compound reactions on the Kirkendall void growth characteristics in Cu/Sn/Cu microbumps*. Japanese Journal of Applied Physics, Vol. 53, 05HA06.

[59] Gedeon, M. (2011) *Nickel as an Undercoating*. Materion Brush Performance Alloys. Technical Tidbits. Issue No. 36.

[60] Tegehall, E. (2006) *Review of the Impact of Intermetallic Layers on the Brittleness of Tin-Lead and Lead-Free Solder Joints.* IVF Project Report 06/07.

[61] So, A.; Chan, Y.; Lai, J. (1997) *Aging Studies of Cu-Sn Intermetallic Compounds in Annealed Surface Mount Solder Joints.* Components, Packaging, and Manufacturing Technology – Part B, Vol. 20, No. 2, pp 161-166.

[62] Lindborg, U.; Asthner, B.; Lind, L.; Révay, L. (1976) *Intermetallic Growth and Contact Resistance of Tin Contacts After Aging.* Parts, Hybrids, and Packaging, Vol. PHP-12, No. 1, pp 33-39.

[63] Chia, P.Y.; Haseeb, A.; Mannan, S. (2016) *Reactions in Electrodeposited Cu/Sn and Cu/Ni/Sn Nanoscale Multilayers for Interconnects.* Materials, Vol. 9, Issue 6.

[64] Tamai, T.; Nabeta, Y.; Sawada, S.; Hattori, Y. (2010) *Property of Tin Oxide Film Formed on Tin-Plated Connector Contacts*. In 56th IEEE Holm Conference on Electrical Contacts, Charleston.

[65] Lee, A.; Mao, A.; Mamrick, M. S. (1988) *Fretting Corrosion of Tin at elevated temperatures.* In 34th IEEE Holm Conference on Electrical Contacts, San Francisco.

[66] Antler, M. (1985) *Electrical Effects of Fretting Connector Contact Materials: A Review.* Wear, Vol. 106, pp 05-33.

[67] Malucci, R. D. (2003) *Fretting Corrosion Degradation, Threshold Behavior and Contact Instability.* In 49th IEEE Holm Conference on Electrical Contacts, Washington.

[68] Braunovic, M. (2009) *Fretting in Electrical/Electronic Connections: A Review.* IEEE Transaction on Electron Devices, Vol. E92-C, No.8, pp 982-991.

[69] AMP Incorporated (2004) *The Tin Commandments: Guidelines For The Use Of Tin On Connector* (Technical Report).

[70] Madeni, J.; Liu, S. (2011) *Effect of Thermal Aging on the Interfacial Reactions of Tin-Based Solder Alloys and Copper Substrates and Kinetics of Formation and Growth of Intermetallic Compounds*. Soldag. Insp. São Paulo, Vol. 16, No. 1, pp 86-95.

[71] Wieland-Werke AG. *Hot-dip tinned copper and copper alloy strip*. Retrieved from: https://www.wieland.com/mediaPool/content/media/en/prospekte/baender_und_bleche_1/feuer verzinnte_baender.pdf

[72] Bürstner, G.; Fröhlich, E. (1997) *Electroplating versus Hot-Dipped Tinning: A comparison of applications/experiences.* In CARTS-Europe ’97 Symposium, Prague.

[73] Wieland-Werke AG. *Electroplated strip*. Retrieved from: http://www.nemcometals.co.uk/common media/content/media/en/prospekte_2/walzprodukte/101021_galvanisch_veredelte_baender.pdf

[74] Prieur, P. (2013) *Risk Assessment of Tin Whisker Impact on Electronic Components* (White Paper). Schneider Electric. Retrieved from: https://www.se.com/za/documents/support/white-papers/energy-efficiency/Tin-whiskers-risks-management.pdf

[75] *Laser Fundamentals* (n.d) Retrieved from: http://www.navsea.navy.mil/Portals/103/Documents/NSWC_Dahlgren/Laser/fundamentals.pdf

[76] Martínez Morillo, M.; Sendra Portero, F. *Láser* (n.d) Retrieved from: http://www.sld.cu/galerias/pdf/sitios/rehabilitacion-fis/laser_morrillo.pdf

[77] Singh, S. C.; Zeng, H.; Guo, C.; Cai, W. (2012) *Lasers: Fundamentals, Types, and Operations*. Nanomaterials: Processing and Characterization with Lasers. Published by Wiley-VCH Verlag GmbH & Co. KGaA.

[78] Alvarez Rueda, A. (2016) *Estudio y construcción de un láser de Nd:YAG en configuración fundamental y de segundo armónico* (Bacherlor's Thesis).

[79] Alonso Fernández, B.; Borrego Varillas, R.; Hernández García, C.; Pérez Hernández, J. A.; Romero Vázquez, C. (2016) *El Láser: la luz de nuestro tiempo*. Retrieved from: http://docplayer.es/1678014-El-laser-la-luz-de-nuestro-tiempo.html

[80] Kärtner, F. (2006) *Fundamentals of Photonics: Quantum Electronics*. MIT Course. Retrieved from: https://ocw.mit.edu/courses/electrical-engineering-and-computer-science/6-974-fundamentals-of-photonics-quantum-electronics-spring-2006/lecture-notes/chapter7.pdf

[81] Fisher, J.; Zimmerman, E.; Murphy, M. (2016) *Fundamentos de la Física Láser, Óptica y Características de Funcionamiento para el Clínico TRT un Concepto Anticuado*. The American Board of Laser Surgery.

[82] Klotzkin, D. J. (2014) *Introduction to Semiconductor Lasers for Optical Communications: An Applied Approach*. New York, United States of America: Springer.

[83] Dahotre, N.; Harimkar, S. (2008) *Laser Fabrication and Machining of Materials*. New York, United States of America: Springer.

[84] Brown, M. S.; Arnold, C. B. (2010) *Fundamentals of Laser-Material Interaction and Application to Multiscale Surface Modification* in Laser Precision Microfabrication, vol. 135, K. Sugioka, M. Meunier, and A. Piqué, Eds. Springer Berlin Heidelberg, pp. 91–120.

[85] Bäuerle, D. (2011) *Laser Processing and Chemistry*. Springer Berlin Heidelberg.

[86] *Review of laser-matter interaction* (n.d) Retrieved from: https://www.io.csic.es/Web_GPL/personal

_pages/Jan/thesis/Chap1.pdf

[87] Samant, A. N.; Dahotre, N. (2009) *Laser machining of structural ceramics – A review*. Journal of the European Ceramic Society 29, pp 969-993.

[88] Lasagni, A.; Gachot, C.; Trinh, K.; Hans, M.; Rosenkranz, A.; Roch, T.; Eckhardt, S.; Kunze, T.; Bieda, M.; Günther, D.; Lang, V.; Mücklich, F. (2017) *Direct laser interference patterning, 20 years of development: from the basics to industrial applications*. Proc. SPIE 10092, Laser-based Micro- and Nanoprocessing XI, vol. 1009211.

[89] Zabila, Y.; Perzanowski, M.; Dobrowolska, A.; Kac, M.; Polit, A. (2009) *Direct Laser Interference Patterning: Theory and Application*. Acta Physica Polonica A, vol. 115, No. 2.

[90] Lasagni, A.; D'Alassandria M.; Giovanelli, R.; Mücklich, F. (2007) *Advanced design of periodical architectures in bulk metals by means of Laser Interference Metallurgy.* Applied Surface Science, vol. 254, pp 930-936.

[91] Lasagni, A.; Bieda, M.; Roch, T.; Langheinrich, D. (2011) *Direct Fabrication of Periodic Structures on Surfaces: Laser Interference Patterning as new scalable industrial tool.* Laser Micro-Processing. WILEY-VCH Verlag GmbH & Co. KGaA, Weinheim, Germany.

[92] Mücklich, F.; Lasagni, A.; Daniel, C. (2006) *Laser Interference Metallurgy – using interference as a tool for micro/nano structuring*. Carl Hanser Verlag, Munich, Germany.

[93] Rosenkranz, A.; Hans, M.; Gachot, C.; Thome, A.; Bonk, S.; Mücklich, F. (2016) *Direct Laser Interference Patterning: Tailoring of Contact Area for Frictional and Antibacterial Properties.* Lubricants, Vol. 4, No. 2.

[94] Lasagni, A. (2006) *Advanced design of periodical structures by laser interference metallurgy in the micro/nano scale on macroscopic areas* (Doctoral Dissertation).

[95] Gachot, C.; Rosenkranz, A.; Reinert, L.; Ramos-Moore, E.; Souza, N.; Müser, M.; Mücklich (2013) *Dry Friction Between Laser-Patterned Surfaces: Role of Alignment, Structural Wavelength and Surface Chemistry.* Tribol. Lett., vol. 49, pp 193-202.

[96] Myers, M.; Leidner, M.; Schmidt, H. (2011) *Effect of Contact Parameters on Current Density Distribution in a Contact Interface*. IEEE 57th Holm Conference on Electrical Contacts in Minneapolis, United States.

[97] Lasagni, A.; Benke, D.; Kunze, T.; Bieda, M.; Eckhardt, S.; Roch, T.; Langheinrich, D.; Berger, J. (2015) *Bringing the Direct Laser Interference Patterning Method to Industry: a One Tool-Complete Solution for Surface Functionalization.* Journal of Laser Micro/Nanoengineering, Vol. 10, No. 3.

[98] Leidner, M.; Thoss, S.; Schmidt, H.; Poliseno, J. C.; Reinert, L.; Schäfer, C.; Mücklich, F. (2017) *Verbesserung der tribologischen und elektrischen Eigenschaften von zinnbeschichteten Steckverbindern mittels Laser-Texturierung*. In 24th Albert-Keil-Kontaktseminar, Karlsruhe.

[99] TE Connectivity (2016) *MCON Interconnection System for the Automotive Industry*. Catalogue 1308070-4. Retrieved from http://www.te.com/content/dam/te-com/documents/automotive/global/mcon-interconnection-system-1308070-4.pdf

[100] TE Connectivity (2015) *MCON 1.2 mm Contact System*. Application Specification 114-18464

[101] Stabroth, W. (2016) *MCON 8: New Interconnection System for Current Requirements of Vehicle Electrification.* (White Paper) Retrieved from: http://www.te.com/content/dam/te-com/documents/automotive/global/160603_WhitePaper_MCON_8_06-2016_engl_CLEAR.pdf

[102] Glaser, S.; Stabroth, W. (2016) *HPF 1.2 – New Interconnection System for Extreme Vibration Requirements in the Vehicle.* (White Paper) Retrieved from: http://www.te.com/global-en/industries/automotive/insights/hpf-1-2-new-interconnection-system.html?tab=pgp-story

[103] Fox, T. (2016) *Einführung und Validierung eines abbildenden Aufbaus zur Laserinterferenzstrukturierung* (Bachelor's Thesis).

[104] Zygo Corporation. *NewView 7200 & 7300 Operating Manual*, OMP-0536E (2011)

[105] Gurvinder Singh Bumbrah; Rakesh Mohan Sharma (2016) *Raman spectroscopy – Basic principle, instrumentation and selected applications for the characterization of drugs of abuse*. Egyptian Journal of Forensic Science, vol. 6, pp. 209-215.

[106] Bindu Madhavi, K.; Sowmya, B. H.; Sandeep, B.; Lavanya, M. (2014). *Derating Analysis for Reliability of Components*. International Journal of Engineering Research and General Science, vol. 2, pp. 39-43.

[107] Brummett, S. L. (1982) *Reliability Parts Derating Guidelines*. Final Technical Report - Boeing Aerospace Company.

[108] Raman Data and Analysis: Raman Spectroscopy for Analysis and Monitoring. Retrieved from: http://www.horiba.com/fileadmin/uploads/Scientific/Documents/Raman/bands.pdf

[109] Raman Band Correlation Table. Retrieved from: https://www.utsc.utoronto.ca/~traceslab/raman%20correlation%20table.pdf

[110] Dispersive and FT-Raman Spectroscopic Methods in Food Analysis. Retrieved from: http://www.rsc.org/suppdata/ra/c4/c4ra12463d/c4ra12463d1.pdf

[111] RRUFF Project website containing an integrated database of Raman spectra, X-ray diffraction and chemistry data for minerals. http://rruff.info/

[112] Van Dijk, P.; Van Meijl, F. (1996) *Problems Due to Fretting and Their Solutions*. AMP Journal of Technology, Vol. 5.

Annex I

In [5,17], Trinh has demonstrated the presence of the intermetallic phase Cu_6Sn_5 (η) by means of x-ray diffraction analysis. Figure 1 shows x-ray diffractograms obtained for textured and non-textured samples. Two different plating techniques were also compared in the following figure. The results for hot-dip tinned samples are illustrated in figure 1 a. Figure 1 b shows the characterization of electroplated samples.

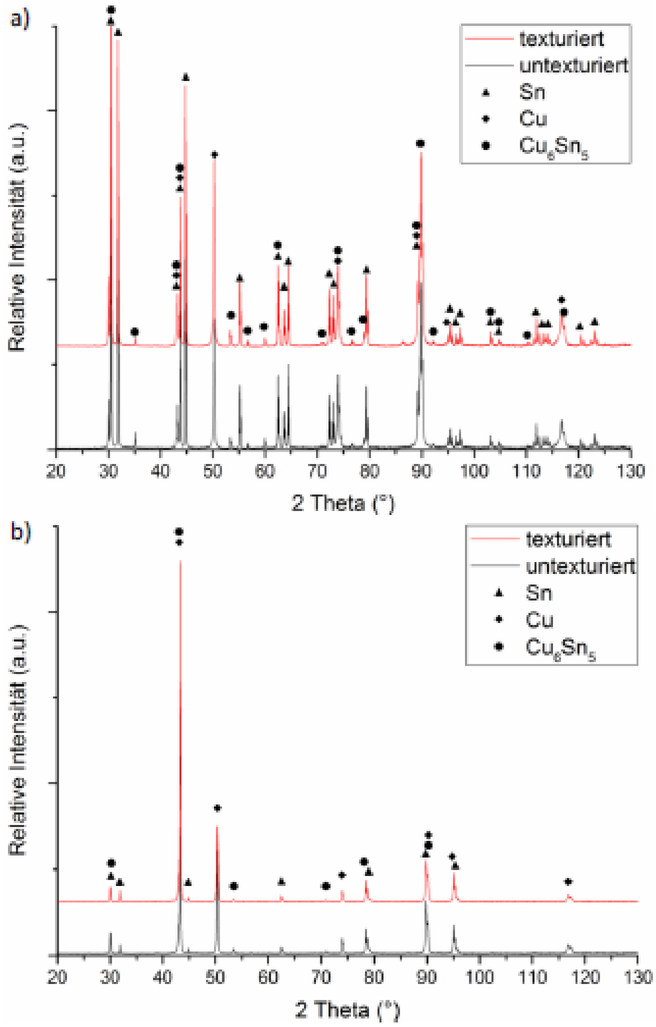

Figure 1. DRX analysis before and after laser texturing (untexturiert and texturiert respectively). The intensity (*Relative Intensität*) is plotted as a function of the diffraction angle (*2 Theta*). The intensity is given in arbitrary units, a.u. a) Hot-tinned sample (fluence: 355 mJ/cm^2 and period 7.5 µm); b) Electro-tinned sample (fluence: 515 mJ/cm^2 and period 7.5 µm). In addition to tin (▲) and copper (♦) phases, the intermetallic phase Cu_6Sn_5 (●) was also detected [5,17].

In figure 1 a, the samples show three strong peaks at 30.5 °, 31.7 ° and 44.8 °. At these angles, the strongest peaks of β-tin are expected, corresponding to the (200), (101) and (211) planes respectively. Further strong peaks were observed at 43.7 ° and 50.3 °. These could be assigned to the (111) and (200) planes of copper, respectively. The reflections of the intermetallic Cu_6Sn_5 are partially overlapped with those of the purely metallic copper or tin phase. Thus, the peak in the range of 30.5 ° could also be assigned to the (311) or (-113) planes of Cu_6Sn_5. Furthermore, the peak at 43.0 ° is assigned to the (132) or (204) planes, while at 43.3 ° the peak could be related to (510) or (-314) planes. All these peaks are registered for samples before and after laser texturing. There is no difference on the diffractogram in terms of peaks position and intensity. Therefore, the thermal effect of the laser does not result in the formation of new intermetallic phases.

For the case of electroplated samples, less peaks are observed in figure 1 b. Particularly, there is a lower amount of tin and Cu_6Sn_5 peaks. In addition, some peaks show a lower intensity. This can be partly explained by considering the difference on the thickness of the tin layer. By electroplating, the tin layer results thinner than by hot-dip plating. A tin layer of 633 nm is obtained by the first technique, while the thickness of the tin layer of a hot-dip plated sample is approximately 2 μm [5,17].

Annex II

The Raman Spectra obtained in order to confirm the presence of lubricant within the texture maxima are presented here below.

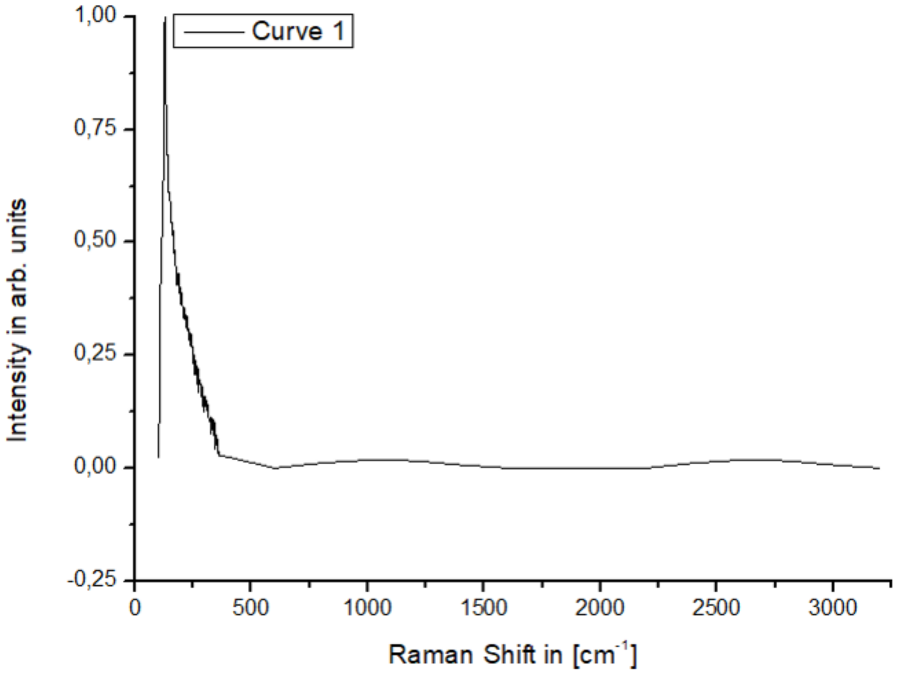

Figure 1. Raman spectrum of a non-textured pin. Curve 1 in figure 22.

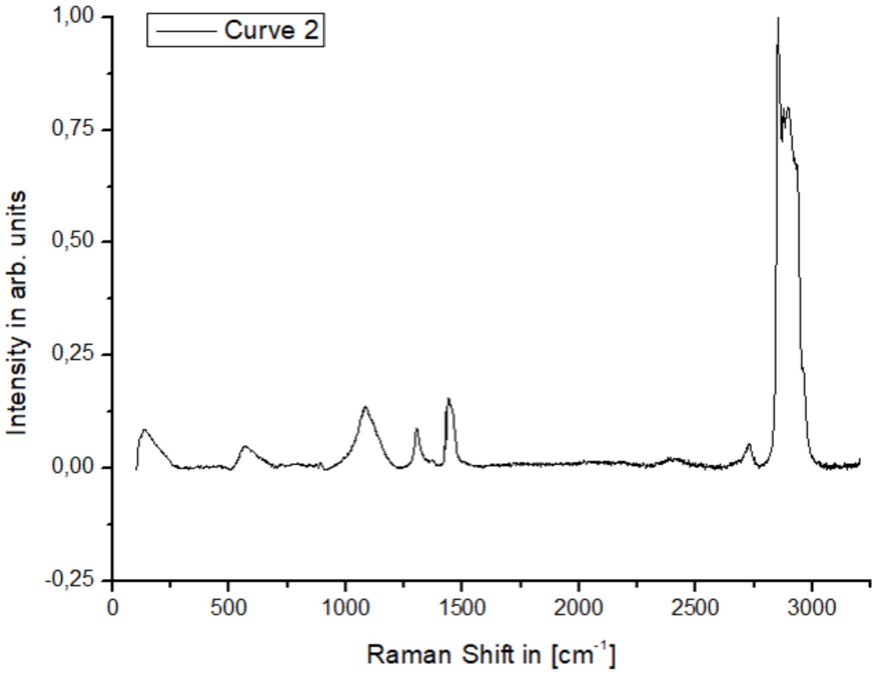

Figure 2. Raman spectrum acquired of lubricant PAO 40. Curve 2 in figure 22.

Table 1. Assignment of functional groups to the absorption peaks obtained for PAO 40. The table also shows the peaks intensity. The theoretical range of the absorption bands for the assignment was extracted from [108-110]

Peak Number	**Raman Shift [cm^{-1}]**	**Peak Assignment**	**Intensity**
1	136.11	-	-
2	563.59	Si-O-Si (glass microscope slide)	weak
3	1084.52	C-C aliphatic chain vibrations CH_3	medium
4	1303.87	C-H / CH_2	weak
5	1403.04	C-H / CH_2 / CH_3	medium
6	2728.54	CH_2 / CH_3	weak
7	2854.17	CH_2	strong
8	2898.04	CH_3	strong
9	2943.63	CH_2	medium

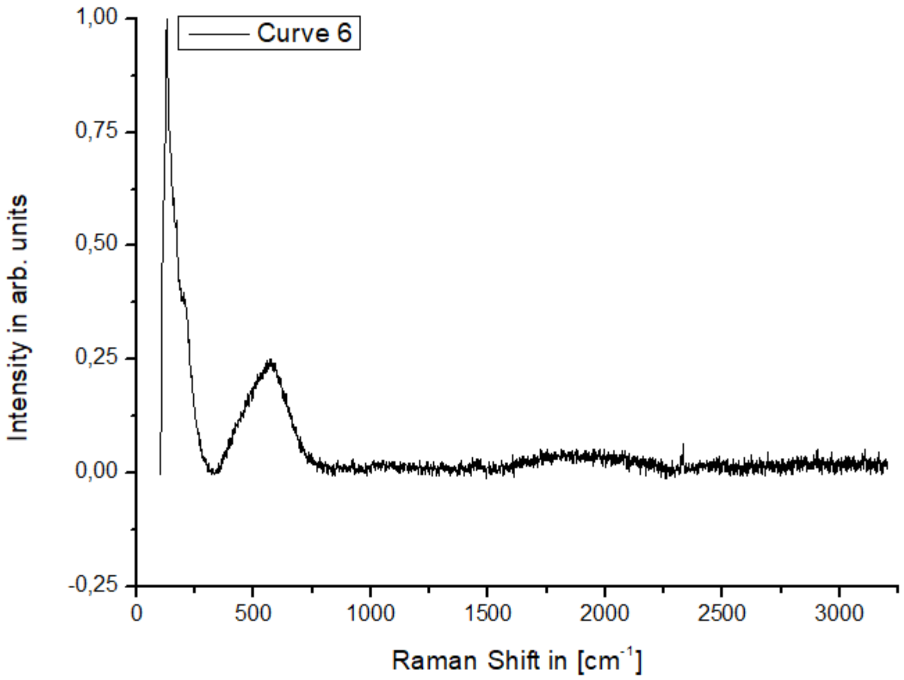

Figure 3. Raman spectrum acquired at a topography maximum of a pin textured without PAO 40. Curve 6 in figure 22.

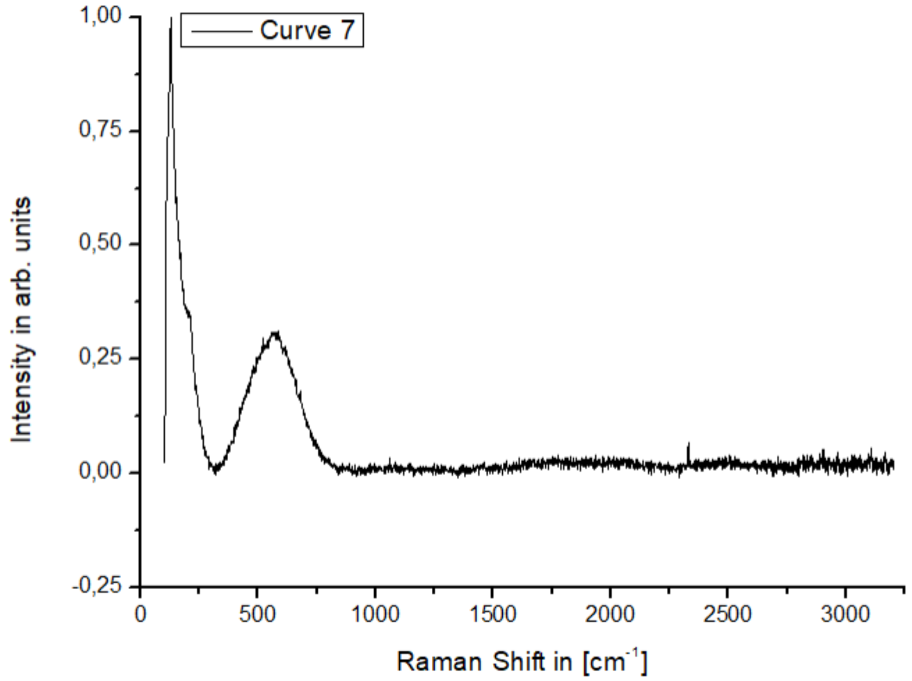

Figure 4. Raman spectrum acquired at a topography minimum of a pin textured without PAO 40. Curve 7 in figure 22.

Table 2. Assignment of functional groups to the absorption peaks obtained for a pin textured without lubricant. The table also shows the peaks intensity. The theoretical range of the absorption bands for the assignment was extracted from [111]

Raman Shift [cm^{-1}]		**Peak Assignment**	**Intensity**
Topography maximum Curve 6	Topography minimum Curve 7		
129.42	126.74	SnO_2 / SnO Cu_2O	strong
193.39	202.67		
574.94	573.68	$Sn(OH)_2$ Cu_2O	medium
2332.01	2332.01	N_2	weak

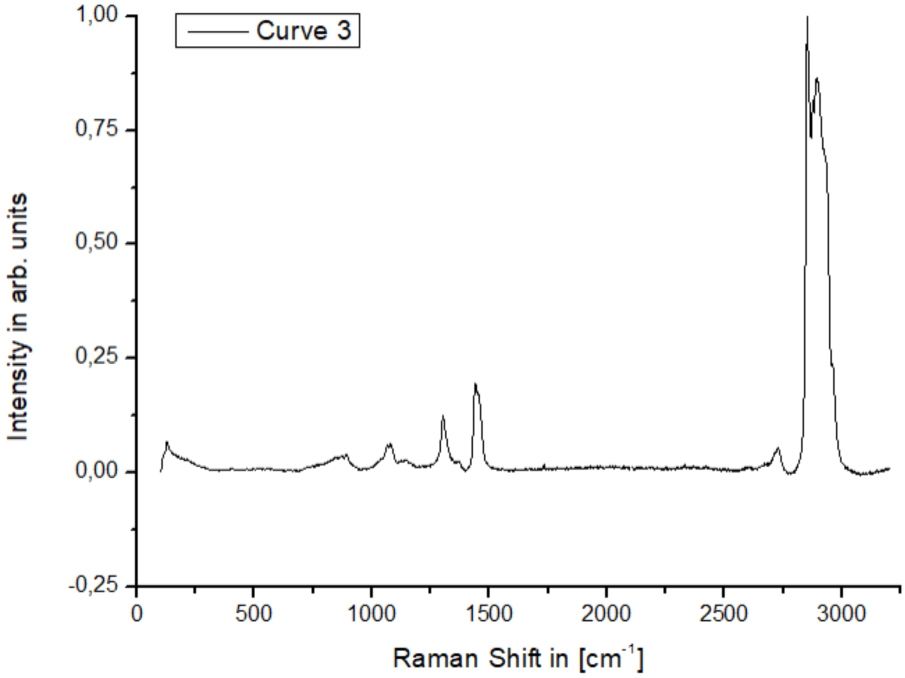

Figure 5. Raman spectrum acquired at a topography maximum of a pin textured with PAO 40. Curve 3 in figure 22.

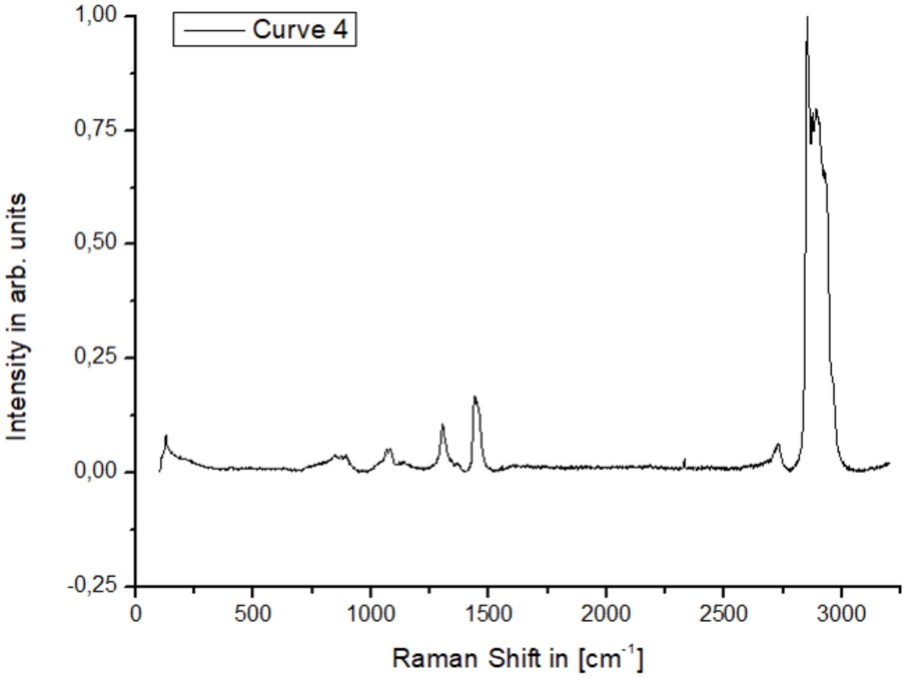

Figure 6. Raman spectrum acquired at a topography minimum of a pin textured with PAO 40. Curve 4 in figure 22.

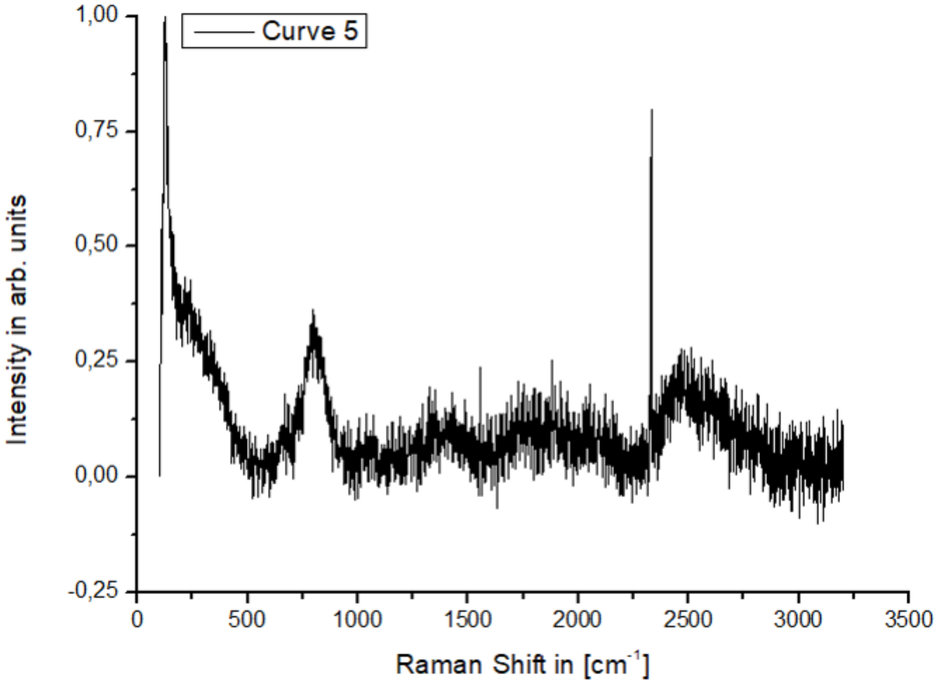

Figure 7. Raman spectrum acquired at other topography minimum of the pin textured with PAO 40 of previous figure. Curve 5 in figure 22.

Table 3. Assignment of functional groups to the absorption peaks obtained for a pin textured with lubricant. The table also shows the peaks intensity. The theoretical range of the absorption bands for the assignment was extracted from [111]

Raman Shift [cm^{-1}]			**Peak Assignment**	**Intensity**
Texture maximum Curve 3	Texture minimum Curve 4	Texture minimum Curve 5		
129.42	132.10	124.07	SnO_2 / SnO Cu_2O	Strong
-	-	227.81		
877.34	867.66	799.57	SnO $Sn(OH)_2$ $Sn(OH)_4$	Medium
1072.78	1073.95	1061.02	CuO Cu_2O PAO 40	weak
1140.60	1141.77	-	PAO 40	Weak
1303.87	1309.55	-		Weak
1371.69	1371.69	-		Weak
1445.50	1443.38	-		Medium
-	-	2332.01	N_2	Strong
2728.54	2727.63	-	PAO 40	Weak
2854.17	2852.41	-		Strong
2891.05	2896.29	-		Strong
2962.32	-	-		Medium